

# IMAGING SPECTROSCOPY OF HETEROGENEOUS TWO-DIMENSIONAL MATERIALS

A Dissertation

Presented to the Faculty of the Graduate School

of Cornell University

In Partial Fulfillment of the Requirements for the Degree of

Doctor of Philosophy

by

Robin Havener

August 2014

This work is licensed under the Creative Commons Attribution-NonCommercial-ShareAlike 4.0 International License. To view a copy of this license, visit <http://creativecommons.org/licenses/by-nc-sa/4.0/>.

2014, Robin Havener

# IMAGING SPECTROSCOPY OF HETEROGENEOUS TWO-DIMENSIONAL MATERIALS

Robin Havener, Ph. D.

Cornell University 2014

Heterogeneities in two-dimensional (2D) materials, including variations in layer number and stacking order, spatial variations in chemical composition, and point defects, may provide these systems with a variety of unique optical and electronic properties. Many of these structures form inherently when 2D materials are produced on a large scale with chemical vapor deposition (CVD), and artificial heterojunctions between different 2D materials can also be produced by design. In this work, we address the challenges of visualizing the local structure and composition of heterogeneous 2D materials, and of establishing clear relationships between these structural features and the materials' properties.

For this purpose, we first introduce two novel optical imaging spectroscopy techniques: DUV-Vis-NIR hyperspectral microscopy and widefield Raman imaging. These techniques enable comprehensive, all-optical mapping of chemical composition in lateral 2D heterojunctions, graphene visualization on arbitrary substrates, large-scale studies of defect distribution in CVD-grown samples, and real-time imaging of dynamic processes. They can also determine the optical response of an unknown 2D material, and in combination with existing high resolution imaging tools such as dark-field transmission electron microscopy, they can be used to establish quantitative structure-property relationships for a variety of 2D heterostructures.

We next apply these methods to the first comprehensive study of the optical properties of twisted bilayer graphene (tBLG), a heterostructure where two graphene layers are rotated by a relative angle ( $\theta$ ), relating the optical conductivity and Raman spectra to  $\theta$  for many tBLG samples. Our results establish the importance of interlayer coupling in tBLG at all  $\theta$ , and our data suggest that unique many-body effects play vital roles in both the optical absorption and Raman response of tBLG. These findings provide a framework for understanding the effects of the  $\theta$  degree of freedom in other stacked 2D materials, and the suite of techniques that we have developed will play a key role in the characterization of heterogeneous 2D materials for years to come.

## BIOGRAPHICAL SKETCH

Robin W. Havener was born in 1986 and grew up in a small town near Boston, Massachusetts. She graduated from The Governor's Academy (formerly Governor Dummer Academy) of Byfield, Massachusetts in 2004, and studied Materials Science and Engineering at the University of Pennsylvania in Philadelphia, Pennsylvania. After receiving her B.S.E. in 2008, she entered the Applied Physics doctoral program at Cornell University in Ithaca, New York. She completed her Ph.D. research under the supervision of Prof. Jiwoong Park, receiving a National Science Foundation Graduate Research Fellowship in 2009. Robin will join the technical staff of MIT Lincoln Laboratory in September of 2014.

To my parents

## ACKNOWLEDGMENTS

None of the work that I accomplished during my six years at Cornell would have been possible without the support (both academic and personal) that I've received from a great number of colleagues, friends, and family throughout my time here. First, I would like to thank to my parents – while they worked hard from the time I was young to ensure that I'd have the best possible education, I don't think they could have guessed that they'd see me through 23 years of school! Mom and Dad, your advice and encouragement (and fond memories of many trips to the Boston Museum of Science) have been invaluable. It goes without saying that none of my achievements so far would have been possible without you, and so I dedicate my dissertation to you with love.

Next, I'd like to thank my Aunt June, and remember my Uncle Charlie, for showing me the joy that comes alongside a lifelong passion for learning. Aunt June, a biology teacher, has an infectious enthusiasm for the outdoors, and every excursion we've taken together has been an adventure, even the ones that haven't involved wrangling cows. Uncle Charlie, an electrical engineer, was a voracious reader about all areas of science and beyond, and was always eager to talk about what he had learned from his most recent book. I'm very grateful to both of you for your wholehearted support of my decisions to pursue increasingly higher levels of education, and I'm proud to have followed in both of your footsteps (quite literally for Uncle Charlie's case, since he was here at Cornell 50 years ago).

So much of the graduate school experience hinges on picking the right research advisor, and (very much in hindsight, of course) I consider joining Jiwoong Park's group to be one of the best decisions I could have made. Jiwoong, while I often get lost in the details of a project, I appreciate that I have always been able to rely on you for your scientific insights and your

grounded perspective. Jiwoong also never lets any of his students settle for the result that we have, whether it be a piece of data or a draft of a paper (or thesis), when he knows that we can do a better job. Even though his attitude has made me want to pull my hair out more than once, I've always had to admit that my work has been better for it.

Another reason I'm glad to have joined Jiwoong's group is the unusual amount of collaboration that he fosters between his students. I'm very grateful for the support I've received from all of my labmates, and am fortunate for the opportunity to have contributed to so many exciting projects during my time in the group. Sang-Yong, I truly value the time and consideration that you put into mentoring me during my first year and a half – you went above and beyond, and gave me a great foundation for my research. Lola and Cheol-Joo, thank you for tirelessly growing the beautiful samples featured in this dissertation. Matt and Fai, thank you for making the basement of PSB a little less lonely with candy and lots of optics advice. Dan, thank you for showing me what it means to work hard, and thanks as well to Li and Mike for your help with nanotubes during the early years. Lulu, Wei, and Mark (and Cheol-Joo and Lola, again), thank you for taking the time to advise me on how to fabricate my own devices, something I put off doing for far too long. Carlos, Michal, Zenghui, and Joel, thank you for all of your additional contributions to my published research. Kan-Heng, Saien, Yimo, Yui, and Kibum, I'm so glad that we've been able to work together, and I'm already excited to see what you've accomplished during your short time here.

Next, I owe a special thanks to my theorist collaborators – Yufeng Liang and Li Yang from Washington University in St. Louis, and Houlong Zhuang and Richard Hennig from Cornell. The discussions we had were invaluable during the time that we were struggling to disentangle the optical properties of twisted bilayer graphene, and I would have been lost without

your insights. I'd also like to thank Paul McEuen for his intellectual and career-related support, and Josh Kevek for his help building the Kavli DUV microscope. In addition, I've enjoyed a number of collaborations and fun scientific discussions with several members of David Muller's group, Robby, Megan, Elliot, and Julia, and I very much appreciate the support of my special committee, Poul Petersen and Dan Ralph.

Finally, I've been incredibly fortunate that many of my classmates and labmates at Cornell have also become some of my dearest friends. Lola, Mark, Carlos, Cheol-Joo, Julia, Robby, and of course, Wei, I can't imagine anyone else with whom I'd rather celebrate and commiserate the ups and downs of graduate school. You made Ithaca my home during the time we were here together, and it was thanks to all of you that this whole experience was actually (mostly) fun. It is unfortunate that graduating means that many of us will move away from each other, but I'm excited to find out where the next stage of our lives will take us.

## TABLE OF CONTENTS

Chapter 1 : INTRODUCTION.....	1
1.1   Overview .....	1
1.2   Various 2D materials .....	4
1.3   Methods of producing 2D materials .....	7
1.4   Structure of CVD-grown 2D materials .....	9
1.5   Lateral Patterning .....	11
1.6   Transfer.....	13
1.7   Outlook.....	14
References .....	17
Chapter 2 : IMAGING TWO-DIMENSIONAL MATERIALS.....	21
2.1   Introduction .....	21
2.2   Electron microscopy .....	22
2.3   Scanning probe microscopy .....	26
2.4   Optical microscopy.....	29
2.5   Outlook.....	31
References .....	34
Chapter 3 : DUV-VIS-NIR HYPERSPECTRAL IMAGING .....	36
3.1   Introduction .....	36
3.2   Absorption spectroscopy .....	37
3.3   Details of the DUV-Vis-NIR microscope.....	40
3.4   Monochromatic and hyperspectral imaging .....	44
3.5   Quantitative absorption spectroscopy.....	46
3.6   Imaging on silicon substrates .....	50
3.7   Conclusion.....	51

References .....	52
<b>Chapter 4 : WIDEFIELD RAMAN IMAGING .....</b>	<b>54</b>
4.1   Introduction .....	54
4.2   Raman spectroscopy .....	55
4.3   Widefield and confocal microscopy .....	58
4.4   Widefield Raman microscope design .....	60
4.5   Spectrally resolved imaging .....	63
4.6   Thermal effects of laser power .....	66
4.7   Substrate-independent imaging .....	67
4.8   Defect mapping .....	70
4.9   Dynamic imaging and spectroscopy.....	73
4.10   Conclusion.....	76
References .....	77
<b>Chapter 5 : BAND STRUCTURE AND OPTICAL ABSORPTION OF TWISTED BILAYER GRAPHENE .....</b>	<b>79</b>
5.1   Introduction .....	79
5.2   Defining the physical structure of tBLG .....	80
5.3   Electronic properties.....	85
5.4   Calculated optical properties of tBLG.....	89
5.5   Experimental results .....	97
5.6   Applications.....	101
5.7   Conclusion.....	103
References .....	105
<b>Chapter 6 : MANY-BODY OPTICAL PROCESSES IN TWISTED BILAYER GRAPHENE</b>	<b>107</b>
6.1   Introduction .....	107

6.2   Tight binding description of tBLG optical absorption vs. experiment .....	109
6.3   Excitonic effects .....	111
6.4   Bound excitons in tBLG .....	118
6.5   $\theta$ -dependence of Raman scattering of tBLG .....	119
6.6   Mechanism for G band enhancement .....	126
6.7   Applications.....	130
6.8   Conclusion.....	133
References .....	134
Chapter 7 : FUTURE DIRECTIONS .....	136
7.1   Introduction .....	136
7.2   Optical properties of tBLG vs. doping and vertical field .....	137
7.3   MoS <sub>2</sub> and related transition metal dichalcogenides.....	141
7.4   Artificial vertical heterostructures .....	145
7.5   Summary .....	147
References .....	149

## LIST OF FIGURES

Figure 1.1: Typical thin films vs. 2D materials .....	2
Figure 1.2: Graphene and hexagonal boron nitride .....	5
Figure 1.3: Molybdenum disulfide .....	6
Figure 1.4: Heterogeneities in CVD graphene.....	9
Figure 1.5: Lateral stitching and patterned regrowth.....	12
Figure 1.6: CVD graphene transfer.....	13
Figure 2.1: STEM and EELS imaging of 2D materials .....	22
Figure 2.2: Dark-field TEM imaging of graphene.....	24
Figure 2.3: SEM of graphene.....	25
Figure 2.4: AFM of graphene .....	27
Figure 2.5: STM of graphene.....	28
Figure 2.6: Making graphene visible .....	29
Figure 3.1: Optical absorption in graphene.....	38
Figure 3.2: UV absorption spectra of graphene and <i>h</i> -BN .....	39
Figure 3.3: Schematic and photographs of DUV-Vis-NIR microscope .....	41
Figure 3.4: Reflective objective.....	43
Figure 3.5: Sample illumination and image normalization.....	43
Figure 3.6: Imaging and spectroscopy of graphene/ <i>h</i> -BN heterostructures .....	44
Figure 3.7: Quantitative calculation of intrinsic optical conductivity .....	47
Figure 3.8: Contrast as a function of $\text{Re}[\sigma]$ and $\text{Im}[\sigma]$ .....	48
Figure 3.9: Reflection spectroscopy on Si/SiO <sub>2</sub> .....	50
Figure 4.1: Raman spectrum of graphene .....	56

Figure 4.2: Raman processes in graphene.....	57
Figure 4.3: Confocal vs. widefield Raman imaging .....	59
Figure 4.4: Schematic of widefield Raman setup .....	61
Figure 4.5: Rapid Raman imaging of $sp^2$ -bonded carbon materials .....	62
Figure 4.6: Tunable bandpass filter .....	63
Figure 4.7: Spectrally resolved imaging .....	64
Figure 4.8: Graphene temperature vs. laser power .....	66
Figure 4.9: Substrate-independent imaging .....	67
Figure 4.10: G and 2D band widefield Raman imaging of graphene on copper .....	69
Figure 4.11: D band imaging of CVD graphene.....	70
Figure 4.12: Raman and DF-TEM grain boundary imaging.....	72
Figure 4.13: Time-resolved Raman imaging .....	73
Figure 4.14: Dynamic spectroscopy .....	75
Figure 5.1: Single layer, Bernal, and twisted bilayer graphene .....	80
Figure 5.2: Commensurate tBLG.....	82
Figure 5.3: Unit cell size vs. $\theta$ .....	83
Figure 5.4: Spatially varying structure in twisted multilayer graphene.....	84
Figure 5.5: Continuum model of tBLG band structure.....	85
Figure 5.6: Experimental studies of the tBLG DOS .....	87
Figure 5.7: Full band structure of graphene.....	88
Figure 5.8: JDOS in tBLG .....	90
Figure 5.9: Calculated JDOS with coupling .....	92
Figure 5.10: Tight binding band structure of $13.2^\circ$ tBLG .....	93

Figure 5.11: Optical matrix element .....	95
Figure 5.12: Calculated optical absorption of tBLG.....	96
Figure 5.13: Correlating optical absorption with $\theta$ .....	97
Figure 5.14: Optical conductivity of tBLG.....	98
Figure 5.15: 2D plot of tBLG optical conductivity.....	99
Figure 5.16: All-optical $\theta$ mapping.....	101
Figure 5.17: tBLG imaging on Si/SiO <sub>2</sub> .....	102
Figure 6.1: Comparison of experimental data with tight binding calculations.....	109
Figure 6.2: Saddle point exciton in single layer graphene.....	112
Figure 6.3: Excitonic effects in tBLG.....	114
Figure 6.4: Bound excitons in tBLG.....	118
Figure 6.5: Raman imaging of tBLG .....	121
Figure 6.6: G band enhancement on resonance .....	122
Figure 6.7: Excitation energy dependent G band resonance.....	122
Figure 6.8: G peak position and width dependence on $\theta$ .....	123
Figure 6.9: 2D band behavior .....	124
Figure 6.10: 2D/G ratio.....	125
Figure 6.11: Double resonance Raman enhancement.....	126
Figure 6.12: Simplified calculation of G band intensity.....	128
Figure 6.13: Asymmetry in our A <sub>G</sub> vs. $\theta$ data.....	129
Figure 6.14: Raman imaging of interlayer coupling in tBLG.....	131
Figure 6.15: AFM of artificially transferred bilayer graphene .....	132
Figure 7.1: Doping and vertical field in tBLG.....	137

Figure 7.2: Transparent, dual gated tBLG transistor .....	138
Figure 7.3: Field and doping effects on the $E_A$ peak .....	140
Figure 7.4: Doping and field dependence of $E_A$ peak parameters .....	140
Figure 7.5: Absorption spectra of bulk TMDs.....	143
Figure 7.6: Artificial vertical heterostructures.....	145
Figure 7.7: Controlling twist angle in vertical stacks .....	146

## **Chapter 1 : INTRODUCTION**

### **1.1 | Overview**

Developing precise control over the composition and properties of thin films has been crucial for many advances in modern technology. The manufacture of products such as computer chips, light emitting diodes, and semiconductor lasers relies heavily on thin film deposition and patterning techniques to transform a solid substrate into a complex, functional device. However, while the active areas of these devices can be as thin as a few atoms, they are permanently affixed to their bulk substrates. These substrates often serve little purpose beyond that of mechanical support, limiting many potential thin film device geometries.

Two-dimensional (2D) materials are an emerging class of thin films which do not require a supporting substrate, and which have created significant interest for both fundamental research and device applications. 2D materials are mechanically continuous sheets which are a few atoms or fewer in thickness. What makes these thin films unique is that they are self-contained: in-plane, they are held together with strong covalent bonds, but they lack the reactive dangling bonds which are found at most other solid surfaces. Unlike many other thin films, they are typically stable if removed from a supporting substrate. In addition, if a 2D material is placed on top of a bulk surface or another 2D material, it interacts through weak van der Waals forces which do not disrupt its in-plane bonding.

An analogy which provides an excellent summary of these properties, and indicates their exciting potential, is that 2D materials can act as discrete, atomically thin “building blocks.” The implication is that some of the most fascinating aspects of these thin films are the ways in which they can be manipulated and combined to form complex structures. One possibility, like other

thin films, is that 2D materials with different chemical compositions may be deposited layer by layer to form a device. There are currently many known 2D materials with a variety of optical and electronic properties. The most familiar example is graphene, a semimetallic, single atom thick sheet of carbon atoms, which will be the main focus of this dissertation. However, other 2D materials, such as insulating hexagonal boron nitride (*h*-BN) and semiconducting molybdenum disulfide (MoS<sub>2</sub>), have been studied intensively during the past several years, and more exotic examples continue to be discovered. As with other thin films, it is possible to synthesize many of these materials on a wafer scale, and exert a high degree of control over their properties by varying parameters such as their composition, physical structure, or dopant density.

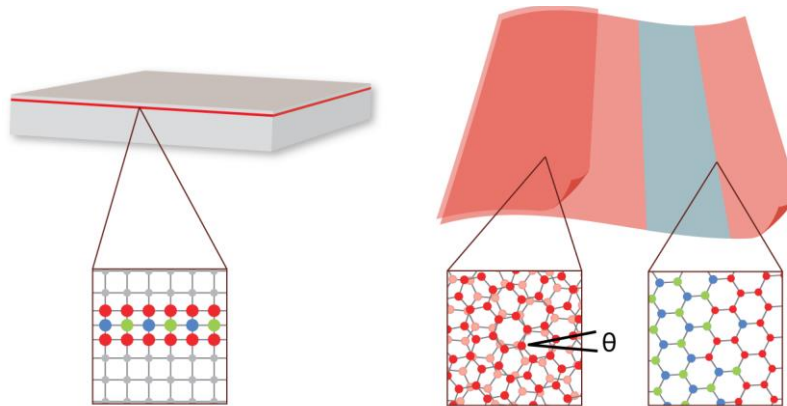


**Figure 1.1: Typical thin films vs. 2D materials**

(left) MBE can be used to produce highly crystalline thin films and exert precise control over the composition of each atomic layer, but these films are covalently bonded to their bulk substrate. (right) 2D materials exist independently of a supporting substrate. Since the bonding between layers is weaker, their interlayer rotation ( $\theta$ ) is a new degree of freedom. It is also possible to pattern lateral heterostructures between 2D materials with different compositions.

However, there are also a number of novel 2D device geometries which cannot be produced with other thin films. First, because 2D materials are self-contained, they can be manipulated, processed, and patterned easily, often with few alterations to their intrinsic

properties. They can also be transferred to arbitrary substrates for a variety of applications, and can conform to irregular or flexible surfaces due to their extreme thinness.

In addition, many of the structural features which are formed when various 2D materials are combined are unique to this class of thin films (Figure 1.1). For example, unlike epitaxial films (such as those produced with molecular beam epitaxy) which require registry between the crystal lattices of each adjacent layer, stacked 2D materials can form atomically precise vertical junctions regardless of their intrinsic lattice parameters. Moreover, the stacking of weakly coupled, crystalline 2D layers adds a unique degree of freedom, the relative rotation angle ( $\theta$ ) between the orientations of each layer. A number of novel,  $\theta$ -dependent optical and electronic signatures have recently been observed in multilayers of 2D materials such as graphene and MoS<sub>2</sub>, providing additional tunability to the properties of these systems. 2D materials with different compositions or dopant densities can also be stitched together to make mechanically continuous, atomically thin lateral heterostructures, aided by the ability to pattern and process them.

While the intrinsic properties of 2D materials such as graphene, MoS<sub>2</sub>, and *h*-BN have been thoroughly characterized over the past decade, many of the properties of the novel, heterogeneous 2D systems described above have remained poorly understood. This dissertation addresses two challenges in this area. First, new tools are required for the basic *characterization* of these systems. Because the composition and structure of 2D materials can vary spatially, *imaging*, rather than point or bulk measurements, is crucial for their characterization. However, in addition to being sensitive to variations in these materials' composition and structure, ideal imaging techniques should also operate independently of the substrate to which the 2D material is transferred. Moreover, a single tool should be able to identify and characterize many different

2D materials in a single heterostructure device simultaneously. In Chapters 3 and 4, we introduce two novel optical tools for *imaging spectroscopy* which are optimized for rapid, large scale characterization of 2D materials on a variety of substrates.

Second, we begin to explore the ways in which these complex features can affect the properties of the resulting 2D materials. Taking advantage of the unique capabilities of the tools developed in the preceding chapters, we focus on quantitatively characterizing the effects of interlayer rotation ( $\theta$ ) on the optical properties of a prototypical stacked 2D material, *twisted bilayer graphene (tBLG)*. Our work represents the first comprehensive study of the  $\theta$ -dependent structure-property relationships in any stacked 2D system. In Chapters 5 and 6, we consider the relationship between  $\theta$  and the band structure and optical transitions in tBLG, as well as the many-body optical processes in this material, including excitonic effects and Raman scattering.

In this chapter, we will review the current state of 2D materials synthesis, heterojunction fabrication, and transfer to arbitrary substrates, focusing on graphene and other 2D materials produced on a large scale with chemical vapor deposition (CVD). As we will discuss, CVD-grown 2D materials are excellent model systems for studying twisted multilayers, and serve as starting points for lateral patterning and transfer.

## 1.2 | Various 2D materials

The family of two-dimensional materials continues to grow, and several examples are presented in Figure 1.2 and Figure 1.3. Graphene, the best known 2D material and the subject of the 2010 Nobel Prize in Physics [1], is a semimetallic, single-atom thick sheet of carbon atoms arranged in a honeycomb lattice. Hexagonal boron nitride (*h*-BN) is an analog to graphene whose carbon atoms are replaced by alternating boron and nitrogen atoms. It is an insulator with a large optical

band gap of  $\sim 6$  eV [2,3]. Also of note, although not the main focus of this work, are monolayer transition metal dichalcogenides (TMDs). TMDs are three atoms thick, and have the chemical composition  $\text{MX}_2$ , where M is a metal atom (examples include Mo, W, Cr, Co, Ni, and Ta) and X is a chalcogen from group 16 of the periodic table (S, Se, Te) [4,5]. These materials can exhibit a variety of electronic properties [6], but many of the most studied examples (e.g.  $\text{MoS}_2$ ,  $\text{MoSe}_2$ ,  $\text{WS}_2$ ) are semiconductors.

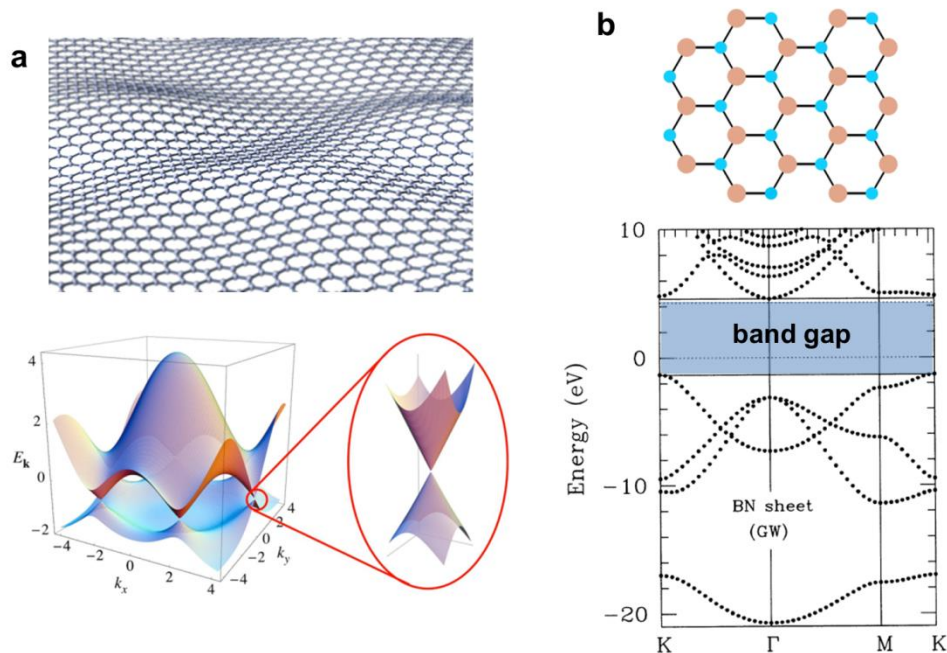


**Figure 1.2: Graphene and hexagonal boron nitride**

(a, top) An artist's rendition of a freestanding sheet of single layer graphene. Carbon atoms are bonded in a hexagonal lattice which is one atom thick. [7] (bottom) The tight binding calculated band structure of graphene, highlighting the linear, gapless bands at low energies. Here, energy is plotted in units of a tight binding parameter  $t = 2.7$  eV. [8] (b, top) The structure of hexagonal boron nitride ( $h$ -BN) which is similar to that of graphene, except that it contains alternating atoms of boron (blue) and nitrogen (orange). [9] (bottom) The *ab initio* calculated band structure of monolayer  $h$ -BN, illustrating the large band gap. [10]

Early studies of 2D materials focused on the fundamental physics of pristine single- and few-layer samples. While some of these findings will be discussed in more detail in subsequent

chapters, we summarize several main results here. First, monolayer graphene has a unique linear band structure near its charge neutrality point, and has served as a platform for many studies of two-dimensional physics, including the integer [11,12] and fractional [13,14] quantum Hall effects. Pristine graphene exhibits very high carrier mobility [15], as well as high mechanical strength [16] and uniform broadband optical absorption [17]. Bernal stacked (i.e. oriented) bilayer graphene is also metallic, but a band gap can be opened in this material under the application of a vertical electric field [18].

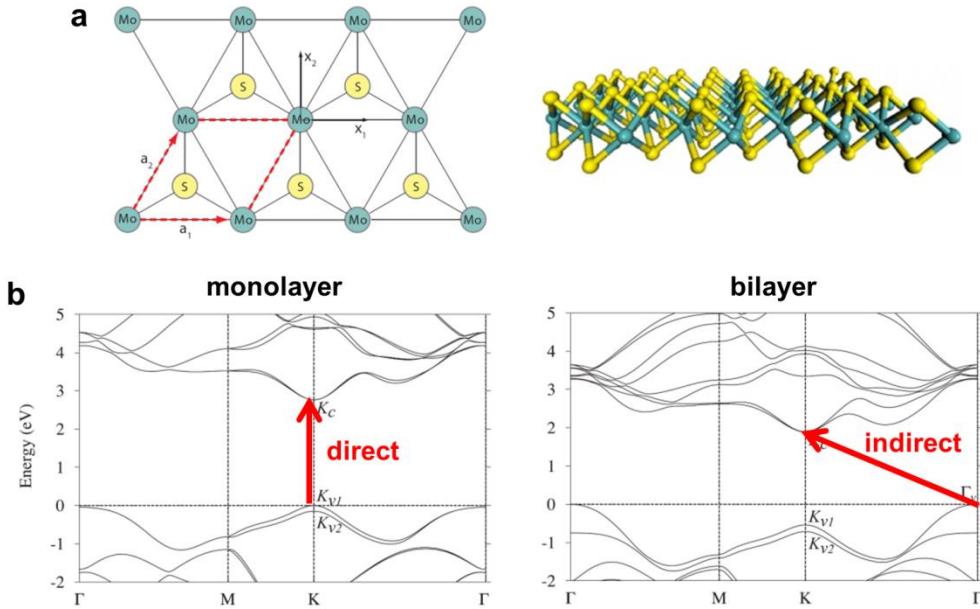


**Figure 1.3: Molybdenum disulfide**

(a) A top-down (left) and side (right) view of MoS<sub>2</sub>, a TMD. MoS<sub>2</sub> is three atoms thick, but has a similar symmetry as *h*-BN when viewed from the top. [19,20] (b) The *ab initio* calculated band structures of monolayer and bilayer MoS<sub>2</sub>, showing the transition from a direct to an indirect band gap. [21]

Next, for MoS<sub>2</sub> and several other semiconducting TMDs, it was found that monolayers have a direct band gap, while oriented multilayers have an indirect band gap [22]. The additional valley degree of freedom in MoS<sub>2</sub>, coupled with the direct band gap of MoS<sub>2</sub> monolayers, has led

to a variety of interesting optical physics in this material and other related TMDs (such as MoSe<sub>2</sub> and WS<sub>2</sub>) [23,24]. Lastly, insulating *h*-BN has been shown to be a high quality dielectric for graphene [3] and other 2D electronic devices, reducing spatial fluctuations in the charge density of the active material due to its lack of dangling bonds.

In order to perform these fundamental studies, it was essential to develop methods of isolating 2D materials. The initial studies of the intrinsic properties of the 2D materials discussed in this section were performed on high quality samples, which were produced on a small scale using a mechanical exfoliation technique. Later, methods were developed to synthesize 2D materials on a larger scale, toward the goal of harnessing some of their unique properties for real world applications. Each of these methods of producing 2D materials will be discussed in more detail in the following section.

### **1.3 | Methods of producing 2D materials**

The first atomically thin 2D crystals, including graphene and MoS<sub>2</sub>, were isolated in 2004. These initial studies used mechanical exfoliation from high quality bulk crystals, or the “Scotch tape method” [25,26], to isolate single- and few-layer 2D samples. After mechanical exfoliation is performed, the target substrate is covered in pieces of the material which vary randomly in size and number of layers. The user must search the entire substrate by eye with an optical microscope to locate the thinnest pieces, which are typically several microns in extent. While exfoliation continues to produce the highest quality 2D crystals, this technique cannot create large area samples.

However, for any viable technological application, it is necessary to produce 2D materials on a large scale. For the case of graphene, it has been known for several decades that

thin graphitic layers can form easily on many metal surfaces, but they were once considered impurities [27]. After graphene was isolated by mechanical exfoliation, it was found that more controlled, few-layer islands of graphene can grow epitaxially under ultrahigh vacuum on certain metal substrates [28-30]. Graphene can also grow epitaxially on silicon carbide, providing large area samples with various numbers of layers [31,32]. With all of these growth methods, however, the graphene is difficult to remove from its substrate. In many cases, there is also strong electronic coupling between the graphene and the substrate, which can alter the intrinsic properties of the graphene.

Chemical vapor deposition (CVD), adopted in 2009 for graphene, is a technique for synthesizing a variety of single- and few-layer 2D materials of arbitrary size. The CVD process involves heating a substrate in a furnace and flowing in gaseous precursors, which decompose and deposit solid material onto the substrate. For the proper choice of substrate and growth conditions, this process can be self-limiting, and a monolayer of the target material can grow. Copper was found to be an ideal growth substrate for both graphene [33,34] and *h*-BN [35-37], and can produce monolayer films of both materials. Importantly, the 2D material is easily removed from the substrate after growth (see Section 1.6). The CVD growth of TMDs is not as well established as that of graphene or *h*-BN, but current methods enable the production of high quality MoS<sub>2</sub> monolayers on small areas of the growth substrate [38,39].

CVD-grown 2D materials, specifically graphene and *h*-BN, are the main subjects of this dissertation. Not only does this growth method produce scalable, high quality samples, but CVD-grown 2D materials are model systems for studying many of the complex 2D structures discussed in Section 1.1. Multilayer regions with varying  $\theta$  often grow during CVD synthesis. In addition, CVD is easily adapted to introduce compositional variations into the growing material,

and is necessary to produce laterally patterned samples (Section 1.5). In Section 1.4, we discuss several common structural features in CVD-grown 2D materials which will be of interest in the following chapters.

#### 1.4 | Structure of CVD-grown 2D materials

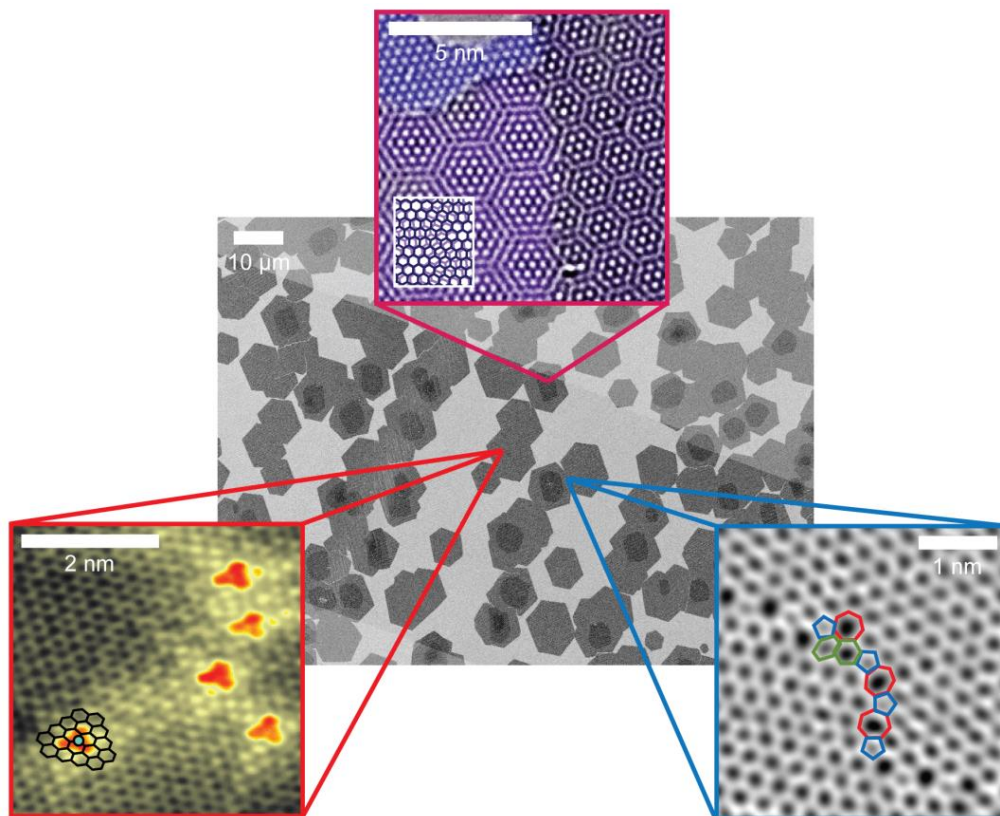


**Figure 1.4: Heterogeneities in CVD graphene**

The center scanning electron microscope (SEM) image illustrates the typical island growth of CVD graphene on copper [40], ultimately leading to grain boundaries (STEM image, right) [41] and twisted multilayers (TEM image, top) [42] in the final material. Point defects (STM image, left) [43] can also be incorporated into the growth, either unintentionally or by design.

Most CVD growth processes produce inherently heterogeneous 2D films, shown in Figure 1.4.

First, CVD-grown samples can contain localized defects, such as vacancies or substitutional impurities. When the conditions are not ideal, defects can be introduced unintentionally during

growth, and monitoring the presence of defects is an important way to evaluate a particular growth recipe. Point defects can also be introduced by design to control the density of free carriers in the resulting material. For example, interstitial boron and nitrogen atoms can either *p*- or *n*-dope the graphene, and can be introduced into the lattice by adding small amounts of boron- or nitrogen-containing precursors during growth [43-45]. The left panel of Figure 1.4 shows an atomic resolution image of individual interstitial nitrogen dopants (located within the red triangles; see schematic) incorporated into a CVD graphene lattice.

Next, CVD graphene and *h*-BN on copper typically grow in islands from central nucleation sites (Figure 1.4, center). The crystalline orientation is not necessarily correlated from island to island, and if the growth is allowed to progress until the substrate is fully covered, then grain boundaries usually form where the islands meet. The right panel of Figure 1.4 shows an atomic scale image of a grain boundary in CVD graphene; although the mechanical continuity of the film is maintained, the local bonding of the carbon atoms is altered along the boundary. Grain boundaries can also exist within a single island, often emanating from the central nucleation site [41,46]. In addition, other line defects such as wrinkles [47] and cracks in the growing material may form during the CVD process.

Finally, depending on the growth conditions, multilayer regions may also grow at the center of each island. The additional layers that grow during CVD may be either oriented or rotated with respect to the first layer, and a single multilayer region may contain multiple domains with numerous relative rotation angles [48]. The top panel of Figure 1.4 shows an atomic scale image of two tBLG domains in a CVD-grown sample. The rotational mismatch of the two single graphene layers causes a moiré pattern to emerge in the twisted regions (see inset), and the period of this moiré pattern decreases with increasing  $\theta$ . Overall, CVD-grown samples

have enabled the first systematic studies of point defects, grain boundaries, and twisted multilayers in 2D materials, since exfoliated samples typically originate from pure, highly crystalline bulk materials in which every layer is oriented.

While these features are interesting subjects of study, we note that it can also be desirable to reduce heterogeneities in CVD-grown samples in order to carefully control the properties of the final product. To increase grain size, the nucleation density of graphene can be reduced to as little as  $\sim 1/\text{cm}^2$  [49] by tuning the flow rates of the precursor and carrier gases, as well as the degree of initial oxidation of the copper surface. Additionally, a crystalline surface, such as (111) copper [50-52] or (100) germanium [53], can enable preferential alignment of individual graphene or *h*-BN islands during growth, producing a crystalline sample despite a higher nucleation density. Both of these methods have the potential to produce homogeneous 2D materials on a wafer scale.

### **1.5 | Lateral Patterning**

As discussed previously, the composition and dopant density of CVD-grown 2D materials depends on the precursor gases used during growth. By extension, it is also possible to laterally control the composition of a single 2D layer during growth. Lateral variations can be produced by stopping the growth of the first material before it fully covers the substrate, and then introducing the precursors for the second material. Different 2D materials can be “stitched” together to form a mechanically continuous sheet if they have similar structures and lattice constants, such as intrinsic and doped graphene, graphene and *h*-BN, or various TMDs. The graphene/*h*-BN case has been studied particularly closely, and it has been shown that these

materials can stitch with atomic precision under certain growth conditions (Figure 1.5a) [54,56,57].

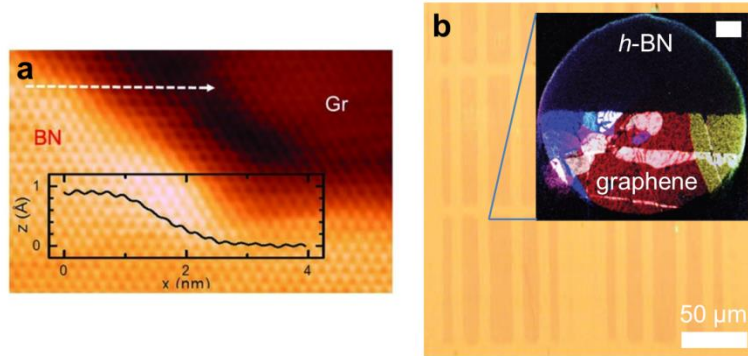


**Figure 1.5: Lateral stitching and patterned regrowth**

(a) An atomic resolution STM image of laterally stitched graphene (Gr) and *h*-BN (BN), illustrating a continuous, defect-free boundary under ultra-high vacuum growth conditions [54]. (b) An optical image of graphene (dark) and *h*-BN (light) regions produced with the patterned regrowth method. (inset) A dark-field TEM image of a mechanically continuous, suspended graphene/*h*-BN junction in a similar patterned sample. Scale bar 250 nm [55].

Introducing a sequence of different precursors into the furnace during CVD growth produces a random network of heterojunctions, but the ability to controllably pattern the composition of a layer is crucial for many applications. This is possible through a recently developed process termed “patterned regrowth” [55]. After a continuous sheet of one material is grown with CVD, it is removed from the growth furnace, and selected regions are etched away using standard photolithography techniques. Then, the sample is reintroduced into the furnace, and a second material is grown in the patterned region only [55,58]. This technique was shown to produce mechanically continuous patterned sheets of graphene/*h*-BN with junctions of width <10 nm (Figure 1.5b). Patterned regrowth can also be used to control the dopant density in graphene films, potentially enabling the fabrication of *p-n* junctions embedded within a single 2D film.

## 1.6 | Transfer

After growth and any applicable patterning, CVD-grown 2D materials must often be removed from their growth substrates. For this, a polymer layer, such as poly(methyl methacrylate) (PMMA), can be spin-coated on top of the 2D material/growth substrate. Then, the growth substrate can be etched away with a wet etchant, leaving the 2D material/polymer film floating on top of the etchant (Figure 1.6). The polymer film supports the 2D material, and the entire structure is fairly robust, allowing the graphene to undergo a series of cleaning steps to remove organic and inorganic residues [59]. Finally, the polymer/2D material membrane can be “scooped” onto a target substrate. The polymer film is removed with an organic solvent or annealing, while the 2D material remains behind [41,60,61].

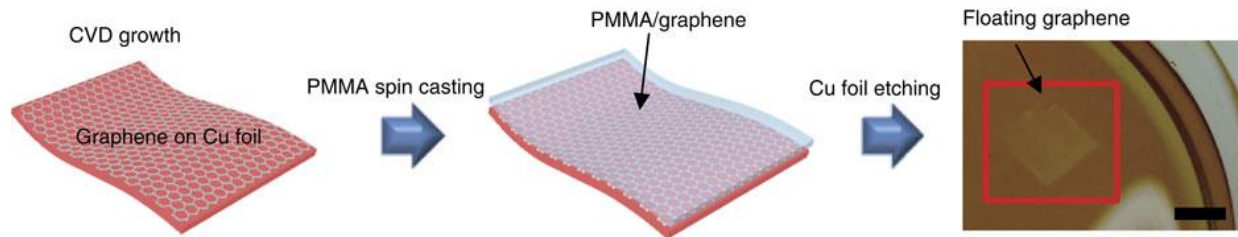


**Figure 1.6: CVD graphene transfer**

A schematic illustrating the most commonly used procedure for transferring CVD-grown 2D materials to other substrates. After etching the growth substrate, the floating PMMA/graphene membrane can be scooped out of solution onto an arbitrary target substrate [62].

Because 2D materials are self-contained, they can be transferred to arbitrary substrates for various applications, including silicon wafers for facile electronic device fabrication, fused silica for optical transparency, or polymer sheets for mechanical flexibility. Although device quality can depend on the substrate used, many of the intrinsic properties of the 2D material (e.g. its band structure, optical absorption spectrum, and Raman scattering) are maintained after

transfer [61]. The basic transfer technique has been adapted to transfer exfoliated samples onto various substrates [3], as well as for meter-scale roll-to-roll transfer of large area graphene [63].

Regardless of the target substrate, transfer cleanliness remains a significant issue, and can reduce device performance significantly. Residues from the polymer layer or etchant may remain after transfer, and contaminants may get trapped between the 2D material and the substrate. For the transfer of CVD-grown materials, efforts have been made to replace the PMMA layer with a cleaner support, such as a different polymer [64], PDMS stamp [65] or thermal release tape [63,66], as well as to dry the film before transfer [67] to reduce contaminants.

Finally, we note that sequential transfers of various 2D materials can be used to create vertical 2D heterostructures where both the composition and relative angle of each layer may be controlled. Despite the cleanliness issues discussed above, it is possible to obtain atomically precise contact between each layer. More details on the production and applications of these 2D stacks will be discussed in Chapter 7.

## **1.7 | Outlook**

As discussed in this chapter, a variety of unique structural features and compositional variations can exist in 2D materials, particularly those produced by CVD. Some of these features, such as twisted multilayers in CVD graphene, can be produced at random during growth; others, like patterned lateral heterojunctions, are created by design. In either case, it is crucial that we understand the structure and local composition of the 2D material that results after growth and patterning, and establish clear relationships between these structural features and the material's properties. This feedback will aid in the discovery of new functionalities in heterogeneous 2D

materials, taking full advantage of the novel ways in which 2D materials can be manipulated and combined.

Toward this goal, we first need to be able to visualize the structural and compositional heterogeneities in CVD-grown 2D materials. In this chapter (Figures 1.4 and 1.5), we included several images of various types of defects and heterostructures which can be found in 2D materials. In **Chapter 2**, we will review the microscopy techniques used to obtain these images, including variants of electron, scanning probe, and optical microscopy. However, these existing techniques have many shortcomings when it comes to characterizing 2D materials produced with CVD, particularly for imaging large samples with high throughput and for characterizing samples after transfer to arbitrary substrates. In Chapters 3 and 4, we introduce two optical microscopy techniques which bridge this characterization gap. **Chapter 3** describes a DUV-Vis-NIR hyperspectral microscope which can be used to image compositional variations in graphene/*h*-BN lateral heterostructures on a large scale, for samples which sit on several different substrates relevant for device fabrication. **Chapter 4** describes a widefield Raman microscope which enables rapid graphene imaging and characterization on arbitrary substrates.

For the most part, the imaging modalities in Chapters 3 and 4 take advantage of the known optical responses of various 2D materials, such as the absorption spectra of isolated graphene and *h*-BN, or the effect of point defects on the Raman spectrum of graphene. However, we also outline how each technique can be used to obtain the quantitative optical response of an *unknown* 2D material. Combined with the other direct imaging techniques outlined in Chapter 2, we have assembled a powerful suite of tools which can be used to establish new relationships between the physical structure and optical properties of 2D materials.

To culminate our new capabilities, we focus in Chapters 5 and 6 on measuring the quantitative structure-property relationships between the optical response of twisted bilayer graphene (tBLG) and its relative rotation angle ( $\theta$ ). As outlined previously, the relative rotation of stacked atomically thin layers is a degree of freedom which is truly unique to 2D materials. However, due to the previous difficulties in characterizing both the structure and the properties of a twisted 2D material simultaneously, the effects of  $\theta$  on even a very simple system like tBLG were poorly understood. In **Chapter 5**, we discuss the relationship between the physical structure of tBLG, its band structure, and its optical absorption spectrum, while in **Chapter 6** we explore the more complex effects of many-body interactions in tBLG, including excitons and Raman scattering. This work explores a wealth of new physics which is unique to tBLG, and establishes  $\theta$  as a crucial parameter to tune the properties of stacked 2D materials.

Finally, we note that while the remainder of this work will focus on the characterization of a few model examples (large scale graphene transferred to arbitrary substrates, graphene/*h*-BN lateral heterostructures, and CVD twisted bilayer graphene), the techniques we outline here are currently being adapted to study a variety of 2D systems. Examples include the optical properties of heterogeneous TMDs or the degree of interlayer coupling in artificially stacked vertical heterostructures. Similarly, the theoretical framework we develop for the band structure and optical properties of tBLG may be applied in the future for other twisted 2D materials. By developing basic tools and ideas which can be applied to many possible 2D systems, we ensure that our work will continue to be relevant in this rapidly developing field. We will touch upon these and other future directions of our work in **Chapter 7**.

## References

- [1] K. Novoselov, *Reviews of Modern Physics* **83**, 837 (2011).
- [2] K. Watanabe, T. Taniguchi, and H. Kanda, *Nature Materials* **3**, 404 (2004).
- [3] C. Dean *et al.*, *Nature Nanotechnology* **5**, 722 (2010).
- [4] A. Ayari, E. Cobas, O. Ogundadegbe, and M. Fuhrer, *Journal of Applied Physics* **101**, 014507 (2007).
- [5] J. Wilson and A. Yoffe, *Advances in Physics* **18**, 193 (1969).
- [6] C. Ataca, H. Sahin, and S. Ciraci, *Journal of Physical Chemistry C* **116**, 8983 (2012).
- [7] J. Hedberg. “graphene sheet (lens blur).” Illustration. 2013. Image of graphene sheet (lens blur) by James Hedberg. *James Hedberg*. Web. 25 Jun 2014.
- [8] A. Castro Neto, F. Guinea, N. Peres, K. Novoselov, and A. Geim, *Reviews of Modern Physics* **81**, 109 (2009).
- [9] “Crystal Layers of hexagonal Boron Nitride.” Illustration. 2006. File: Boron-Nitride h.png. *Wikimedia Commons*. Web. 25 Jun 2014.
- [10] X. Blase, A. Rubio, S. Louie, and M. Cohen, *Physical Review B* **51**, 6868 (1995).
- [11] Y. Zhang, Y. Tan, H. Stormer, and P. Kim, *Nature* **438**, 201 (2005).
- [12] K. Novoselov, A. Geim, S. Morozov, D. Jiang, M. Katsnelson, I. Grigorieva, S. Dubonos, and A. Firsov, *Nature* **438**, 197 (2005).
- [13] X. Du, I. Skachko, F. Duerr, A. Luican, and E. Andrei, *Nature* **462**, 192 (2009).
- [14] K. Bolotin, F. Ghahari, M. Shulman, H. Stormer, and P. Kim, *Nature* **462**, 196 (2009).
- [15] K. Bolotin, K. Sikes, Z. Jiang, M. Klima, G. Fudenberg, J. Hone, P. Kim, and H. Stormer, *Solid State Communications* **146**, 351 (2008).
- [16] C. Lee, X. Wei, J. Kysar, and J. Hone, *Science* **321**, 385 (2008).
- [17] R. Nair, P. Blake, A. Grigorenko, K. Novoselov, T. Booth, T. Stauber, N. Peres, and A. Geim, *Science* **320**, 1308 (2008).
- [18] Y. Zhang, T. Tang, C. Girit, Z. Hao, M. Martin, A. Zettl, M. Crommie, Y. Shen, and F. Wang, *Nature* **459**, 820 (2009).
- [19] R. Cooper, C. Lee, C. Marianetti, X. Wei, J. Hone, and J. Kysar, *Physical Review B* **87**, 035423 (2013).
- [20] H. Wang. Structure of molybdenum disulfide. Illustration. 2012. One-molecule-thick material has big advantages. *MTL News*. Web. 25 Jun 2014.

- [21] T. Cheiwchanchamnangij and W. R. L. Lambrecht, *Physical Review B* **85**, 205302 (2012).
- [22] K. Mak, C. Lee, J. Hone, J. Shan, and T. Heinz, *Physical Review Letters* **105**, 136805 (2010).
- [23] K. Mak, K. He, J. Shan, and T. Heinz, *Nature Nanotechnology* **7**, 494 (2012).
- [24] H. Zeng, J. Dai, W. Yao, D. Xiao, and X. Cui, *Nature Nanotechnology* **7**, 490 (2012).
- [25] K. Novoselov, A. Geim, S. Morozov, D. Jiang, Y. Zhang, S. Dubonos, I. Grigorieva, and A. Firsov, *Science* **306**, 666 (2004).
- [26] K. Novoselov, D. Jiang, F. Schedin, T. Booth, V. Khotkevich, S. Morozov, and A. Geim, *PNAS* **102**, 10451 (2005).
- [27] J. M. Blakely, J. S. Kim, and H. C. Potter, *Journal of Applied Physics* **41**, 2693 (1970).
- [28] P. Sutter, J. Flege, and E. Sutter, *Nature Materials* **7**, 406 (2008).
- [29] A. N'Diaye, J. Coraux, T. Plasa, C. Busse, and T. Michely, *New Journal of Physics* **10**, 043033 (2008).
- [30] P. Sutter, J. Sadowski, and E. Sutter, *Physical Review B* **80**, 245411 (2009).
- [31] C. Berger *et al.*, *Journal of Physical Chemistry B* **108**, 19912 (2004).
- [32] W. de Heer, C. Berger, M. Ruan, M. Sprinkle, X. Li, Y. Hu, B. Zhang, J. Hankinson, and E. Conrad, *PNAS* **108**, 16900 (2011).
- [33] X. Li *et al.*, *Science* **324**, 1312 (2009).
- [34] X. Li, C. Magnuson, A. Venugopal, R. Tromp, J. Hannon, E. Vogel, L. Colombo, and R. Ruoff, *Journal of the American Chemical Society* **133**, 2816 (2011).
- [35] K. Kim *et al.*, *Nano Letters* **12**, 161 (2012).
- [36] Y. Shi *et al.*, *Nano Letters* **10**, 4134 (2010).
- [37] L. Song *et al.*, *Nano Letters* **10**, 3209 (2010).
- [38] A. van der Zande *et al.*, *Nature Materials* **12**, 554 (2013).
- [39] S. Najmaei *et al.*, *Nature Materials* **12**, 754 (2013).
- [40] I. Vlassiouk, M. Regmi, P. Fulvio, S. Dai, P. Datskos, G. Eres, and S. Smirnov, *ACS Nano* **5**, 6069 (2011).
- [41] P. Huang *et al.*, *Nature* **469**, 389 (2011).
- [42] U. Ulm, Kaiser Group, and Smet Group. Grain boundary in bilayer graphene. Micrograph. n.d. TEM image of a grain boundary of bilayer graphene. Substrate (grey),

monolayer (blue), and bilayer graphene with different rotation angles forming distinctive Moire patterns (purple). Scale bar: 5nm. *Solid State Nanophysics: Max Planck Institute for Solid State Research*. Web. 25 Jun 2014.

- [43] L. Zhao *et al.*, *Science* **333**, 999 (2011).
- [44] L. Zhao *et al.*, *Nano Letters* **13**, 4659 (2013).
- [45] D. Wei, Y. Liu, Y. Wang, H. Zhang, L. Huang, and G. Yu, *Nano Letters* **9**, 1752 (2009).
- [46] J. Wofford, S. Nie, K. McCarty, N. Bartelt, and O. Dubon, *Nano Letters* **10**, 4890 (2010).
- [47] C. Ruiz-Vargas, H. Zhuang, P. Huang, A. van der Zande, S. Garg, P. McEuen, D. Muller, R. Hennig, and J. Park, *Nano Letters* **11**, 2259 (2011).
- [48] L. Brown, R. Hovden, P. Huang, M. Wojcik, D. A. Muller, and J. Park, *Nano Letters* **12**, 1609 (2012).
- [49] Z. Yan *et al.*, *ACS Nano* **6**, 9110 (2012).
- [50] L. Gao, J. Guest, and N. Guisinger, *Nano Letters* **10**, 3512 (2010).
- [51] D. Miller, M. Keller, J. Shaw, K. Rice, R. Keller, and K. Diederichsen, *AIP Advances* **3**, 082105 (2013).
- [52] L. Brown *et al.*, submitted (2014).
- [53] J. Lee *et al.*, *Science* **344**, 286 (2014).
- [54] L. Liu *et al.*, *Science* **343**, 163 (2014).
- [55] M. Levendorf, C. Kim, L. Brown, P. Huang, R. Havener, D. Muller, and J. Park, *Nature* **488**, 627 (2012).
- [56] P. Sutter, R. Cortes, J. Lahiri, and E. Sutter, *Nano Letters* **12**, 4869 (2012).
- [57] G. Han *et al.*, *ACS Nano* **7**, 10129 (2013).
- [58] Z. Liu *et al.*, *Nature Nanotechnology* **8**, 119 (2013).
- [59] X. Liang *et al.*, *ACS Nano* **5**, 9144 (2011).
- [60] A. Reina, H. Son, L. Jiao, B. Fan, M. Dresselhaus, Z. Liu, and J. Kong, *Journal of Physical Chemistry C* **112**, 17741 (2008).
- [61] Y. Wang, Z. Ni, T. Yu, Z. Shen, H. Wang, Y. Wu, W. Chen, and A. Wee, *Journal of Physical Chemistry C* **112**, 10637 (2008).
- [62] Y. Kim *et al.*, *Nature Communications* **4**, 2114 (2013).
- [63] S. Bae *et al.*, *Nature Nanotechnology* **5**, 574 (2010).

- [64] J. Song, F. Kam, R. Png, W. Seah, J. Zhuo, G. Lim, P. Ho, and L. Chua, *Nature Nanotechnology* **8**, 356 (2013).
- [65] K. Kim, Y. Zhao, H. Jang, S. Lee, J. Kim, J. Ahn, P. Kim, J. Choi, and B. Hong, *Nature* **457**, 706 (2009).
- [66] J. Caldwell *et al.*, *ACS Nano* **4**, 1108 (2010).
- [67] N. Petrone, C. Dean, I. Meric, A. van der Zande, P. Huang, L. Wang, D. Muller, K. Shepard, and J. Hone, *Nano Letters* **12**, 2751 (2012).

## Chapter 2 : IMAGING TWO-DIMENSIONAL MATERIALS

### 2.1 | Introduction

In order to study the structural features of the complex, heterogeneous 2D materials which were discussed in Chapter 1, including twisted multilayers, compositional variations, defects, and lateral heterojunctions, it is first necessary to be able to visualize these structures. In this chapter, we review a number of standard techniques which have been adapted for 2D materials characterization, including variants of electron microscopy, scanning probe microscopy, and optical microscopy. Although a myriad of characterization techniques exist which can provide information about the structural, electrical, mechanical, or optical properties of a 2D sample, we will limit our discussion to *imaging* techniques which can provide spatially resolved information about structural features in a sample. While most of the examples presented in this chapter illustrate graphene imaging, these techniques can also be applied to *h*-BN, MoS<sub>2</sub>, and other 2D materials except where otherwise noted.

An ideal imaging technique for 2D materials research would have high enough spatial resolution to directly visualize the features of interest, which can range from the atomic scale for point defects to several microns for the grain size of CVD-grown samples. However, because these samples can be hundreds of microns or larger in size, an ideal technique should not be limited to a small area of the sample, and should be able to acquire large images rapidly. In addition, because 2D materials can be transferred to a variety of substrates, a substrate-independent imaging technique is desirable so that 2D materials can be characterized directly on their target substrate. Finally, imaging techniques for 2D materials research should be non-destructive, particularly if further electronic or optoelectronic device fabrication is desired after

characterization. No one technique can currently fulfill all of these objectives. Instead, we will review the capabilities of each of the techniques described in this chapter, and discuss their advantages and disadvantages for characterizing the large area, heterogeneous 2D materials introduced in Chapter 1. In doing so, we will motivate the need for the new 2D materials characterization techniques which will be introduced in Chapters 3 and 4. Certain sections of this chapter are adapted from [1].

## 2.2 | Electron microscopy

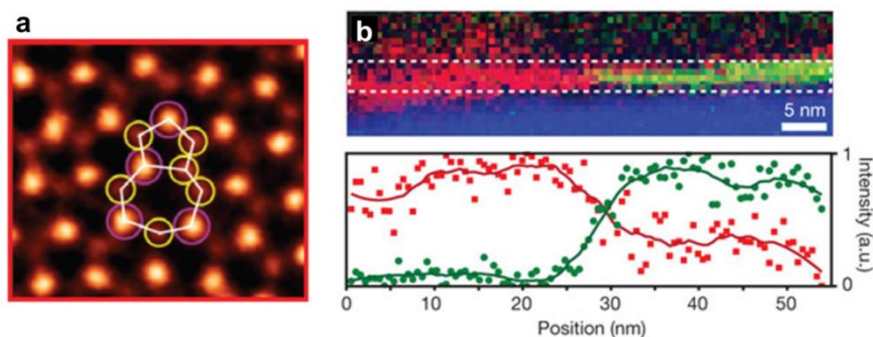


**Figure 2.1: STEM and EELS imaging of 2D materials**

(a) A STEM image of a defect (outlined) in single-layer MoS<sub>2</sub>. This image also illustrates the difference in contrast between atoms with different atomic weights with STEM [2]. (b) A cross-sectional EELS map of the concentrations of graphitic carbon (red) and boron (green) near a graphene/*h*-BN lateral junction [3].

First, we will discuss electron microscopy techniques, which are invaluable for obtaining high resolution structural information about 2D samples. In general, the spatial resolution of a microscope is limited by the wavelength of its probe. Electrons have wavelengths of roughly 1-10 pm depending on their accelerating voltage, enabling extremely high spatial resolution imaging with electron microscopy. Due to current limitations of electron optics, the resolution limit of electron microscopes is orders of magnitude larger, but it is still possible to obtain atomic scale images with spatial resolution as small as ~100 pm.

In particular, the transmission electron microscope is an extremely powerful tool for producing structural and compositional mapping of materials on an atomic scale. Several different modes of operation are available, each with different capabilities. First, scanning transmission electron microscopy (STEM), where an incident electron beam is focused to a subnanometer-sized spot and raster scanned across the sample, has been used by a number of groups to produce atomic resolution images of 2D materials [4,5]. In this mode, the contrast of each atom increases with increasing atomic number, allowing different elements to be distinguished in 2D materials such as TMDs [2,6] and *h*-BN [4]. STEM is particularly useful for imaging lattice defects, such as grain boundaries [2,5-7]. Figure 2.1a shows a defect in single layer MoS<sub>2</sub> which was imaged with STEM, and also illustrates the contrast difference between the heavy Mo (bright) and light S (dark) atoms.

Electron energy loss spectroscopy (EELS) is a complementary spectroscopy technique to STEM. By measuring the energies lost by the monochromated electrons transmitted through the sample, EELS can determine local information about atomic composition and bonding. For example, subtle changes in EELS spectra can be used to differentiate between graphitic and amorphous carbon [3,8]. A higher signal to noise ratio EELS signal can be obtained for thicker materials, and thus EELS has been used to map the chemical composition in cross sections of lateral [3] and vertical [8,9] 2D heterostructures. Figure 2.1b shows a cross-sectional EELS map of a patterned lateral graphene/*h*-BN junction, plotting the concentrations of graphitic carbon (red) and boron (green). Here, EELS was used to establish a junction width between the patterned graphene and *h*-BN regions of <10 nm.

Conventional transmission electron microscopy (CTEM, or simply TEM) is also very valuable for 2D materials characterization. In this mode of imaging, a larger area of the sample

(e.g. several microns) is illuminated with the electron beam. Like STEM, aberration corrected high resolution TEM (HR-TEM) can also be used to obtain atomic resolution images of 2D materials [10-12], although it is more difficult to quantitatively interpret the image contrast in this mode. Another particularly useful feature of TEM for 2D materials characterization is the ability to obtain an electron diffraction pattern, which can be used to identify the local crystallinity and orientation of the sample [5,7]. Single crystals of monolayer graphene, *h*-BN, and TMDs all produce six-fold symmetric diffraction patterns.

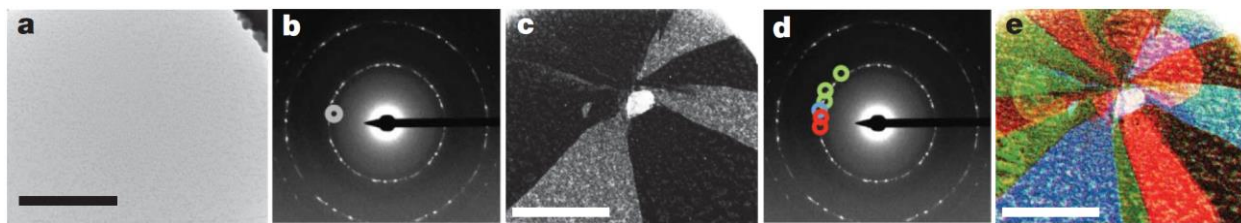


**Figure 2.2: Dark-field TEM imaging of graphene**

(a) A conventional TEM image of a suspended graphene film, which is largely featureless and transparent to the electron beam. (b) An electron diffraction pattern from the same region, showing many sets of six-fold symmetric diffraction spots. The circle indicates the location of the aperture for (c), the dark-field image of the grains corresponding to the selected crystalline orientation. (d) and (e) illustrate false colored imaging of graphene grains with many different orientations. Scale bars 500 nm [5].

A related mode of operation, dark-field TEM imaging (DF-TEM), can be used to visualize the individual crystalline grains of 2D materials (Figure 2.2) [5,13,14]. After obtaining a diffraction pattern from the sample, an objective aperture is placed in the diffraction plane so that only electrons scattered in a certain direction are collected. In the final real space image, only those regions with the selected orientation are visible. This technique can be extended to identify all of the grains in the sample by taking a series of images where the aperture is moved to select different diffraction spots. DF-TEM can also be used to identify the relative orientations of stacked layers; for misoriented layers, the grains corresponding to two different diffraction

spots will overlap spatially. Typically, these images are compiled into a composite which is false colored by orientation, as in Figure 2.2e. DF-TEM will be used extensively in this dissertation to characterize the grain structure and stacking order in a variety of 2D samples.

The biggest disadvantage to all transmission electron microscopy techniques is that they have restrictive sample preparation requirements, which can limit their use in materials characterization. First, the entire sample must be transparent to electrons, which limits the potential substrates to very thin membranes (e.g. 5-10 nm of silicon nitride) or suspended samples. The samples should also be free of contaminants, particularly hydrocarbon residues, for atomic resolution STEM and HR-TEM imaging. All electron microscopy techniques are also potentially destructive: they can deposit amorphous carbon on the sample surface, dope the sample, and cause damage to the lattice, depending on the material being studied and the accelerating voltage of the electron beam.

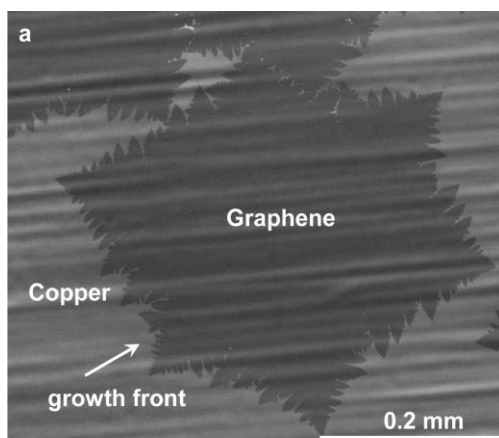


**Figure 2.3: SEM of graphene**

A SEM image of CVD graphene on its copper growth substrate [15]

A final electron microscopy technique of note is scanning electron microscopy (SEM), where the electron beam is focused and raster scanned along the surface of the sample, and

backscattered electrons are detected. SEM does not have the stringent sample preparation requirements of TEM, although samples must be reasonably metallic or they will quickly accumulate charge (insulating and semiconducting 2D materials on metallic substrates generally can be imaged with SEM). The spatial resolution of this technique is lower than that of TEM, typically tens of nanometers. For 2D materials, SEM is most useful for quick characterization of CVD samples on their metallic growth substrates (Figure 2.3). While the contrast in these images is not easy to interpret quantitatively, single and multilayer regions can be identified quickly with high spatial resolution.

### **2.3 | Scanning probe microscopy**

Next, we discuss a second class of imaging tools, collectively known as scanning probe microscopy (SPM) techniques. For each, a sharp tip is brought into close physical contact with the surface of a sample, and raster scanned along the surface to produce an image. Scanning probe techniques are most commonly used to image surface topography (AFM) or free electron density (STM), but can be adapted to image a variety of other properties, such as friction between the tip and the sample [16] or surface potential [17]. The most significant disadvantage to all scanning probe techniques is that feedback is required to regulate the distance between the tip and the sample as the tip is scanned, which limits the rate at which images can be acquired.

Atomic force microscopy (AFM) uses a tip which is typically tens of nanometers in radius, and is attached to the end of a small cantilever. For tapping mode AFM, the cantilever is driven to oscillate near its resonant frequency, and the amplitude of the resulting oscillation is monitored as the tip is raster scanned over the sample. The oscillation amplitude decreases sensitively as a function of the distance between the tip and the sample, and a feedback loop is

used to keep the amplitude constant as the tip scans. Because of the close relationship between the oscillation amplitude and the tip-sample distance, AFM thus provides quantitative imaging of the sample topography.

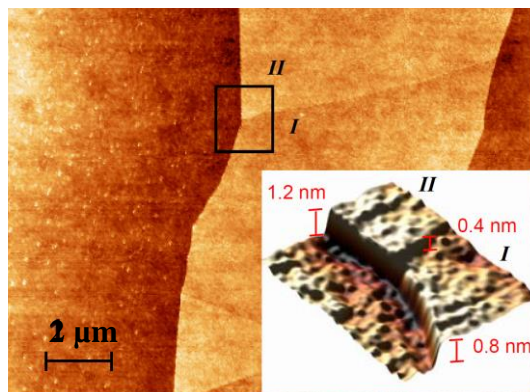


**Figure 2.4: AFM of graphene**

An AFM image of the surface topography of a piece of mechanically exfoliated graphene, showing that the sample is clean and conformal with the intrinsic roughness of the SiO<sub>2</sub> substrate. Region I is thought to be single-layer graphene despite its measured height (0.8 nm) being twice that of the known interlayer spacing of graphite [18].

Although the lateral resolution of AFM is limited by the tip radius, the height resolution is subnanometer, and individual layers of graphene and other 2D materials can be resolved (Figure 2.4). However, AFM is not a reliable technique for measuring the thickness of a single layer of graphene. Differences between the tip-sample interactions on the 2D material surface and the bare substrate can introduce height artifacts, and it is also common for 2D materials to retain a thicker layer of adsorbates or contaminants than the bare substrate [18,19]. On the other hand, AFM is a valuable technique for characterizing nanoscale surface roughness of 2D materials on various substrates [20], and for quantifying the contaminants which remain on a sample after transfer [21]. Unlike electron microscopy techniques, AFM can be performed on a variety of substrates.

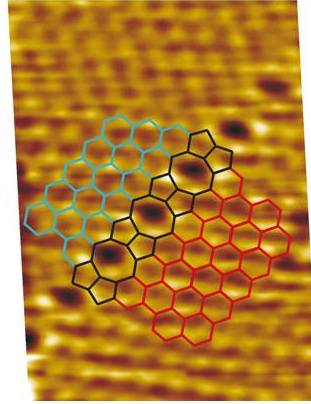


**Figure 2.5: STM of graphene**

An atomic scale image of an extended line defect of CVD graphene on its nickel growth substrate, obtained with STM. [22]

A second scanning probe technique is scanning tunneling microscopy (STM). Here, the tip is atomically sharp and metallic, and a current tunnels between the tip and the sample when the tip is very close to the sample surface. The magnitude of the tunneling current is exponentially sensitive to the distance between the tip and the sample, and can be used as a feedback mechanism to map surface topography on an atomic scale (Figure 2.5). The measured quantity is not the direct physical topography of the sample, but is related to the local free electron density at the sample surface. In addition, scanning tunneling spectroscopy (STS), where the tunneling current at a point is measured as a function of tip-sample voltage, is a sensitive probe of the local density of states spectrum. STM and STS have been used for a variety of studies of 2D materials, such as the electronic properties of individual defects [22], interstitial dopants in graphene [23] or the atomic structure of graphene/*h*-BN lateral heterojunctions [24,25]. Although STM is very informative, it is limited to very small areas of the sample and requires a pristine surface.

## 2.4 | Optical microscopy

Optical microscopy techniques, a third class of imaging tools, have several advantages over both electron microscopy and scanning probe techniques. Not only can images be acquired rapidly, allowing large-scale imaging with high throughput, but optical microscopy also requires minimum sample preparation and causes little to no damage to the sample. Light can interact with a sample through a variety of processes, which can provide spectroscopic information probing the material's electronic and vibrational properties.

However, the most significant limitation of optical microscopy is that the spatial resolution of the collected images is limited by the wavelength of the light, which is much larger than the wavelength of an electron. In practice, the resolution limit is a few hundred nanometers for visible light illumination, which is orders of magnitude larger than many features of interest in 2D materials, such as single atomic defects or individual grain boundaries. On the other hand, this resolution is still significantly smaller than the typical grain size of high quality CVD-grown 2D materials, and is more than sufficient for many studies.

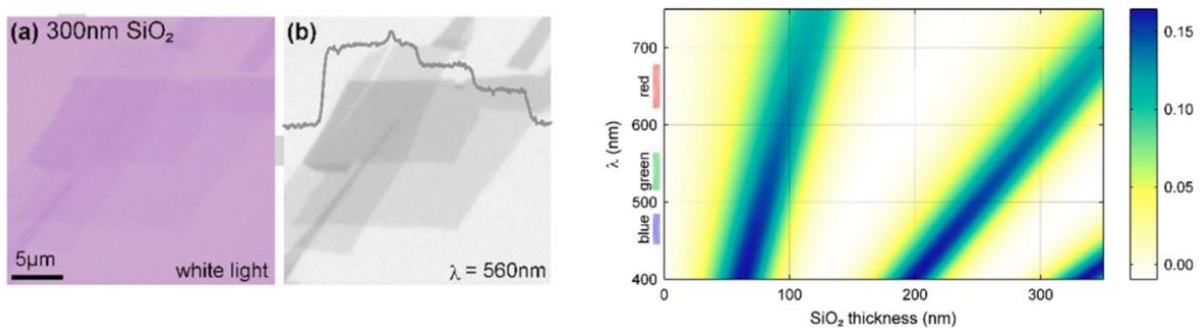


**Figure 2.6: Making graphene visible**

(left) Color (a) and single wavelength (b) images of exfoliated graphene on a silicon wafer with a 300 nm SiO<sub>2</sub> layer. In both cases, single- and few-layer graphene are visible and can be differentiated. (right) A plot illustrating the contrast of graphene (color scale) at different wavelengths ( $y$ -axis) and SiO<sub>2</sub> thicknesses ( $x$ -axis) [26].

One of the most crucial applications of optical imaging for the field of 2D materials research was also one of the simplest, and this example highlights the benefits of the high throughput and simplicity of optical microscopy. Particularly during the early development of the 2D materials field when graphene samples were produced by mechanical exfoliation, it was necessary to be able to search a large region of a substrate quickly in order to identify areas of single- and few-layer graphene among many thicker regions. This is difficult because a single layer of graphene absorbs only 2.3% of visible light. However, if silicon with an appropriate oxide thickness is used as a substrate, interference effects can increase the contrast of the single-layer graphene to roughly 10% under white light illumination, making it visible by eye (Figure 2.6) [26,27]. This technique allowed the rapid identification of single- and few-layer exfoliated graphene for use in further studies, and is still widely used for imaging both CVD graphene and many semiconducting 2D materials after transfer. However, we note that this technique is poorly suited for identifying single- and few-layer *h*-BN, which is transparent at all visible energies; we will discuss this point in more detail in Chapter 3.

While white light microscopy is sufficient for certain applications, it is not sensitive enough to image the complex variations in composition and structure which can be present in 2D materials. Instead, as we will discuss in the following chapters, understanding how a 2D material interacts with light as a function of wavelength can provide very detailed information about its composition, number of layers, stacking structure, and defect density. The spectral response of a material can be obtained by scanning the optical excitation wavelength ( $\lambda_{\text{ex}}$ ) using a tunable source. At a fixed  $\lambda_{\text{ex}}$ , the spectrum of any emitted light from the sample can also be collected, providing information about inelastic optical processes such as photoluminescence and Raman

scattering. Microscopy techniques which provide both spatial and spectral information about a sample are referred to as *imaging spectroscopy* or *hyperspectral imaging* techniques.

Both electron microscopy and scanning probe techniques can also provide information about the energy-dependent response of a sample. However, EELS suffers from low spectral resolution (typically  $>0.1$  eV), and STS from a limited energy range (1-2 eV). On the other hand, wavelengths for optical characterization range from the near infrared ( $\sim 800$ - $2500$  nm, or 0.5-1.5 eV) and visible ( $\sim 400$ - $800$  nm, or 1.5-3 eV) to the ultraviolet ( $\sim 200$ - $400$  nm, or 3-6 eV), and a spectral resolution of  $<0.01$  eV is easily achievable. Thus, in addition to its high throughput and versatility, the large spectral range and high spectral resolution of optical microscopy are additional advantages to this class of characterization techniques.

## **2.5 | Outlook**

To summarize, we have reviewed three classes of imaging techniques: electron, scanning probe, and optical microscopy. While both electron microscopy and scanning probe techniques have provided direct images of a variety of atomic and nanometer-scale structural features in 2D materials, these non-optical techniques also have several disadvantages. Scanning probe techniques are generally slow, limiting their ability to characterize graphene over a large area, while electron microscopy techniques have the potential to alter or damage the sample. AFM and SEM provide limited information about atomic structure, while more informative techniques such as STM and TEM require restrictive sample preparation, precluding many device geometries. None of these techniques alone is sufficient to quickly and non-destructively image a large area 2D sample.

Optical microscopy has the potential to bridge this gap, and the high throughput, simplicity, and versatility of white light optical microscopy have already made it the tool of choice for simply visualizing CVD or exfoliated graphene on a silicon substrate. However, imaging spectroscopy is required in order to take full advantage of the sensitivity of optical microscopy. For this, hyperspectral microscopes can be designed to exploit the known optical responses of various 2D materials. Examples which we will discuss in the following chapters include the variations in the optical absorption spectra of 2D materials with different atomic compositions, such as graphene and *h*-BN, and the inelastic Raman scattering spectrum of graphene, which is sensitive to parameters such as point defect density, doping, strain, and stacking structure.

Next, these same microscopes can be used to quantitatively characterize the optical response of an arbitrary 2D material with unknown compositional or structural features. Combined with the direct, nanometer scale imaging capabilities of electron microscopy and scanning probe techniques, we can establish new relationships between the structure and properties of a variety of complex 2D materials, enabling the discovery of new physics and functionalities in these systems. In the following chapters, we will use DF-TEM imaging extensively to compare the grain structure and stacking orientations of our samples to their optical absorption and Raman scattering spectra. We will also use AFM to examine the effects of contaminants on the optical properties of our samples, and compare some of our optical data with previous STM and STS studies of similar systems.

Optical imaging spectroscopy is not a new concept, and a variety of imaging spectroscopy techniques have already been applied to 2D materials research. However, there are a number of specific technical challenges which have prevented these techniques from being

used to their full potential for characterizing complex 2D materials on a large scale. In **Chapters 3 and 4**, we discuss and address these challenges in order to adapt absorption spectroscopy and Raman spectroscopy, respectively, as diffraction-limited microscopy techniques optimized for 2D materials characterization.

## References

- [1] R. Havener, A. Tsen, H. Choi, and J. Park, *NPG Asia Materials* **3**, 91 (2011).
- [2] S. Najmaei *et al.*, *Nature Materials* **12**, 754 (2013).
- [3] M. Levendorf, C. Kim, L. Brown, P. Huang, R. Havener, D. Muller, and J. Park, *Nature* **488**, 627 (2012).
- [4] O. Krivanek *et al.*, *Nature* **464**, 571 (2010).
- [5] P. Huang *et al.*, *Nature* **469**, 389 (2011).
- [6] A. van der Zande *et al.*, *Nature Materials* **12**, 554 (2013).
- [7] K. Kim, Z. Lee, W. Regan, C. Kisielowski, M. Crommie, and A. Zettl, *ACS Nano* **5**, 2142 (2011).
- [8] L. Wang *et al.*, *Science* **342**, 614 (2013).
- [9] S. J. Haigh *et al.*, *Nature Materials* **11**, 764 (2012).
- [10] J. Meyer, C. Kisielowski, R. Erni, M. Rossell, M. Crommie, and A. Zettl, *Nano Letters* **8**, 3582 (2008).
- [11] A. Gibb, N. Alem, J. Chen, K. Erickson, J. Ciston, A. Gautam, M. Linck, and A. Zettl, *Journal of the American Chemical Society* **135**, 6758 (2013).
- [12] A. Hashimoto, K. Suenaga, A. Gloter, K. Urita, and S. Iijima, *Nature* **430**, 870 (2004).
- [13] L. Brown, R. Hovden, P. Huang, M. Wojick, D. A. Muller, and J. Park, *Nano Letters* **12**, 1609 (2012).
- [14] A. Tsen *et al.*, *Science* **336**, 1143 (2012).
- [15] X. Li, C. Magnuson, A. Venugopal, R. Tromp, J. Hannon, E. Vogel, L. Colombo, and R. Ruoff, *Journal of the American Chemical Society* **133**, 2816 (2011).
- [16] A. J. Marsden, M. Phillips, and N. R. Wilson, *Nanotechnology* **24**, 255704 (2013).
- [17] S. S. Datta, D. R. Strachan, E. J. Mele, and A. T. C. Johnson, *Nano Letters* **9**, 7 (2009).
- [18] Y. Zhang, Y. Tan, H. Stormer, and P. Kim, *Nature* **438**, 201 (2005).
- [19] K. Novoselov, A. Geim, S. Morozov, D. Jiang, Y. Zhang, S. Dubonos, I. Grigorieva, and A. Firsov, *Science* **306**, 666 (2004).
- [20] C. Lui, L. Liu, K. Mak, G. Flynn, and T. Heinz, *Nature* **462**, 339 (2009).
- [21] J. Song, F. Kam, R. Png, W. Seah, J. Zhuo, G. Lim, P. Ho, and L. Chua, *Nature Nanotechnology* **8**, 356 (2013).

- [22] J. Lahiri, Y. Lin, P. Bozkurt, I. Oleynik, and M. Batzill, *Nature Nanotechnology* **5**, 326 (2010).
- [23] L. Zhao *et al.*, *Science* **333**, 999 (2011).
- [24] P. Sutter, R. Cortes, J. Lahiri, and E. Sutter, *Nano Letters* **12**, 4869 (2012).
- [25] L. Liu *et al.*, *Science* **343**, 163 (2014).
- [26] P. Blake, E. Hill, A. Neto, K. Novoselov, D. Jiang, R. Yang, T. Booth, and A. Geim, *Applied Physics Letters* **91**, 063124 (2007).
- [27] K. Novoselov, D. Jiang, F. Schedin, T. Booth, V. Khotkevich, S. Morozov, and A. Geim, *PNAS* **102**, 10451 (2005).

## Chapter 3 : DUV-VIS-NIR HYPERSPECTRAL IMAGING

### 3.1 | Introduction

In this chapter, we describe a hyperspectral optical microscope whose excitation wavelength ( $\lambda_{\text{ex}}$ ) can be tuned continuously over an energy range of several electron volts (eV). By obtaining the spatially resolved transmission or reflection spectrum of a 2D sample, we can characterize and distinguish between regions with different optical absorption spectra. Here, we will focus on the use of our microscope to image 2D heterostructures with spatially varying composition, specifically patterned graphene/*h*-BN lateral junctions. However, the imaging and quantitative spectroscopy techniques we describe in this chapter can immediately be applied to many other 2D systems, and we will explore the use of this microscope to characterize the optical properties of twisted bilayer graphene (tBLG) over a large energy range in Chapters 5 and 6.

The challenge of building this microscope was to provide a large enough energy range to observe the relevant spectral features for a diverse group of 2D materials and 2D heterostructures. Standard optical microscopes are designed to operate using visible or infrared light at energies below  $\sim 3$  eV. However, many 2D materials contain important features in their optical absorption spectra at much higher energies, as we discuss in more detail below. In particular, *h*-BN is an insulator which is completely transparent at energies below 6.1 eV, or at wavelengths longer than 203 nm. Operating at these deep ultraviolet (DUV) energies required the careful selection of the illumination source, optical elements, and array detector for our setup.

Our DUV-Vis-NIR hyperspectral microscope provides imaging and spectroscopy at energies of up to 6.2 eV, allowing direct optical imaging of *h*-BN at its absorption peak for the first time, and comprehensive, all-optical mapping of chemical composition in graphene/*h*-BN

lateral heterojunctions. With the addition of dark-field transmission electron microscopy (DF-TEM), we obtain quantitative structure-property relationships, confirming the formation of interfaces in graphene/h-BN lateral heterojunctions which are abrupt on a submicron scale. In particular, we outline a procedure for obtaining the quantitative full optical function ( $\sigma$ ) of 2D materials which sit on thin silicon nitride membranes, a substrate which is also compatible with TEM imaging. We also perform hyperspectral imaging of samples that are supported on a nontransparent silicon/SiO<sub>2</sub> substrate, enabling facile fabrication of atomically thin electronic devices with known composition and structure. The majority of this chapter is reproduced from [1], as well as certain sections from [2].

### 3.2 | Absorption spectroscopy

Optical absorption spectroscopy can provide information about the band structure of a material over an energy range of several eV, and serves as a useful fingerprint to identify the composition of a material. When any material absorbs a photon, a transition can only occur between two states in the electronic band structure of the material with the same momentum. Thus, optical absorption is closely related to the density of states of a material. Because of this, materials with varying band gaps, such as metals, semiconductors, and insulators, typically have very distinct optical absorption spectra [3].

The optical response of any material is actually described by its optical conductivity ( $\sigma$ ) through the equation  $J = \sigma E$ , where  $J$  is the current density in the material and  $E$  is the time-dependent electric field of the incoming light. In general,  $\sigma$  is an imaginary quantity whose real part is proportional to the optical absorption of the material, and whose imaginary part is proportional to its permittivity. Although  $\text{Re}[\sigma]$  is often the quantity of interest,  $\text{Re}[\sigma]$  and  $\text{Im}[\sigma]$

are linked through mathematical rules known as the Kramers-Kronig relations [4], such that a material with features (such as peaks) in its absorption spectrum will also exhibit corresponding features in its  $\text{Im}[\sigma]$  spectrum.

This distinction is important because absorption (i.e.  $\text{Re}[\sigma]$ ) is never measured directly. Rather, the measured quantity is the transmission through or reflection from the sample as a function of wavelength. The case of 2D materials is further complicated by the fact that 2D samples are typically supported by a bulk substrate. Depending on the substrate used, the measured reflection or transmission spectrum of the entire sample may be a function of both  $\text{Re}[\sigma]$  and  $\text{Im}[\sigma]$  of the 2D material. For some substrates, such as transparent fused silica, it is straightforward to convert the transmission or reflection spectrum of the 2D material and its supporting substrate to  $\text{Re}[\sigma]$  of the 2D material alone [5], while for others, such as a silicon wafer with an oxidized surface layer, it is much more difficult. These challenges will be discussed in more detail in Section 3.5.

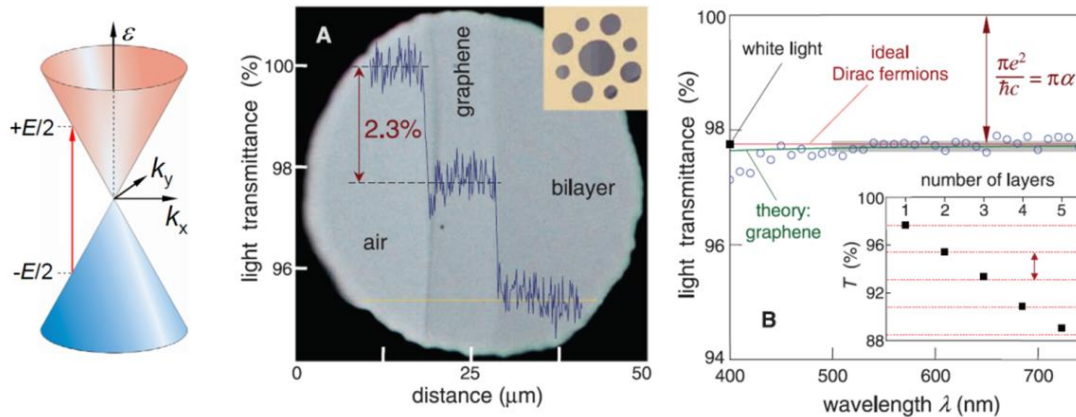


**Figure 3.1: Optical absorption in graphene**

(left) A schematic of an allowed optical transition in graphene. (center) An image of transmitted light through a suspended single and bilayer graphene sample, and (right) a plot of the transmittance vs. wavelength, illustrating that this quantity is constant over the visible range. [6]

The optical absorption spectrum of graphene is unique due to the cone-like linear dispersion of its conduction and valence bands near its charge neutrality (Dirac) point (Figure 3.1). Single layer graphene has a uniform optical absorption at most visible and near infrared wavelengths [6] of 2.3% or  $\pi\alpha$ , where  $\alpha$  is the fine structure constant, while thin multilayers exhibit multiples of 2.3% absorption (Figure 3.1 right, inset). While 2.3% absorption is nearly transparent to the eye, it is fairly large considering that the material is only one atom thick. The finite visible light absorption of graphene enabled the use of a simple optical microscopy technique to visualize it, as described in Chapter 2.

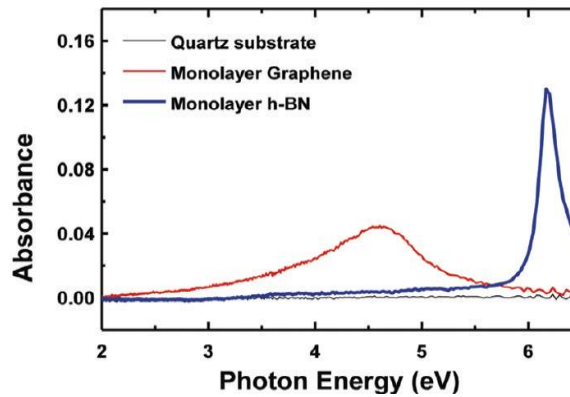


**Figure 3.2: UV absorption spectra of graphene and *h*-BN**

The UV absorption spectrum of monolayer graphene and *h*-BN transferred to a quartz substrate, measured across a large area (several mm) with a UV-Vis-NIR spectrometer. We note that the low energy optical response of graphene (red) is not accurate in this particular measurement, as monolayer graphene has a constant 0.023 absorbance at visible energies (see above). [7]

On the other hand, semiconducting and insulating materials are generally transparent at energies below their band gap, and exhibit an absorption peak at their optical band gap energy, as well as other higher energies where the band structure contains van Hove singularities (vHSs). In particular, *h*-BN is transparent at energies of up to 6.1 eV [1,7] due to its large band gap, as shown by the optical absorption spectrum in Figure 3.2. This makes monolayer *h*-BN very

difficult to visualize with visible light [8]. A high energy, saddle point vHS is also present in the band structure of graphene, leading to a broad, asymmetric peak in its absorption spectrum near 4.6 eV [9,10].

Absorption spectroscopy has been an essential tool for studying the band structures and many-body interactions in several 2D materials, and has revealed a variety of rich physics in these low-dimensional systems. However, most absorption studies of 2D materials, particularly those encompassing UV wavelengths, have been bulk [7] or point [9,10] measurements. Here, we build an optical microscope capable of DUV-Vis-NIR imaging with submicron spatial resolution, allowing us to take advantage of the sensitivity of absorption spectroscopy in order to study 2D materials with complex structural and compositional variations.

### **3.3 | Details of the DUV-Vis-NIR microscope**

Our DUV-Vis-NIR microscope enables hyperspectral imaging of 2D heterostructures over the entire spectral range of 1.2 to 6.2 eV while maintaining submicron spatial resolution. While similar DUV-Vis-NIR hyperspectral imaging systems are commercially available [11], our main goal with our homebuilt system was a wavelength range which encompassed the 6.1 eV band gap of *h*-BN, allowing us to identify and image this material at a wavelength where it was highly absorptive. We have achieved this goal by careful selection of the microscope components, described below.

In general, optical imaging techniques are performed using a microscope that is equipped with an excitation light source and delivery optics (illumination), and an optical detector and collection optics (detection). The illumination and detection geometries and the specific components chosen for each optical element depend on the intended application of the

microscope. Our priority was to choose components which were compatible with DUV light, and which reduced or eliminated chromatic aberrations. To this end, we removed all refractive elements and DUV-opaque glass (such as BK7) from the light path, and used exclusively mirror-based (“catoptric”) [12] optics for light focusing and image formation.

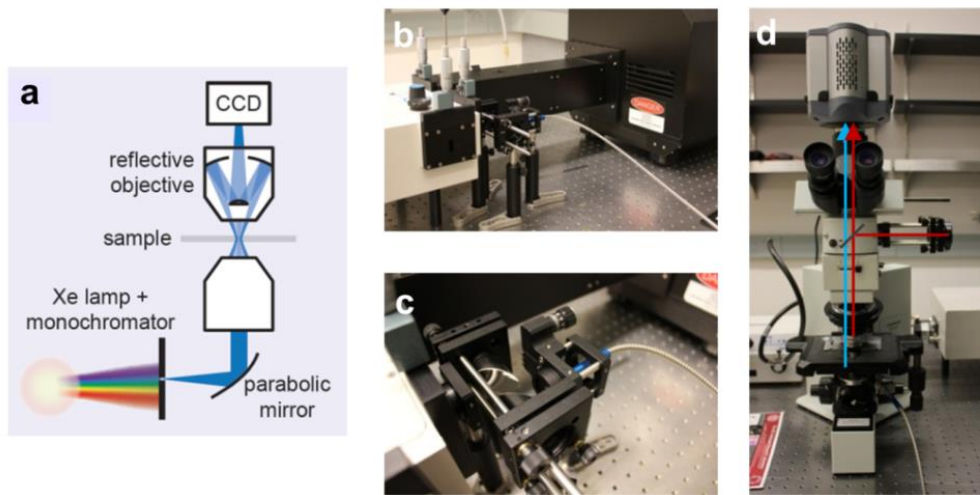


**Figure 3.3: Schematic and photographs of DUV-Vis-NIR microscope**

(a) A schematic of the microscope. (b) The 1000W Xe lamp housing (black, right) and monochromator (white, left). (c) A close up image of the parabolic mirrors used to align and focus the light from the monochromator into the solarization-resistant fiber. (d) An early version of the hyperspectral microscope. Two illumination schemes are possible, transmission (blue) or reflection (red), depending on where the fiber is attached to the microscope. The image is detected by the CCD camera (top), which has a detection range of 200-1000 nm.

For illumination, we chose a UV enhanced 1000 W Xe arc source with a monochromator (typically set to 2 nm spectral resolution) to select a specific wavelength (Figure 3.3). Light exiting the monochromator is focused with parabolic mirrors (Figure 3.3b) into a multimode fiber designed not to degrade in performance under exposure to DUV light (solarization-resistant), which delivers the light to the microscope.

The final key component of the illumination path is a reflective (Schwarzschild) objective (Figure 3.4). There are two issues for using typical refractive microscope objectives for UV

imaging. First, as noted above, many glasses strongly absorb UV light. Second, even DUV-compatible glasses such as pure fused quartz have high dispersion at UV wavelengths, meaning that their refractive indices change rapidly as a function of wavelength. As a result, the focus of the microscope would have to be adjusted continuously as  $\lambda_{\text{ex}}$  was varied. Our choice of a reflective objective avoids both of these problems. Collimated light from the fiber is focused by the objective onto the sample. The size of the illuminated region is determined by the finite size of the incoherent light source, which is the core diameter of the delivery fiber in this case. In our microscope, this results in a  $\sim 70$   $\mu\text{m}$  diameter circle of illumination on our sample surface (Figure 3.5). The spatially uneven illumination of our sample is one of the disadvantages of our design, but all of our images are normalized with respect to a bare substrate to correct for variations in illumination intensity.

Our microscope is designed to work in one of two modes: reflection or transmission. In reflection mode (see red line in Figure 3.3, as well as Figure 3.9), a DUV 50/50 beamsplitter directs the light to illuminate the sample through the objective, after which the reflected light from the sample is collected through the same objective and directed back through the microscope. In transmission mode, a second reflective objective below the sample delivers the light, acting as a condenser. In both cases, the light from the sample is focused onto a one megapixel charge-coupled device (CCD) for detection, with an effective magnification of  $\sim 100\times$ . Our CCD detector is UV enhanced, allowing detection from 200-1000 nm. For wavelengths below 250 nm, an additional DUV bandpass filter is required to remove stray visible light, which originates from the monochromator and/or fiber. For wavelengths from 500-1000 nm, a single long pass filter may be used to remove the light from second order diffraction ( $\lambda = \lambda_{\text{ex}}/2$ ) in the monochromator.

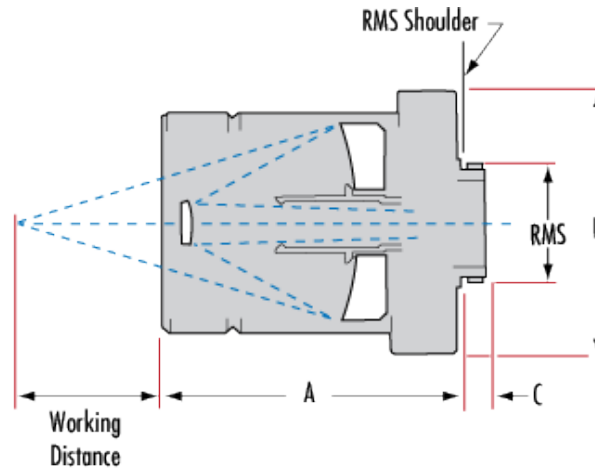


**Figure 3.4: Reflective objective**

A cross-sectional schematic of the reflective objective used our microscope, taken from the manufacturer [13]. The white regions are mirrors, while the blue dashed line is the path of the light. Collimated light enters the objective through the right side and is focused by the curved mirrors onto a point on the left. The central mirror (left) acts to obscure light traveling directly down the center of the objective, and the focused light leaving the objective has the form of a hollow cone.

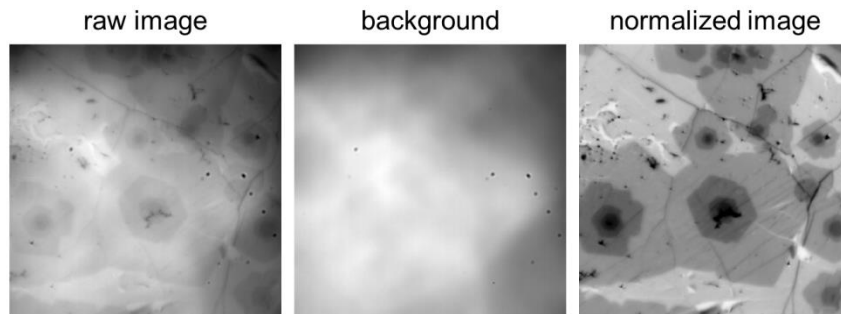


**Figure 3.5: Sample illumination and image normalization**

An image of multilayer graphene in transmission mode before and after normalization.

Finally, the spatial resolution of an optical microscope is typically determined by the numerical aperture (N.A.) of the objective, which is the sine of the angle ( $\theta$ ) of the cone of light which can be collected from a point on the sample. However, the central mirror of a Schwarzschild objective obscures the central portion of the collected light cone (Figure 3.4). The result for imaging is that the performance of the objective is somewhat degraded, compared to that of a refractive objective with the same N.A., when imaging larger features ( $>\lambda/\text{N.A.}$  for our

objective, which has an obscuration of 16.7%). However, the performance of both reflective and refractive objectives with the same N.A. is approximately the same close to the Abbe diffraction limit (feature size of  $\lambda/2\text{N.A.}$ ) [14]. The Abbe limit for a refractive objective with N.A. = 0.65 is  $0.77\lambda$ , and so we approximate the resolution of our reflective objective as  $\lambda$  (30% larger).

### 3.4 | Monochromatic and hyperspectral imaging

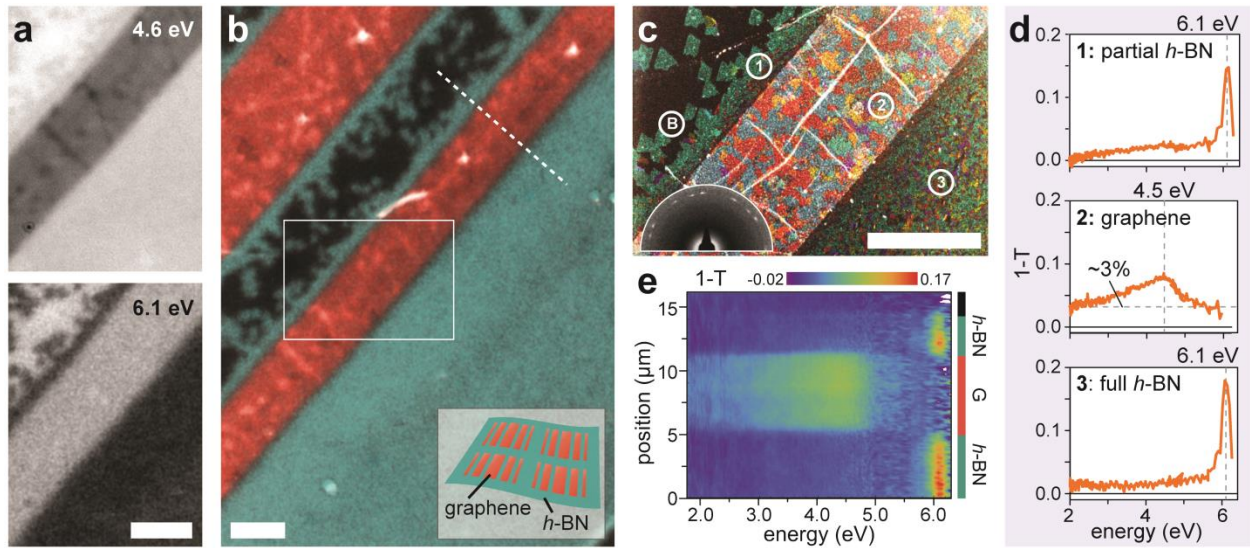


**Figure 3.6: Imaging and spectroscopy of graphene/*h*-BN heterostructures**

(a) Optical transmission images of a graphene/*h*-BN lateral heterostructure at two different energies, showing energy-dependent features. (b) False color image combining the images from (a), showing a clear stripe pattern which matches the (inset) intended design. (c) DF-TEM image of the same sample (from boxed region in (b)), showing the grain structure of the materials present, which reveals a clear junction. (inset) A representative background subtracted diffraction pattern from a junction region of the same sample, showing diffraction spots consistent with both graphene and *h*-BN. (d) Transmission spectra from three numbered regions outlined in (c) (with respect to the bare substrate, “B”), corresponding to partial and full *h*-BN growth and graphene. (e) Transmission spectra taken along the dashed line in (b), showing clear *h*-BN and graphene strips with little compositional mixing. All scale bars are 5  $\mu\text{m}$ .

We next detail the use of our microscope to study graphene/*h*-BN lateral heterostructures. The samples studied in our work were produced by the patterned regrowth method [15] and are supported either by 10 nm thick silicon nitride (SiN) membranes [16] for both optical and TEM

imaging, or by silicon substrates with thermal oxide. Figure 3.6 shows optical transmission images of a graphene/*h*-BN lateral heterojunction transferred to a SiN membrane substrate with distinct, energy dependent features. Different regions appear darker (with reduced transmission) at 4.6 and 6.1 eV, which correspond to the known absorption peaks of graphene [9,10] and *h*-BN [7], respectively. Because our microscope has no chromatic aberrations, such images can be easily combined to generate a false color composite, shown in Figure 3.6b. This large-scale image reveals lateral junctions whose pattern matches the intended design (Figure 3.6b, inset), and suggests areas of both full and partial *h*-BN growth immediately adjacent to graphene strips. The junction formation is confirmed by a DF-TEM [17] image (Figure 3.6c) of same device from Figure 3.6b (boxed region), in which different colors indicate domains of different crystalline orientations. This image shows clear lines across which the domain structure changes abruptly, and confirms that both graphene and *h*-BN are polycrystalline single layers. We note, however, that our DF-TEM data alone cannot definitively distinguish between graphene and *h*-BN, because the diffraction patterns from both materials have the same symmetry and very similar lattice constants, as shown in a diffraction pattern from a junction region containing both materials (Figure 3.6c, inset).

The spatially-resolved atomic composition is confirmed by full spectral measurements (Figure 3.6d and Figure 3.6e). Figure 3.6d shows transmission spectra taken from several 1  $\mu\text{m}$  diameter spots (outlined in Figure 3.6c), extracted from hundreds of transmission images of the same region measured while continuously varying the photon energy from 1.8 to 6.2 eV. The majority of these hyperspectral images can be acquired within minutes, with an acquisition time per frame of <1 second for wavelengths above 250 nm, increasing to 1-2 minutes near 200 nm. Here, we plot 1-T, the transmission contrast (T defined as  $I/I_0$ , where  $I_0$  is the transmission

intensity through the bare substrate, and  $I$  is the intensity through the substrate plus sample), which is approximately equal to the absorption of the sample in most cases. Regions 1 and 3 exhibit a sharp, narrow peak near 6.1 eV, consistent with *h*-BN [7], while region 2 exhibits a broad, asymmetric peak near 4.5 eV with roughly constant 1-T at lower energies, consistent with graphene [6,9,10]. These results provide the most direct confirmation of our assignments of the composition in each area and suggest high qualities of graphene and *h*-BN. Furthermore, a two-dimensional plot of 1-T vs. energy across the graphene/*h*-BN heterojunction (Figure 3.6e) suggests that the transition between the graphene and *h*-BN is abrupt on a micron scale, and that each region exhibits a homogeneous optical spectrum, suggesting little compositional mixing. Thus, our graphene/*h*-BN heterostructure behaves as designed; additionally, we note that the optical response of the single-layer *h*-BN is similar for both partial and full growth regions with different grain structures, suggesting it is independent of grain size from hundreds of nm to ~1  $\mu\text{m}$ .

### 3.5 | Quantitative absorption spectroscopy

Our microscope also provides quantitatively accurate, spatially resolved measurements of the complex optical conductivity ( $\sigma$ ) of 2D materials (or permittivity,  $\varepsilon = i\sigma/\omega$ ). Figure 3.7 shows the real and imaginary parts of  $\sigma$  from our single-layer graphene and *h*-BN. These values were extracted from transmission and reflection images of the same sample, and the known optical parameters and geometry of the SiN substrate, which are discussed in more detail below.

In particular, we found that while 1-T of an atomically thin film on a thin ( $\ll \lambda$ ) membrane is approximately proportional to the film's absorption (or  $\text{Re}[\sigma]$ ), the reflection contrast 1-R (where R is defined analogously to T) is instead approximately proportional to

$\text{Im}[\sigma]$ . Figure 3.8 shows the calculated contrast of an atomically thin (0.34 nm) film in transmission and reflection modes on a 10 nm thick SiN membrane at 2.5 eV as a function of  $\text{Re}[\sigma]$  and  $\text{Im}[\sigma]$  of the atomically thin film. This calculation demonstrates that there is an approximately linear relationship between contrast and  $\text{Re}[\sigma]$  in transmission mode, and between contrast and  $\text{Im}[\sigma]$  in reflection mode. Additionally, there is much less variation in contrast when the opposite parameter ( $\text{Im}[\sigma]$  in transmission mode or  $\text{Re}[\sigma]$  in reflection mode) is varied.

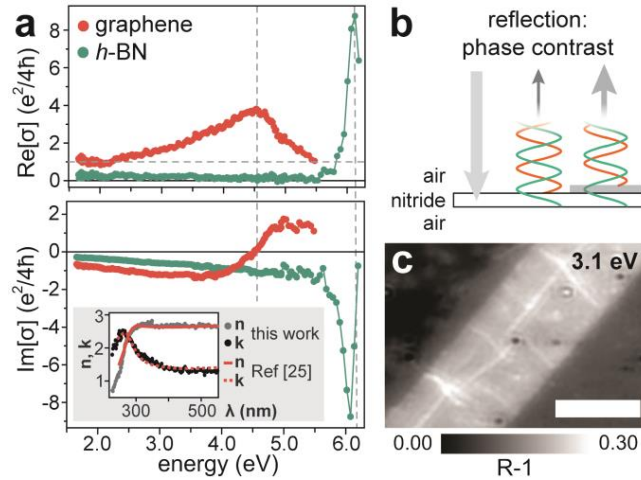


**Figure 3.7: Quantitative calculation of intrinsic optical conductivity**

(a) Measured real and imaginary parts of the optical conductivity ( $\sigma$ ) of single-layer CVD graphene and  $h$ -BN. (inset) Measured complex refractive index ( $n+ik$ ) of CVD graphene (dots), compared with previous work (lines) [18]. (b) Schematic illustrating phase contrast mechanism for reflection imaging of atomically thin films on a thin silicon nitride membrane (membrane thickness enlarged for clarity). (c) Reflection image of graphene/ $h$ -BN junction (same region as Figure 3.6c), showing that  $h$ -BN is visible far from its absorption peak in this mode (scale bar  $5\mu\text{m}$ ).

A more intuitive explanation for this unusual effect is that the reflections from the front and back of the thin membrane have opposite phase, interfering destructively [19]; the atomically thin film acts to alter this phase difference, typically increasing reflection, to a degree which depends on its thickness and dielectric constant (or  $\text{Im}[\sigma]$ ) (Figure 3.7b). Due to this effect,  $h$ -BN is clearly visible in reflection mode even at low energies (Figure 3.7c).

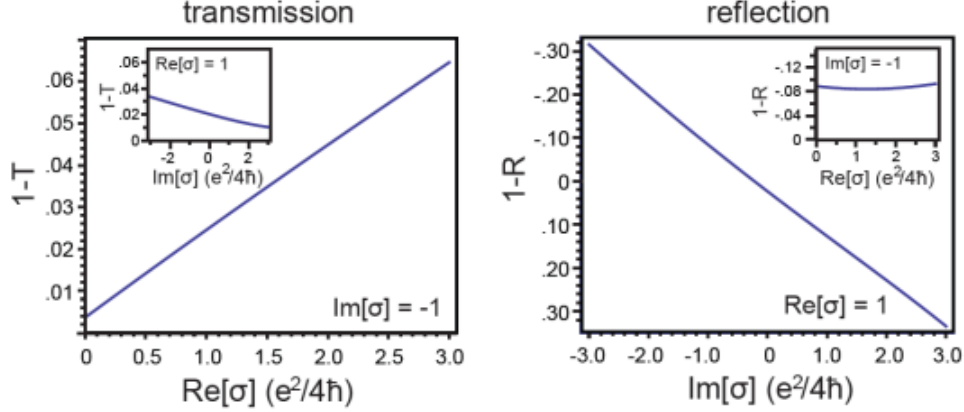


**Figure 3.8: Contrast as a function of  $\text{Re}[\sigma]$  and  $\text{Im}[\sigma]$**

Calculated contrast for an atomically thin film in (left) transmission and (right) reflection mode on a 10 nm thick silicon nitride membrane. For transmission (reflection) mode, the contrast is plotted as a function of  $\text{Re}[\sigma]$  ( $\text{Im}[\sigma]$ ) while  $\text{Im}[\sigma]$  ( $\text{Re}[\sigma]$ ) is held constant. In the insets,  $\text{Im}[\sigma]$  ( $\text{Re}[\sigma]$ ) varies while  $\text{Re}[\sigma]$  ( $\text{Im}[\sigma]$ ) is constant.

To calculate the complex  $\sigma$  of our atomically thin samples, we model our substrate + sample as a series of thin films using the transfer matrix formalism [20], and solve simultaneously for the values of  $\text{Re}[\sigma]$  and  $\text{Im}[\sigma]$  which best fit our transmission and reflection data. We set the incident angle of the unpolarized light in our model to  $30^\circ$  from the normal (which is the average incident angle produced by our reflective objective), and we assume that a single layer of graphene or *h*-BN has a thickness of 0.34 nm, close to the interplanar spacing of both materials [21,22]. We also find it necessary to add an additional layer to our thin film model to account for material trapped under the 2D film and/or adsorbates [23], with a thickness of 1-2 nm, to obtain consistent and reasonable results (examples of which are discussed below) when calculating  $\sigma$  of the atomically thin film. Adding this extra layer effectively increases our calculated value of  $\text{Im}[\sigma]$  by a constant, with little effect on  $\text{Re}[\sigma]$ .

For simplicity, we assume that the debris is only trapped under the film, not adsorbed on top of it, and that  $\sigma(\lambda)$  of the debris is that of PMMA [24]. We choose the thickness of the debris layer such that our calculated  $\text{Im}[\sigma]$  of the atomically thin film meets several criteria: 1.  $\text{Im}[\sigma]$  of

Bernal-stacked bilayer graphene is approximately twice that of single-layer graphene, when applicable; 2. The real part of the permittivity ( $\epsilon = i\sigma/\omega$ ) is roughly constant as a function of energy away from a resonance; 3. The real part of the refractive index  $n = \text{Re}[\epsilon^{1/2}]$  at low energies is consistent with literature values for single-layer graphene [21] and bulk *h*-BN [25]. Without the extra layer in our model, these criteria are not met. The debris thicknesses that best meet these criteria for the graphene/*h*-BN samples discussed in this chapter are 1 nm for the *h*-BN and 2 nm for the graphene.

This debris layer introduces uncertainty into our calculation of  $\text{Im}[\sigma]$  for our atomically thin film. Particularly, the dispersion of the debris is unknown, and this will likely introduce the greatest uncertainty in  $\text{Im}[\sigma]$  at high energies where the dispersion of different insulating materials can vary greatly. Full Kramers-Kronig analysis [4] may be useful in the future to find a consistent  $\sigma(\lambda)$  for all materials present.

Despite this uncertainty, the full optical function we calculate for CVD graphene matches previous, Kramers-Kronig consistent measurements of its refractive index [18] ( $n+ik = \epsilon^{1/2}$ ) (Figure 3.7a, inset). Our data in Figure 3.7a also provide complete quantitative measurements of  $\sigma$  for single-layer *h*-BN for the first time, and allow evaluation alongside that of CVD graphene.  $\text{Re}[\sigma]$  of single-layer *h*-BN peaks at  $\sim 9 e^2/4\hbar$  (corresponding to  $\sim 20\%$  absorption) for  $6.11 \pm 0.03$  eV, and  $|\text{Im}[\sigma]|$  peaks at a slightly lower energy with a similar height. Significantly, the accurate knowledge of  $\sigma$  for arbitrary atomically thin films enhances the capabilities of our microscope, because it allows us to predict the appearance of the same films on more complicated or non-transparent substrates for all-optical identification, as detailed in the following section.

### 3.6 | Imaging on silicon substrates

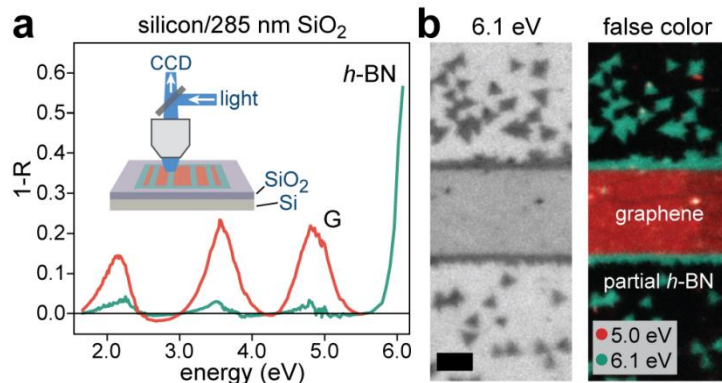


**Figure 3.9: Reflection spectroscopy on Si/SiO<sub>2</sub>**

(a) Contrast ( $1-R$ ) of graphene and  $h$ -BN on Si/SiO<sub>2</sub> (285 nm) for energies of up to 6.1 eV, calculated using  $\sigma$  from Figure 3.7. (inset) Schematic for imaging samples on Si/SiO<sub>2</sub> substrates in reflection mode. (b) (left) Image of a graphene/ $h$ -BN junction on Si/SiO<sub>2</sub> (285 nm), illustrating that  $h$ -BN is clearly visible at 6.1 eV, and (right) a false color image combining data at 6.1 and 5.0 eV, showing the relative positions of graphene and  $h$ -BN in this device (scale bar 5  $\mu$ m).

Our DUV-Vis-NIR hyperspectral microscope can also image and characterize atomically thin heterostructures on non-transparent substrates for device fabrication, most notably silicon with an oxide layer, when operating in reflection mode (Figure 3.9a, inset). For monochromatic imaging, the oxide thickness determines the contrast once  $\sigma(\lambda)$  of the atomically thin film is known [21]. Based on our measured  $\sigma$  (Figure 3.7), we calculate ( $1-R$ ) vs. energy for graphene and  $h$ -BN on 285 nm thick oxide, a substrate which is already widely used for graphene imaging, in Figure 3.9. Our calculation predicts high contrast for graphene near 2.2, 3.6, and 4.8 eV, while  $h$ -BN exhibits high contrast only near 6.1 eV. This allows rapid imaging of both graphene and  $h$ -BN directly on 285 nm Si/SiO<sub>2</sub>, as demonstrated in Figure 3.9b. We note that  $h$ -BN should be visible at 6.1 eV for most oxide thicknesses, including on bare silicon, except for a few specific cases (near  $(54 + 66\alpha)$  nm, where  $\alpha$  is an integer).

### 3.7 | Conclusion

In conclusion, our DUV-Vis-NIR hyperspectral microscope provides a versatile platform for imaging and characterization of arbitrary 2D heterostructures. While we focused on graphene/*h*-BN junctions in this chapter, the optical and TEM characterization methods demonstrated here can be immediately applied for the study of heterostructures formed between other 2D materials. In particular, we will discuss the possible applications of this microscope to study MoS<sub>2</sub> and other TMD heterostructures in more detail in Chapter 7. Recent theoretical work has predicted exciting optical and electronic properties in many such systems which have yet to be characterized [26-28], and our technique provides an essential tool for developing complex 2D devices with highly controlled, tunable functionalities.

Additionally, in multilayer stacks of 2D materials, interlayer interactions can generate additional structure-dependent optical features [29-35]. An important example is twisted bilayer graphene, which exhibits multiple additional absorption peaks at DUV and visible energies, depending on its twist angle ( $\theta$ ) [32-35]. Our microscope has been essential for quantitative characterization of the optical properties of tBLG as a function of  $\theta$ , establishing precise structure-property relationships in this material. More details of this application of our microscope will be described in Chapters 5 and 6.

## References

- [1] R. W. Havener, C. J. Kim, L. Brown, J. W. Kevek, J. D. Sleppy, P. L. McEuen, and J. Park, *Nano Letters* **13**, 3942 (2013).
- [2] R. Havener, A. Tsen, H. Choi, and J. Park, *NPG Asia Materials* **3**, 91 (2011).
- [3] P. Y. Yu and M. Cardona, *Fundamentals of semiconductors: physics and materials properties* (Springer, 1996).
- [4] J. D. Jackson, *Classical Electrodynamics* (John Wiley & Sons, Hoboken, NJ, 1999).
- [5] K. F. Mak, M. Y. Sfeir, Y. Wu, C. H. Lui, J. A. Misewich, and T. F. Heinz, *Physical Review Letters* **101**, 196405 (2008).
- [6] R. Nair, P. Blake, A. Grigorenko, K. Novoselov, T. Booth, T. Stauber, N. Peres, and A. Geim, *Science* **320**, 1308 (2008).
- [7] K. Kim *et al.*, *Nano Letters* **12**, 161 (2012).
- [8] R. Gorbachev *et al.*, *Small* **7**, 465 (2011).
- [9] K. Mak, J. Shan, and T. Heinz, *Physical Review Letters* **106**, 046401 (2011).
- [10] D. Chae, T. Utikal, S. Weisenburger, H. Giessen, K. von Klitzing, M. Lippitz, and J. Smet, *Nano Letters* **11**, 1379 (2011).
- [11] Craic Technologies Microspectrophotometer & Microspectrometer. Web. 21 Jun 2014. <<http://www.microspectra.com/>>
- [12] R. Barker, *Philosophical Transactions* **39**, 259 (1735).
- [13] Schematic of reflective objective. Illustration. n.d. Adjustable ReflX Objective 52X/0.65NA DUV, Finite. *Edmund Optics*. Web. 21 Jun 2014.
- [14] G. Nadorff and F. DeWitt. Reflexicon objectives for imaging, <[https://cvimellesgriot.com/products/Documents/TechnicalGuide/CVIMGRefluxicon\\_Whitepaper.pdf](https://cvimellesgriot.com/products/Documents/TechnicalGuide/CVIMGRefluxicon_Whitepaper.pdf)> (2012).
- [15] M. Levendorf, C. Kim, L. Brown, P. Huang, R. Havener, D. Muller, and J. Park, *Nature* **488**, 627 (2012).
- [16] L. Brown, R. Hovden, P. Huang, M. Wojick, D. A. Muller, and J. Park, *Nano Letters* **12**, 1609 (2012).
- [17] P. Huang *et al.*, *Nature* **469**, 389 (2011).
- [18] F. Nelson, V. Kamineni, T. Zhang, E. Comfort, J. Lee, and A. Diebold, *Applied Physics Letters* **97**, 253110 (2010).

- [19] J. Overbeek, *Journal of Physical Chemistry* **64**, 1178 (1960).
- [20] S. Roddaro, P. Pingue, V. Piazza, V. Pellegrini, and F. Beltram, *Nano Letters* **7**, 2707 (2007).
- [21] P. Blake, E. Hill, A. Neto, K. Novoselov, D. Jiang, R. Yang, T. Booth, and A. Geim, *Applied Physics Letters* **91**, 063124 (2007).
- [22] Y. Shi *et al.*, *Nano Letters* **10**, 4134 (2010).
- [23] M. Bruna and S. Borini, *Journal of Physics D-Applied Physics* **42**, 175307 (2009).
- [24] M. Ispirian, S. Karabekyan, and R. Eckmann. Cyro Industries Inc. data tabulated by luxpop.com, <[http://www-hera-b.desy.de/subgroup/detector/rich/rich/lens\\_system](http://www-hera-b.desy.de/subgroup/detector/rich/rich/lens_system) Filename: plastic\_trans.ps> (2012).
- [25] E. Franke, M. Schubert, J. Hecht, H. Neumann, T. Tiwald, D. Thompson, H. Yao, J. Woollam, and J. Hahn, *Journal of Applied Physics* **84**, 526 (1998).
- [26] J. Yan, K. W. Jacobsen, and K. S. Thygesen, *Physical Review B* **86**, 039910 (2012).
- [27] K. Kośmider and J. Fernández-Rossier, *Physical Review B* **87**, 075451 (2012).
- [28] H. Park, A. Wadehra, J. Wilkins, and A. Neto, *Applied Physics Letters* **100**, 253115 (2012).
- [29] K. Mak, C. Lee, J. Hone, J. Shan, and T. Heinz, *Physical Review Letters* **105**, 136805 (2010).
- [30] K. F. Mak, C. H. Lui, J. Shan, and T. F. Heinz, *Physical Review Letters* **102**, 4 (2009).
- [31] Y. Zhang, T. Tang, C. Girit, Z. Hao, M. Martin, A. Zettl, M. Crommie, Y. Shen, and F. Wang, *Nature* **459**, 820 (2009).
- [32] J. T. Robinson, S. W. Schmucker, C. B. Diaconescu, J. P. Long, J. C. Culbertson, T. Ohta, A. L. Friedman, and T. E. Beechem, *ACS Nano* **7**, 637 (2012).
- [33] R. Havener, H. Zhuang, L. Brown, R. Hennig, and J. Park, *Nano Letters* **12**, 3162 (2012).
- [34] Y. Wang, Z. Ni, L. Liu, Y. Liu, C. Cong, T. Yu, X. Wang, D. Shen, and Z. Shen, *ACS Nano* **4**, 4074 (2010).
- [35] P. Moon and M. Koshino, *Physical Review B* **87**, 205404 (2013).

## Chapter 4 : WIDEFIELD RAMAN IMAGING

### 4.1 | Introduction

Raman spectroscopy has been used extensively to study graphene and other  $sp^2$ -bonded carbon materials, and can provide quantitative information about a variety of parameters including defect density, strain, doping, layer number, and stacking order in graphene samples. However, the imaging capabilities of standard Raman spectroscopy techniques are limited by their low throughput. In this chapter, we apply an existing alternative imaging mode, widefield Raman imaging, to rapidly visualize and characterize graphene films on arbitrary substrates. We show that this technique can be used to image graphene orders of magnitude faster than conventional micro-Raman imaging allows, while still obtaining detailed spectral information about the sample.

Then, we showcase the advantages of widefield Raman imaging in several important applications, which establish this tool as a powerful and versatile characterization method for graphene at different stages of growth and device fabrication. First, we show that unlike white light optical microscopy, widefield Raman imaging can be used to rapidly and clearly visualize graphene on a variety of substrates, including unoxidized silicon and copper, as well as suspended graphene. Second, we demonstrate that widefield Raman is a valuable tool to characterize the quality of CVD graphene, revealing spatial inhomogeneities in film quality that could easily go undetected with point Raman spectroscopy. Finally, we use our microscope to monitor dynamic processes in graphene with high spatial and spectral resolution over a large area in real time. These novel implementations of widefield Raman for graphene imaging provide valuable information that cannot be easily obtained with other optical imaging methods, and

enable new experiments at various stages of graphene growth and processing. The majority of this chapter is reproduced from [1].

## 4.2 | Raman spectroscopy

Raman scattering (technically, Stokes Raman scattering) is an inelastic process which occurs when an absorbed photon loses a small portion of its energy to a vibrational mode (phonon) in a material, and a corresponding redshifted photon is reemitted. The redshift of the emitted light is typically quantified in units of wavenumber ( $\text{cm}^{-1}$ ), which is proportional to energy ( $1 \text{ eV} \approx 8000 \text{ cm}^{-1}$ ). Only a few specific phonon modes are Raman allowed, and the corresponding Raman spectrum contains several peaks. Because Raman scattering involves interactions between both electronic and vibrational excitations, the Raman spectrum of 2D materials can be sensitive to a large number of parameters, including strain, doping, defect density, number of layers, and stacking order. The overall intensity of the Raman scattering also depends on the amount of light the material absorbs at both the excitation ( $\lambda_{\text{ex}}$ ) and emission wavelengths.

Because the probability of a Raman process occurring is very low (for example,  $\sim 1/10^{10}$  absorbed photons undergo Raman scattering for the case of carbon nanotubes [2]), the intensity of the light incident on the sample needs to be high in order for Raman scattering to be detectable. In addition, the incident light needs to be monochromatic for the Raman peaks to be resolved. For these reasons, Raman spectroscopy of 2D materials is typically performed using a focused laser source with intensity of up to  $1 \text{ mW}/\mu\text{m}^2$  [3], but alternative modes of Raman imaging will be discussed in Section 4.3.

Although Raman spectroscopy has been applied to a variety of 2D materials, graphitic carbon materials have been a focus of Raman studies for many decades. The Raman spectrum of

graphene is shown in Figure 4.1. Two peaks, the G peak and the 2D (also referred to as G') peak, are the most prominent in graphene. An additional two peaks, the D and D' peaks, are forbidden by momentum conservation in pristine graphene but are activated by the presence of defects [4]. A D peak can indicate any of a variety of defects in graphene, including grain boundaries [5], wrinkles [6,7], point defects [8], and/or cracks and edges [9].

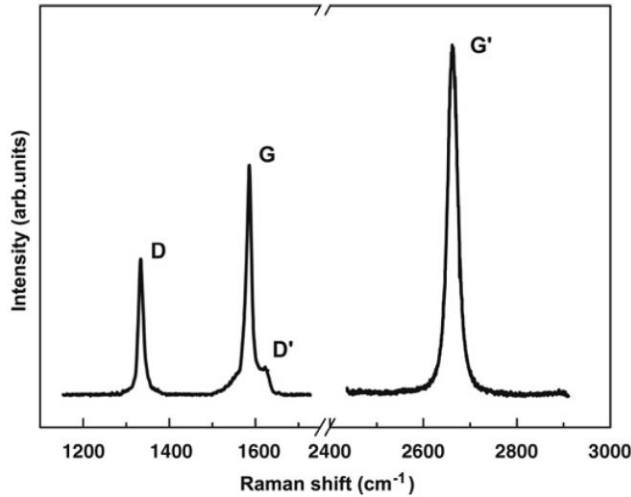


**Figure 4.1: Raman spectrum of graphene**

An example Raman spectrum of graphene illustrating the four most prominent peaks. The G and G' peaks are found in pristine graphene, while the D and D' peaks are activated by defects. The G' peak is also referred to as the 2D peak. [10]

The G peak is generated by a first order Raman process where energy is lost to a single, zero momentum optical phonon. On the other hand, the 2D peak (as well as the D and D' peaks) involves phonons with finite momentum, and so the states involved in the 2D process span across multiple locations in momentum space. While the phonon mode involved in the G process is always the same regardless of the graphene band structure or  $\lambda_{ex}$ , the mode(s) of the 2D peak are sensitive to both of these parameters. For example, the 2D peak of Bernal stacked bilayer

graphene splits into four components due to the hybridization of the electronic bands in this material (Figure 4.2) [10,11].

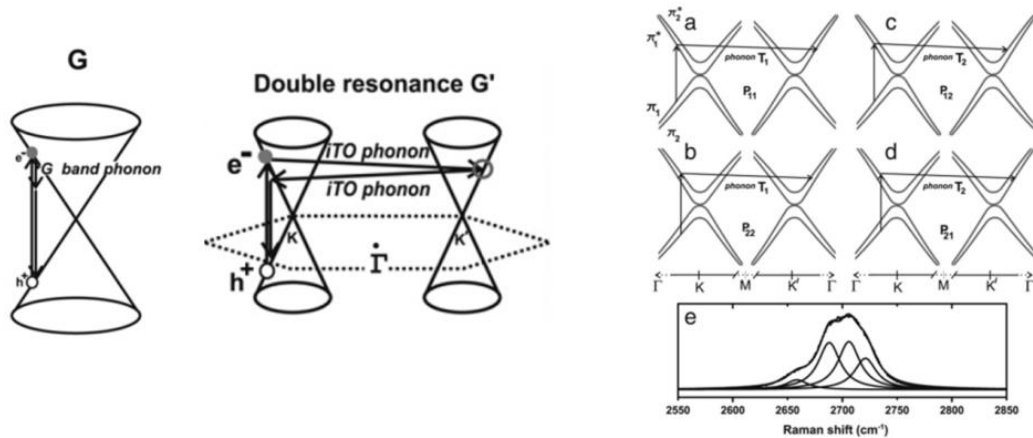


**Figure 4.2: Raman processes in graphene**

(left) Schematics of the G and G' (or 2D) Raman processes in graphene. [10] (right) Schematic of the 2D Raman process in oriented bilayer graphene, illustrating how the hybridized band structure leads to four components of the 2D peak. [10]

In general, when the graphene layers are known to be oriented (as in exfoliated samples), the shape of the 2D peak and intensity ratio between the 2D and G peaks are very reliable indicators of the number of layers [10-13] and stacking order [14]. On the other hand, for twisted multilayers of graphene, both the G and 2D peaks can exhibit more complex behavior as a function of  $\theta$  and  $\lambda_{\text{ex}}$  [15-17], which will be discussed in more detail in Chapter 6.

The positions of the G and 2D peaks are sensitive to both strain and doping, as changes to each of these parameters are capable of softening or stiffening the graphene phonon dispersion [18,19]. However, while controlled experiments have measured the dependence of the peak positions on both doping and strain individually, it is difficult to determine the degree of doping and strain simultaneously from a single Raman spectrum [20]. For uniaxial strain, G peak splits;

the degree of peak splitting and the polarization dependence of each peak can then be used to identify the graphene crystal orientation [18].

Unlike absorption spectroscopy (as described in Chapter 3), Raman spectroscopy is currently less relevant for 2D materials beyond graphene. Hexagonal boron nitride has a similar atomic structure to graphene, and a mode analogous to the G mode in graphene is Raman allowed in *h*-BN [21]. The wavenumber of this peak is  $\sim 300\text{ cm}^{-1}$  lower than the graphene case due to the differences in the C-C and B-N bond effective spring constants. However, this Raman peak is typically weaker in *h*-BN due to the low absorption of this material at visible energies. TMDs exhibit two Raman peaks near  $400\text{ cm}^{-1}$  (typically denoted as the  $E_{2g}^1$  and  $A_{1g}$  modes), and the separation between these peaks appears to be a reliable indicator of layer number for the case of exfoliated  $\text{MoS}_2$  samples [22]. Overall, the Raman response of both *h*-BN and TMDs is not thoroughly characterized compared to that of graphene.

### 4.3 | Widefield and confocal microscopy

As discussed above, the Raman spectrum of a sample is typically acquired at a single point with a focused laser spot, a geometry known as confocal and/or micro-Raman spectroscopy. However, spatial mapping of a sample with confocal micro-Raman is limited due to the technique's low throughput. To create an image, the laser spot is raster-scanned across the sample to generate a two-dimensional map of a specific Raman band (see Figure 4.3a for a schematic). The image acquisition speed is limited by the low efficiency of Raman scattering and the laser power (restricted by the damage threshold, below 2 mW for confocal illumination of graphene [3]). As a result, a diffraction-limited image of an area of tens of microns across

typically requires hours to acquire, making micro-Raman ill-suited for rapid, large-scale graphene imaging.

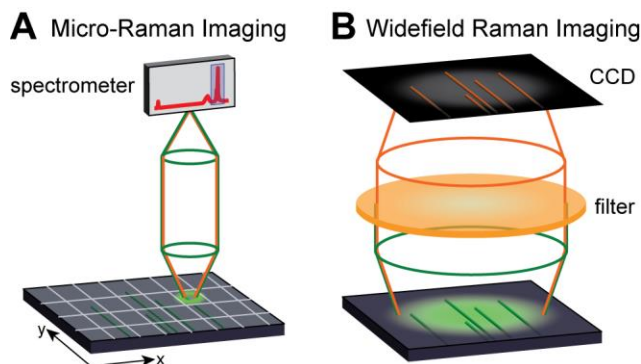


**Figure 4.3: Confocal vs. widefield Raman imaging**

Comparison of two-dimensional scanning confocal Raman (a) with widefield Raman imaging (b). Schematics illustrate serial collection of spectra over a series of pixels with a confocal micro-Raman setup (a) vs. large area imaging of a specific band with the widefield Raman imaging setup (b).

Another alternative is to employ widefield Raman imaging (also known as global or direct Raman imaging) [23-28], which is illustrated in Figure 4.3b. In this imaging mode, a planar sample is illuminated with a large collimated (or defocused) laser spot, and the Raman-scattered light from the entire illuminated area is imaged with an objective lens and a CCD camera after filters select for a specific Raman band. The laser power used to illuminate the sample can be orders of magnitude stronger than that used in micro-Raman imaging, but the power is distributed over a much larger area, preventing damage to the sample. This allows for rapid acquisition of large-area, diffraction-limited images. Additionally, imaging spectroscopy can be used in a line mapping geometry to obtain high spectral resolution Raman spectra once an area of interest is identified (see Figure 4.7) [26,29]. Widefield Raman imaging has been successfully employed for a variety of applications in chemistry, biology, and materials science [23-26].

Applying this existing technique to image graphene and other  $sp^2$ -bonded carbon materials on planar substrates is straightforward. Widefield Raman images can be acquired at wavelengths corresponding to the known Raman bands of these materials (G, D, 2D) by using the appropriate optical bandpass filters [23-26]. However, despite the fact that Raman spectroscopy is used to characterize  $sp^2$ -bonded carbon materials so frequently, widefield Raman imaging was only recently applied to carbon nanotube imaging [27,28], and the time-consuming micro-Raman technique is still the standard tool for Raman imaging of graphene. Next, we demonstrate that widefield Raman imaging indeed enables rapid, large-scale, and non-destructive characterization of graphene, while providing spectral information comparable to that obtainable with confocal Raman.

#### **4.4 | Widefield Raman microscope design**

Our widefield Raman setup was built using an inverted microscope body as a platform. A high power, diode-pumped solid state (DPSS) laser is used as an illumination source. The laser beam passes through a cleanup bandpass filter and is linearly polarized, after which the beam diameter can be adjusted with a beam expander. Next, the main modification of our widefield Raman microscope from a typical confocal geometry, which allowed us to obtain a large collimated illumination beam at the sample surface (40-300  $\mu\text{m}$  in diameter), was to focus the laser at the back focal plane of an objective lens by using a convex lens (Figure 4.4). While the power delivered to the sample is orders of magnitude greater than that used by confocal Raman techniques (up to hundreds of mW for widefield Raman on graphene *vs.*  $\sim 0.1$  mW for confocal Raman on graphene), the power per unit area remains low ( $\sim 0.1$  mW/ $\mu\text{m}^2$  for both techniques).

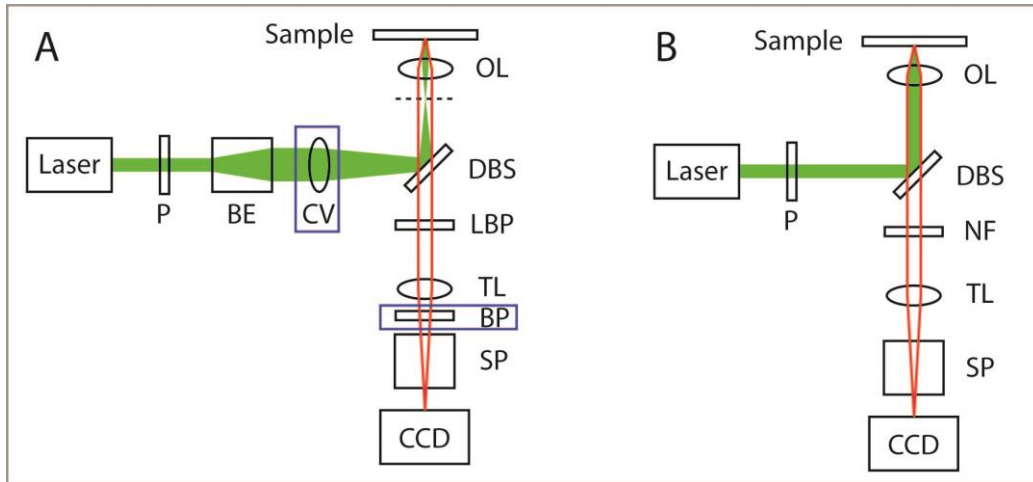


**Figure 4.4: Schematic of widefield Raman setup**

Schematics of widefield Raman setup (a) compared with a typical micro-Raman setup (b). Green and red lines indicate beam profiles of excitation and scattered light, respectively. BP can be either tunable bandpass filter or single bandpass filter. Abbreviations: P: Polarizer, BE: beam expander, CV: convex lens, DBS: dichroic beam splitter, OL: objective lens, LBP: long pass filter, BP: bandpass filter, CCD: charge-coupled device, NF: notch filter, TL: tube lens, SP: spectrometer. Blue boxes indicate major difference in the configurations of (a) and (b).

The same objective is used for illumination and detection. After scattering from the sample, the detected light passes through a dichroic beam splitter and long pass filter to eliminate the elastically scattered light. Finally, a bandpass filter is used to select a specific Raman band, or an imaging spectrometer is used to obtain a full Raman spectrum (see Section 4.5). Images are recorded using a CCD camera.

In Figure 4.5, we demonstrate the high-throughput, diffraction-limited Raman imaging capability of our microscope for graphene and single-walled carbon nanotubes, another type of  $sp^2$ -bonded carbon material. First, to demonstrate the difference in imaging capabilities between widefield and micro-Raman imaging, Figure 4.5 shows G band images of aligned single-walled carbon nanotubes on a quartz substrate obtained using micro-Raman and widefield Raman imaging, respectively (carbon nanotubes exhibit a Raman G peak similar to that of graphene). The widefield Raman image was obtained in 5 seconds (3 W total laser power with a 80  $\mu\text{m}$  spot

size), while the confocal Raman image took 3 hours (0.5  $\mu\text{m}$  pixel size and 1 sec/pixel). Despite its much shorter acquisition time ( $\sim 1/2000$ ), the widefield Raman image has a better signal-to-noise ratio and improved spatial resolution. We also stress that the inherent resolution of widefield Raman imaging is diffraction-limited, whereas increasing the resolution of a micro-Raman image requires more pixels, and thus a longer imaging time.

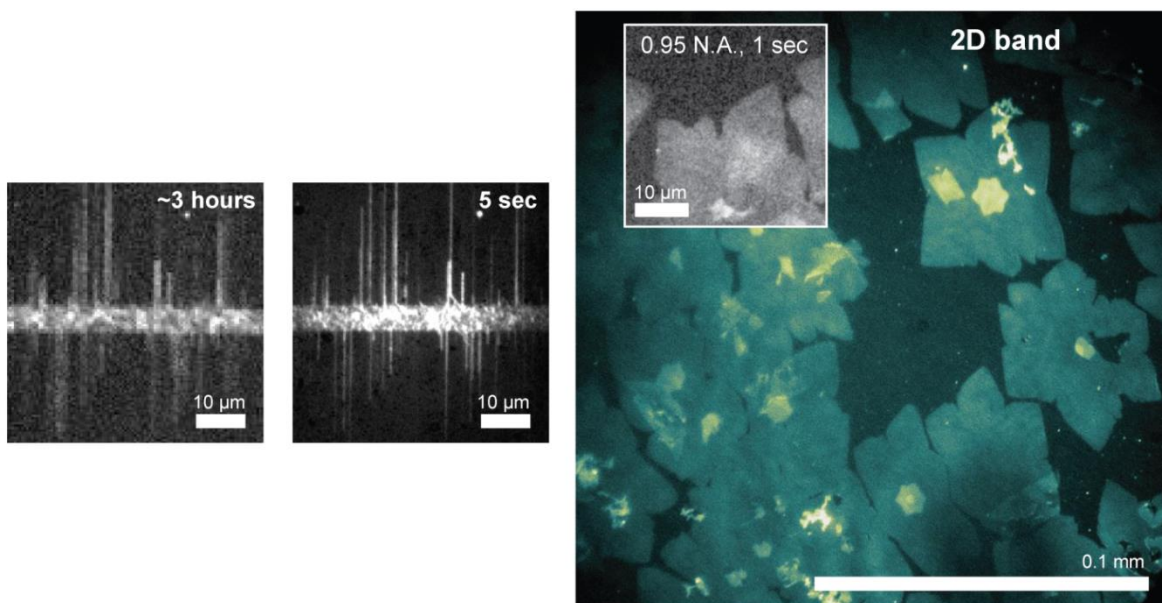


**Figure 4.5: Rapid Raman imaging of  $\text{sp}^2$ -bonded carbon materials**

(left) G band images of the same area of aligned carbon nanotubes obtained with micro-Raman setup ( $\sim 3$  hour acquisition, 0.5  $\mu\text{m}$  pixel size) and widefield Raman setup (5 sec acquisition,  $\sim 80$   $\mu\text{m}$  illumination size, 3 W), using 100x objective (N.A. = 0.95) in both cases. (right) A sub-millimeter scale false color 2D band image of graphene using 20x objective (N.A. = 0.70) with 300 sec acquisition time. (inset) With a 100x (N.A. = 0.95) objective, graphene is clearly visible on Si/285 nm  $\text{SiO}_2$  at acquisition times as short as 1 sec. Image is Gaussian blurred (radius 1 pixel = 125 nm) to reduce CCD noise.

The right panel of Figure 4.5 shows a sub-millimeter scale false color image of the 2D band of CVD graphene with intentionally incomplete surface coverage transferred onto a Si/285 nm oxide substrate. This image was obtained with a 20 $\times$ , 0.70 N.A. objective, 50 mW of laser power at 532 nm, and an acquisition time of 300 seconds. A confocal image on this scale with

identical imaging conditions as in Figure 4.5 would take 35 hours to obtain. Using an objective with a higher N.A. (0.95, 100×), we can further decrease the imaging time, allowing the graphene film to be resolved in as little as 1 second (see inset). High-quality images can be obtained on Si/285 nm oxide in 1 minute under these imaging conditions.

#### 4.5 | Spectrally resolved imaging

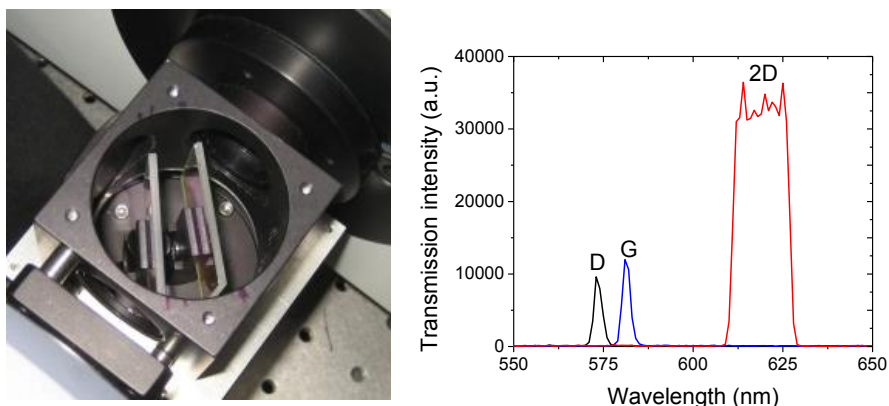


**Figure 4.6: Tunable bandpass filter**

(left) Picture of tunable bandpass filter. Note that the angles of the two bandpass filters are offset slightly. (right) Bandwidth at wavelengths corresponding to D, G, and 2D bands (for 532 nm excitation) obtained from tunable bandpass filter.

Spectral information about the sample can be obtained by selecting the known Raman bands of graphene with various bandpass filters. Depending on the substrate, commercially available 10 nm FWHM (full width at half maximum) bandpass filters usually suffice to capture G and 2D band images such as those shown in Figure 4.5, because these Raman bands are well separated in wavelength (~580 and 620 nm, respectively, for 532 nm excitation). However, the separation between the D and G bands is much smaller (~8 nm), and commercially available filters cannot distinguish between them.

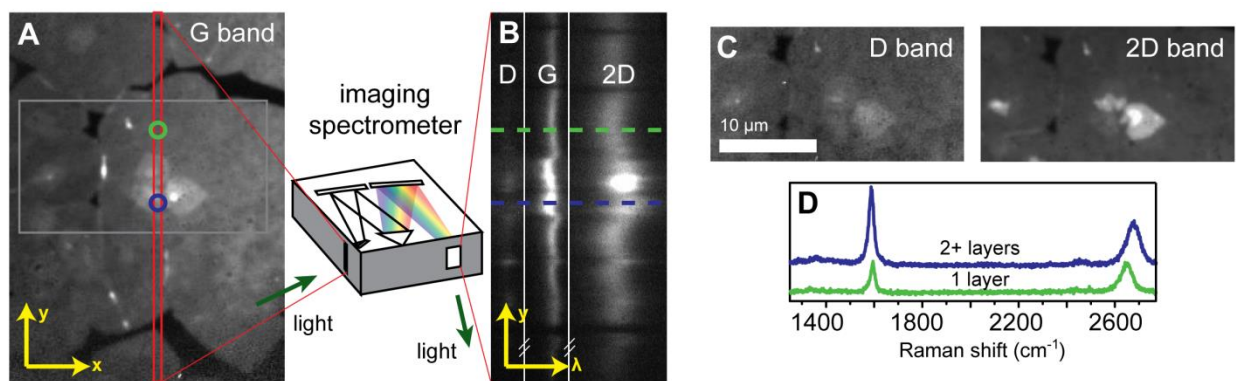


**Figure 4.7: Spectrally resolved imaging**

(a) G band image of CVD graphene that has been normalized for spatial variations in laser intensity (using the second order silicon Raman peak at  $\sim 1000\text{ cm}^{-1}$ ). Red box indicates a kinematic slit position for spectral measurement. (b) Spectral analysis along the line in (a), with D, G, and 2D Raman bands visible. Note that the abscissa changes from distance to Raman shift. Spectra were obtained in 60 seconds with spectrometer entrance slit width of  $50\text{ }\mu\text{m}$  ( $3.5\text{ cm}^{-1}$ ) and 500 mW laser power over an  $\sim 80\text{ }\mu\text{m}$  spot size. (c) Normalized D and 2D band images of area outlined in G band image, obtained with tunable bandpass filter. (d) Raman spectra for single (bottom) and multiple (top) graphene layers, obtained along dotted lines in (b).

To address this problem, we used a custom-made, continuously-variable filter with a bandwidth of  $100\text{ cm}^{-1}$  ( $\sim 3\text{ nm}$ ) for  $940\text{-}1850\text{ cm}^{-1}$ , encompassing the D and G bands. We achieved a bandwidth as small as  $2.5\text{ nm}$  by using two tunable bandpass filters (TBP01-620/14-25 $\times$ 36, Semrock). The individual filters have  $\sim 20\text{ nm}$  bandwidths, and the center wavelength (CWL) of each bandpass filter can vary from 620 to 550 nm by changing the angle between the filter and the incident light from 0 to  $60^\circ$  (the change in CWL is roughly proportional to  $\sin(\theta)$ ). By offsetting the two filters about  $10^\circ$  apart, the two bandpass filters act as one narrow tunable filter, with a roughly constant  $2.5\text{ nm}$  FWHM between 560 and 590 nm, the range where CWL vs.  $\theta$  is approximately linear (Figure 4.6). For wavelengths above 600 nm, the bandwidth increases, reaching  $\sim 20\text{ nm}$  at 620 nm (2D band @ 532 nm excitation).

Using our homebuilt filter, Figure 4.7 shows G, D, and 2D band images of the same area of a large grain CVD-grown graphene sample transferred onto a Si/285 nm oxide substrate (500

mW power with a 80  $\mu\text{m}$  spot size). The use of the tunable bandpass filter allows for rapid comparison of the relative intensities of these Raman bands over large areas. From the data shown in Figure 4.7, we can observe graphene nucleation sites and growth patterns with a high signal-to-noise ratio, and we find that our sample has a relatively low defect density over a large area.

As an alternative, for high-resolution spectral information, we can perform imaging spectroscopy [26,29]. While maintaining widefield illumination, Raman spectra along a vertical line on the sample can be obtained by positioning the entrance slit of a spectrometer at the image plane (Figure 4.7). The imaging spectrometer used in our setup contained a turret with an interchangeable 1200 g/mm, 500 nm blaze grating (spectral mode) and a mirror (imaging mode). Figure 4.7 presents Raman spectra acquired in this mode. Here, the y-axis of the CCD image after the imaging spectrometer (Figure 4.7b) corresponds to the y-axis of the real space image along a fixed line (Figure 4.7a), while the x-axis of the CCD image corresponds to the Raman shift ( $\text{cm}^{-1}$ ). Multi-layer areas can be rapidly identified from an abrupt increase in G band intensity [30] and redshift of the 2D peak [10], which can be confirmed quantitatively by extracting Raman spectra from the CCD data (Figure 4.7c). In addition, we observe small ( $\pm \sim 2 \text{ cm}^{-1}$ ) fluctuations in the G peak position, which could indicate local doping [19] or strain [18] in our sample. All of the data in Figure 4.7 were acquired in a matter of minutes, providing a means to rapidly characterize the quality of CVD graphene over a large area. In addition, collecting a series of such spectra while scanning the sample in the x-direction (“line mapping”) allows for complete sample mapping with full Raman spectra at every point [26,29]. Since data from many pixels are still acquired in parallel, this technique provides the same information that can be acquired with confocal micro-Raman imaging in a much shorter time [26].

## 4.6 | Thermal effects of laser power

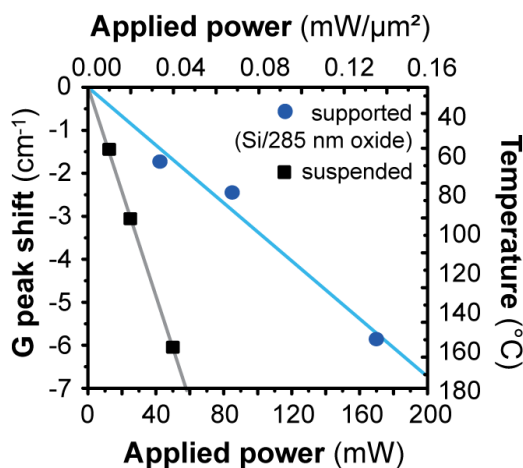


**Figure 4.8: Graphene temperature vs. laser power**

Approximate temperature increase of graphene vs. applied power for a suspended (black) and supported (blue) graphene sample. G peak shift is determined by offsetting the linear fit of G peak position vs. applied power to 0 at room temperature (25°C).

To ensure that graphene is not damaged by our technique, we monitor the local temperature increase induced by the imaging laser using imaging spectroscopy, as discussed in Section 4.5. Heating graphene in an oxidative environment (such as air) can cause strong hole doping at ~200°C and etching at 450°C [31], so to avoid damage, the sample should be kept below these temperatures. We can estimate the temperature increase of the graphene by measuring the G peak position as a function of laser power, and using a known conversion factor between G peak position and temperature [32]. Our results for supported graphene (on silicon/285 nm oxide), as well as suspended graphene (see Figure 4.9), are shown in Figure 4.8. For suspended samples, or supported samples at higher powers, the temperature increase can be significant. However, under the conditions used to image most of our samples (50 mW over a 40-50 μm spot size), the local temperature only increases by a few tens of degrees Celsius, confirming that widefield Raman imaging provides both rapid and non-destructive graphene imaging. From the previous sections,

it is clear that widefield Raman is well-suited for high-throughput graphene imaging and characterization.

#### 4.7 | Substrate-independent imaging

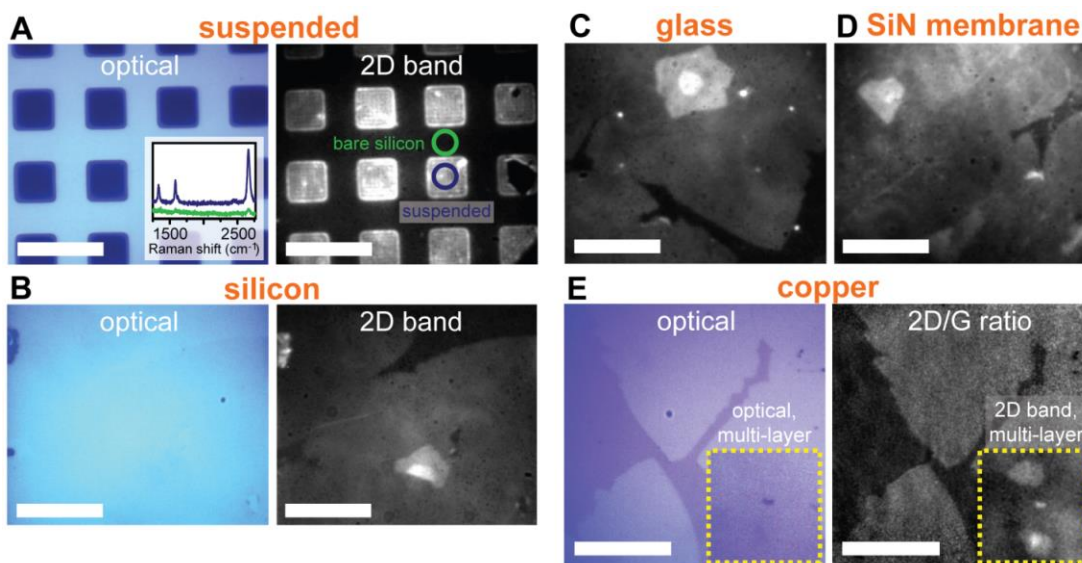


**Figure 4.9: Substrate-independent imaging**

(a) (left) Optical image of graphene suspended over 5  $\mu\text{m}$  holes etched in bare silicon. The graphene is invisible over the entire substrate. (right) 2D band image of the same area shows a high yield of suspended graphene. Acquisition time 60 seconds. (inset) Raman spectra from suspended and supported graphene. The intensity of the Raman signal of supported graphene on bare silicon is an order of magnitude smaller than the signal of suspended graphene. (b) (left) Optical image of graphene on bare silicon, which is also almost impossible to see. (right) 2D band image of same area shows graphene edges and multi-layer areas. Acquisition time 300 seconds. (c) 2D band image of graphene on fused silica, acquisition time 300 seconds. (d) 2D band image of graphene on 5 nm thick silicon nitride, acquisition time 300 seconds. (e) (left) Optical image of graphene grown on copper film. Inset shows an area with multiple graphene layers, which is indistinguishable from single-layer graphene. (right) 2D/G ratio image shows location of graphene on copper, and multiple layer regions (inset, same area as optical image) can be distinguished from single-layer ones in a 2D band image. Raw images acquired in 300 seconds with 450 nm laser. All scale bars 10  $\mu\text{m}$ , and all images obtained at 50 mW power.

Widefield Raman imaging can be used to rapidly visualize graphene on a large variety of substrates, enabling high-throughput characterization through various stages of graphene growth and device fabrication. Previous work employing widefield Raman to image carbon nanotubes focused mainly on suspended nanotubes [27,28], which typically exhibit stronger Raman

scattering than nanotubes on a substrate [27,33], and imaging of graphene is often performed on silicon with a 285 nm thick oxide layer, which enhances optical contrast through constructive interference [30,34]. However, graphene exhibits a similar Raman signature on many substrates [35], allowing substrate-independent Raman imaging. Although the intensity of the Raman signal is reduced on the substrates we studied as compared to silicon/285 nm oxide, good quality raw images on all of these substrates can be acquired in five minutes or fewer.

First, as with carbon nanotubes [27,28], widefield Raman can be used to image suspended regions of graphene. Figure 4.9a shows an optical image (left) of a bare silicon substrate with 5  $\mu\text{m}$  square holes etched through it. CVD graphene was transferred on top of the substrate, but it is impossible to resolve under a white light reflection microscope. On the other hand, a 2D band widefield Raman image (right) quickly reveals that most of the holes are covered in graphene. Suspended graphene can be visualized with an acquisition time of seconds (see Figure 4.13), while high quality images like Figure 4.9a can be obtained in 1-2 minutes.

The Raman signal is approximately an order of magnitude stronger over the suspended regions than it is on bare silicon (see Figure 4.9a, inset). Even on bare silicon, however, graphene can be resolved with widefield Raman imaging using a sufficiently long collection time (300 seconds). Widefield Raman can easily resolve the edges and multi-layer regions of graphene on silicon, as shown in Figure 4.9b, even though the graphene is very difficult to distinguish in an optical image. It can also image graphene on transparent substrates, such as glass (Figure 4.9c), and on 5 nm thin silicon nitride membranes (Figure 4.9d), allowing subsequent DF-TEM studies [36].

Lastly, widefield Raman imaging can be used to visualize CVD graphene directly on its copper growth substrate, which allows confirmation of graphene growth without transfer. Under

white light illumination (Figure 4.9e, left), graphene shows a slight contrast difference from the copper substrate. Likely, the bare copper is slightly oxidized, while the graphene-covered areas are protected from oxidation [37]. Multi-layer regions of graphene (inset) are indistinguishable from single-layer ones.

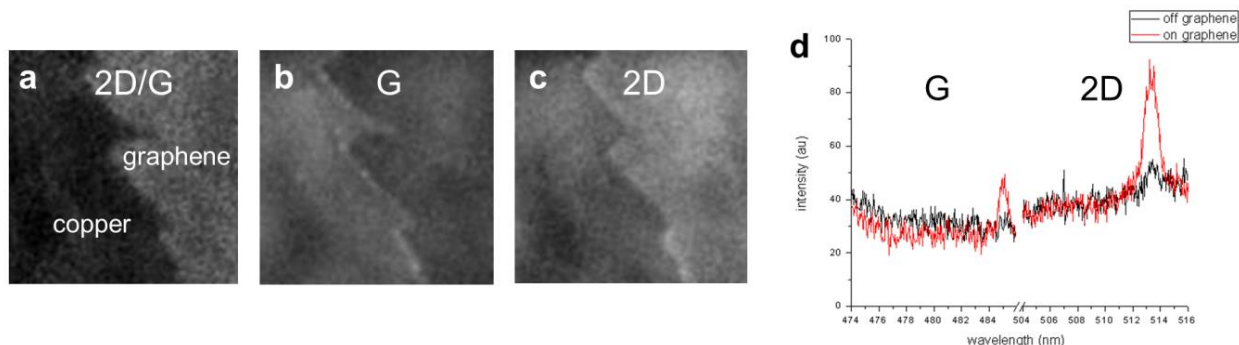


**Figure 4.10: G and 2D band widefield Raman imaging of graphene on copper**

(a) 2D/G ratio image of graphene on copper (from Figure 4.9). Graphene appears brighter than copper substrate. (b) Raw G band image of graphene on copper, showing contrast flip. (c) Raw 2D band image of graphene on copper. As in (a), the graphene appears brighter than the substrate. (b) and (c) were each acquired in 5 minutes. (d) Raman spectra on and off graphene on copper over the wavelength range of the G (left) and 2D (right) bandpass filters, after subtracting dark background. The integrated Raman signal (copper background + G band) over the range of the G bandpass filter (~475-485 nm) is slightly higher off the graphene, accounting for the contrast flip in the G band image.

Copper exhibits a relatively strong luminescence background with respect to the graphene Raman signal [8,38], but it is low enough for an excitation wavelength of 450 nm that widefield Raman imaging of graphene on copper is still possible. However, we find that for the G band image, the contrast flips, and single-layer graphene appears darker than the bare substrate (Figure 4.10). Collecting Raman spectra at adjacent locations on and off the graphene (laser intensity roughly constant) shows that near the G peak, the background is slightly higher off the graphene than on the graphene, accounting for the contrast flip when integrated over the range of our bandpass filter (~10 nm FWHM, Thorlabs).

On the other hand, a 2D/G ratio image clearly distinguishes graphene from bare copper (Figure 4.9e, right), and multi-layer regions can be identified in a 2D band image (inset). It also has the additional benefit of being automatically normalized with respect to laser intensity. Thus, widefield Raman can be used to locate and characterize graphene after all stages of device fabrication – growth, transfer to a target substrate, and patterning – and provides extra flexibility.

#### 4.8 | Defect mapping

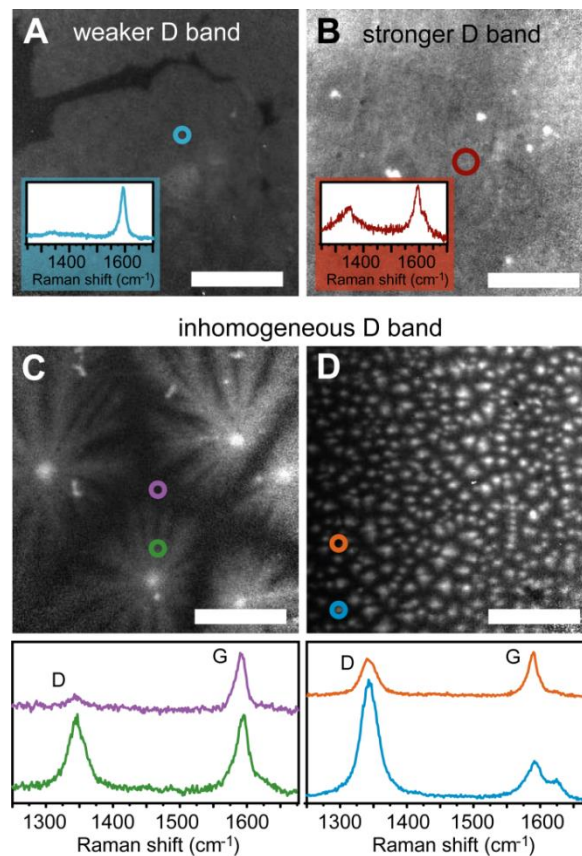


**Figure 4.11: D band imaging of CVD graphene**

Normalized D band images of various graphene samples transferred to Si/285 nm oxide. Samples exhibit a large variety of behaviors with respect to D band intensity. Some samples (a) exhibit very low, uniform D band intensity, while others (b) exhibit higher, uniform intensity. Insets show point Raman spectra, which are representative of the sample as a whole. Other samples, however, have large spatial variations in D band intensity. (c) and (d) are two examples of such behavior. Point Raman spectra taken at different locations on the sample (shown below c, d) can appear very different.

As a second application of widefield Raman imaging, we demonstrate that D band imaging can be used to rapidly compare the quality of large areas of CVD graphene produced with different growth conditions. The intensity of the Raman D peak ( $\sim 1350\text{ cm}^{-1}$ ) scales with the density of defects in a graphene film [4], and a low D peak (or low D/G intensity ratio) indicates a reasonably high quality film. Often, point Raman spectroscopy or confocal mapping over a relatively small area is used to characterize the D peak of CVD graphene, but with widefield Raman, we can rapidly image the D band intensity directly on a large scale. After transferring graphene to Si/285 nm oxide, we find that for some samples (Figure 4.11a and b), the D band intensity is roughly constant over tens of microns, and can be well-described with point Raman spectra (see insets). However, other samples (Figure 4.11c and d) show large spatial inhomogeneities in D band intensity. Raman spectra taken at various points on the sample can have vastly different D/G intensity ratios, as shown in Figure 4.11c and d. While the mechanism for these inhomogeneities is currently unknown, it is clear that point Raman spectroscopy is not sufficient to fully characterize the quality of a CVD graphene film, and that widefield Raman imaging provides valuable information about the spatial distribution of defects in our samples.

The defects in Figure 4.11 are likely point defects, but as discussed in Chapter 1, line defects including grain boundaries, wrinkles, and cracks are also common in CVD-grown samples. In previous Raman imaging studies, linear regions with increased D band intensity have been observed at the boundaries between graphene islands produced with CVD [5,6], indicating that it may be possible to image the grain structure of a CVD-grown graphene sample with optical imaging alone. However, there is little direct evidence that these lines truly correspond to grain boundaries (GBs), and not very small wrinkles, cracks, or other line defects.

In Figure 4.12, we present preliminary data comparing a DF-TEM image of the grain structure of a CVD-grown graphene sample to a D band image of the same sample, which has been transferred to a silicon nitride membrane substrate as in Figure 4.9. This particular growth is similar to Growth A in Figure 4.11 in that the grain size is large, and the D band intensity of the majority of the sample is very low. The D band image of this sample was obtained with the “line mapping” imaging mode described in Section 4.5 in order to obtain quantitative Raman spectra at each point. As shown in the DF-TEM image, this sample contains multiple GBs (indicated by the borders between regions of different colors) as well as a number of wrinkles (indicated by the white lines).

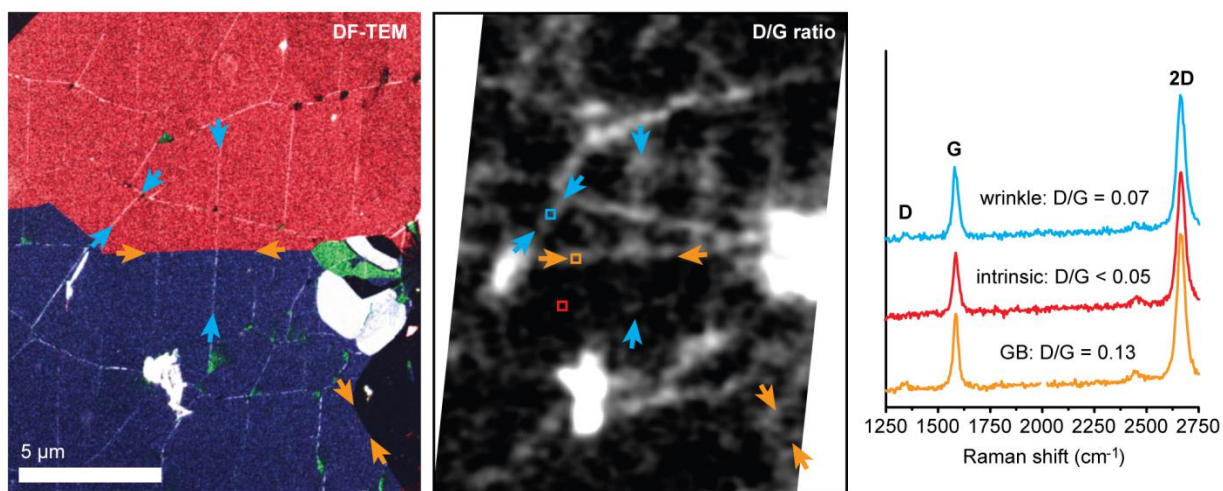


**Figure 4.12: Raman and DF-TEM grain boundary imaging**

(left) A DF-TEM image of a graphene sample. Grain boundaries are located where regions of different colors intersect, and wrinkles are indicated as small white lines. A few GBs (orange) and wrinkles (blue) have been marked by arrows. (center) A D band image of the same region, overlaid with the marked features from the DF-TEM image. (right) Raman spectra obtained at each of the boxed points in the center image.

We find that some wrinkles and some GBs observed in the DF-TEM image both correlate with a small D peak in the Raman image of the same region, providing direct evidence of a link

between the presence of GBs and increased D band intensity for the first time. The magnitude of the D peak is similar for both GBs and small wrinkles, about 1/10 of the integrated intensity of the G peak. However, we also observe that a few wrinkles and GBs do not correlate with a significant increase in D band intensity, including the bottom half of the wrinkle indicated by blue arrows in the center of the Raman image, and the grain boundary indicated by orange arrows in the bottom right hand corner of the image. While further studies will be required to study the effects of factors such as laser polarization, graphene crystalline orientation, and wrinkle width on D band intensity, our preliminary work indicates that interpreting the Raman data from a CVD-grown sample which contains both wrinkles and grain boundaries is potentially complex.

#### 4.9 | Dynamic imaging and spectroscopy

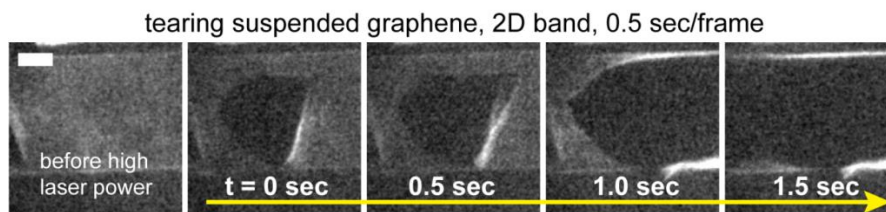


**Figure 4.13: Time-resolved Raman imaging**

Dynamic imaging of laser-induced tearing of suspended graphene. Images show 2D band of a strip of graphene (bright) suspended between two pieces of silicon (dark). When laser power is increased, a hole forms in the graphene, which eventually causes the graphene strip to mechanically fail. This tearing is observed with 0.5 second resolution. Images are Gaussian blurred (radius 1 pixel = 125 nm) to reduce CCD noise. Scale bar 5  $\mu\text{m}$ .

Finally, widefield Raman can capture images within fractions of a second, allowing large-scale, real-time spatially and spectrally resolved imaging of dynamic processes specific to graphene. We demonstrate the dynamic capability of our microscope by using the imaging laser at a high power to damage the graphene, and observing the process in real time. When graphene is

suspended (see Figure 4.9), 50 mW of laser power can cause the graphene to tear. By taking 2D band images rapidly (0.5 second frame rate), we can observe the dynamics of this process. Figure 4.13 shows a 2D band image of a suspended graphene film. After the laser power is increased, a hole is formed in the film and grows quickly, causing the entire film to fail within a few seconds. From Figure 4.8, we note that the temperature of the graphene remains below the damage threshold of 200°C, even at 50 mW laser power. However, the mechanical failures we observe appear to propagate from point defects and edges, which could be particularly unstable at higher temperatures. In addition, optical forces have been shown previously to manipulate carbon nanotubes [27], and may also be manipulating our suspended graphene. Our rapid time resolution allows us to see precisely where failures form in our suspended graphene sheets and how they propagate, enabling future studies of this and other interesting dynamic mechanical processes in graphene under a uniform external stress or local AFM indentation.

In addition, imaging spectroscopy can be used to obtain dynamic spectral information for many points on the sample surface simultaneously. When graphene is supported on a substrate, it cannot fail mechanically, but high laser power can cause the graphene to degrade. Laser-induced degradation has been observed previously for a weak laser power (2 mW) over a long time scale (~1 day) [3], but on a silicon/285 nm SiO<sub>2</sub> substrate, a 3W laser over an 80 μm spot size (~0.5 mW/μm<sup>2</sup>) degrades graphene within minutes. G band images of a sample before and after intense laser irradiation (Figure 4.14, left) show that the G band intensity decreases significantly over most of the sample after damage. The method in Figure 4.8 cannot be used to measure the temperature at higher laser powers directly, because hole doping above 200°C can cause the G peak to redshift [31], but it is reasonable to assume that the temperature of our samples increases locally by hundreds of degrees Celsius at this laser power, causing the graphene to oxidize. To

confirm that oxidation is the primary damage mechanism, a DF-TEM image [36] of a similar graphene sample on a thin silicon nitride membrane (Figure 4.14, inset) with extensive laser damage shows circular pits in multi-layer regions, which is indicative of oxidative damage [31].

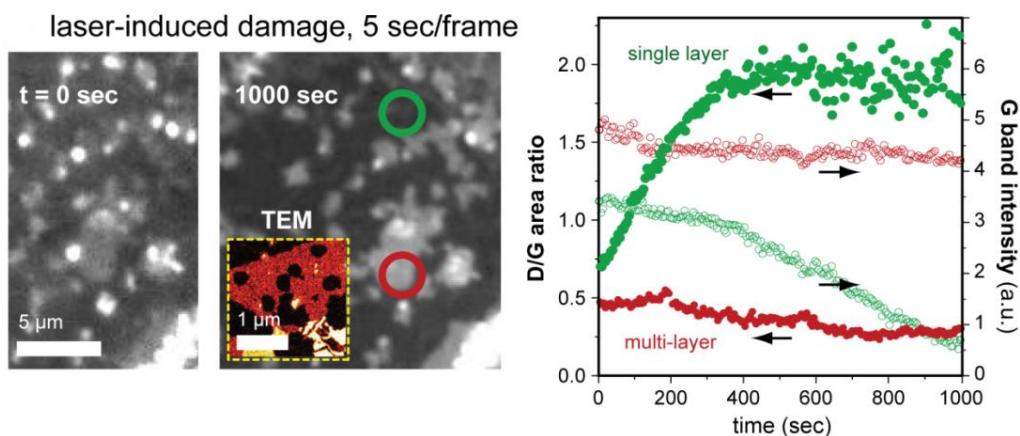


**Figure 4.14: Dynamic spectroscopy**

Dynamic spectroscopy along a line of a graphene sample on Si/285 nm oxide. (left) G band images showing a sample before and after exposure to a 3W laser. A dark area appears where the laser intensity was the strongest, showing highly damaged graphene. (inset) A false color dark-field TEM image of a similar multi-layer sample that has been heavily damaged by the imaging laser, showing circular etch pits indicative of oxidation. (right) D/G area ratio and G band intensity extracted from spectra taken at locations shown by red and green circles (left). D and G (+ D') peaks fit to single Lorentzians. Single-layer graphene (green) shows behavior consistent with increasing amorphization with time, but for multi-layer graphene (red), the D/G ratio and G intensity remain relatively constant, showing that multi-layer graphene is much more resistant to laser-induced damage than single-layer graphene.

To examine this process in detail, we use imaging spectroscopy to collect Raman spectra every 5 seconds along a line of the sample shown in Figure 4.14. For most of the sample (green), the D/G area ratio increases immediately upon intense laser irradiation up to a value of ~2, after which the G band intensity begins to decrease significantly, consistent with the amorphization of single-layer graphene [4,39]. However, for multi-layer areas (red), the G band intensity stays constant with time and the D/G ratio actually decreases slightly. The decreased reactivity of multi-layer regions as compared to single-layer regions is consistent with the previous studies of

graphene oxidation [31] and chemical reactivity [40]. We stress that with widefield Raman imaging, we obtain dynamic, spectrally resolved information for many points on our sample simultaneously, which cannot be achieved with conventional confocal techniques. An exciting future application of this technique is spatially and spectrally resolved monitoring of CVD graphene growth *in situ*.

#### **4.10 | Conclusion**

In summary, widefield Raman imaging is easily-implementable, and can rapidly image and characterize graphene over different length scales while providing detailed spectral resolution. Widefield Raman imaging can be used to map the location of graphene over a large area, and distinguish single- and multi-layer regions, on arbitrary substrates within minutes. The ability to rapidly acquire Raman images with high spectral resolution is a powerful characterization tool, allowing us to see spatial variations in film quality that would go unnoticed with point Raman spectroscopy. In addition, the acquisition speed of this technique is fast enough to allow us to observe dynamic processes in graphene with high spatial and spectral resolution. Because optical microscopy can be performed in a variety of environments, this technique enables many *in situ*, time-resolved studies of graphene growth, degradation, and electrical and mechanical processes. We expect that widefield Raman imaging will prove to be an important experimental technique for graphene imaging, enabling large-scale device fabrication and graphene growth characterization.

## References

- [1] R. W. Havener, S.-Y. Ju, L. Brown, Z. Wang, M. Wojcik, C. S. Ruiz-Vargas, and J. Park, *ACS Nano* **6**, 373 (2012).
- [2] R. Havener, A. Tsen, H. Choi, and J. Park, *NPG Asia Materials* **3**, 91 (2011).
- [3] B. Krauss, T. Lohmann, D. Chae, M. Haluska, K. von Klitzing, and J. Smet, *Physical Review B* **79**, 165428 (2009).
- [4] A. Ferrari and J. Robertson, *Physical Review B* **61**, 14095 (2000).
- [5] Q. Yu *et al.*, *Nature Materials* **10**, 443 (2011).
- [6] Y. Ogawa, K. Komatsu, K. Kawahara, M. Tsuji, K. Tsukagoshi, and H. Ago, *Nanoscale* **6**, 7288 (2014).
- [7] X. Li *et al.*, *Science* **324**, 1312 (2009).
- [8] L. Zhao *et al.*, *Science* **333**, 999 (2011).
- [9] Y. You, Z. Ni, T. Yu, and Z. Shen, *Applied Physics Letters* **93**, 163112 (2008).
- [10] L. Malard, M. Pimenta, G. Dresselhaus, and M. Dresselhaus, *Physics Reports* **473**, 51 (2009).
- [11] A. Ferrari *et al.*, *Physical Review Letters* **97**, 187401 (2006).
- [12] A. Reina, X. Jia, J. Ho, D. Nezich, H. Son, V. Bulovic, M. Dresselhaus, and J. Kong, *Nano Letters* **9**, 30 (2009).
- [13] D. Graf, F. Molitor, K. Ensslin, C. Stampfer, A. Jungen, C. Hierold, and L. Wirtz, *Nano Letters* **7**, 238 (2007).
- [14] C. H. Lui, Z. Q. Li, Z. Y. Chen, P. V. Klimov, L. E. Brus, and T. F. Heinz, *Nano Letters* **11**, 164 (2011).
- [15] R. Havener, H. Zhuang, L. Brown, R. Hennig, and J. Park, *Nano Letters* **12**, 3162 (2012).
- [16] Z. Ni, L. Liu, Y. Wang, Z. Zheng, L. Li, T. Yu, and Z. Shen, *Physical Review B* **80**, 125404 (2009).
- [17] K. Kim *et al.*, *Physical Review Letters* **108**, 246103 (2012).
- [18] T. M. G. Mohiuddin *et al.*, *Physical Review B* **79**, 205433 (2009).
- [19] A. Das *et al.*, *Nature Nanotechnology* **3**, 210 (2008).
- [20] J. Lee, G. Ahn, J. Shim, Y. Lee, and S. Ryu, *Nature Communications* **3**, 1024 (2012).
- [21] R. Gorbachev *et al.*, *Small* **7**, 465 (2011).
- [22] C. Lee, H. Yan, L. Brus, T. Heinz, J. Hone, and S. Ryu, *ACS Nano* **4**, 2695 (2010).

- [23] D. Batchelder, C. Cheng, W. Muller, and B. Smith, *Makromolekulare Chemie-Macromolecular Symposia* **46**, 171 (1991).
- [24] P. Treado, I. Levin, and E. Lewis, *Applied Spectroscopy* **46**, 1211 (1992).
- [25] G. Puppels, M. Grond, and J. Greve, *Applied Spectroscopy* **47**, 1256 (1993).
- [26] S. Schlucker, M. Schaeberle, S. Huffman, and I. Levin, *Analytical Chemistry* **75**, 4312 (2003).
- [27] K. Kaminska, J. Lefebvre, D. Austing, and P. Finnie, *Physical Review B* **73**, 235410 (2006).
- [28] K. Kaminska, J. Lefebvre, D. G. Austing, and P. Finnie, *Nanotechnology* **18**, 165707 (2007).
- [29] M. Bowden, D. Gardiner, G. Rice, and D. Gerrard, *Journal of Raman Spectroscopy* **21**, 37 (1990).
- [30] Y. Wang, Z. Ni, Z. Shen, H. Wang, and Y. Wu, *Applied Physics Letters* **92**, 043121 (2008).
- [31] L. Liu, S. Ryu, M. Tomasik, E. Stolyarova, N. Jung, M. Hybertsen, M. Steigerwald, L. Brus, and G. Flynn, *Nano Letters* **8**, 1965 (2008).
- [32] W. Cai, A. Moore, Y. Zhu, X. Li, S. Chen, L. Shi, and R. Ruoff, *Nano Letters* **10**, 1645 (2010).
- [33] Y. Zhang, H. Son, J. Zhang, M. Dresselhaus, J. Kong, and Z. Liu, *Journal of Physical Chemistry C* **111**, 1983 (2007).
- [34] P. Blake, E. Hill, A. Neto, K. Novoselov, D. Jiang, R. Yang, T. Booth, and A. Geim, *Applied Physics Letters* **91**, 063124 (2007).
- [35] Y. Wang, Z. Ni, T. Yu, Z. Shen, H. Wang, Y. Wu, W. Chen, and A. Wee, *Journal of Physical Chemistry C* **112**, 10637 (2008).
- [36] P. Huang *et al.*, *Nature* **469**, 389 (2011).
- [37] S. Chen *et al.*, *ACS Nano* **5**, 1321 (2011).
- [38] G. Boyd, Z. Yu, and Y. Shen, *Physical Review B* **33**, 7923 (1986).
- [39] E. Ferreira, M. Moutinho, F. Stavale, M. Lucchese, R. Capaz, C. Achete, and A. Jorio, *Physical Review B* **82**, 125429 (2010).
- [40] R. Sharma, J. Baik, C. Perera, and M. Strano, *Nano Letters* **10**, 398 (2010).

## **Chapter 5 : BAND STRUCTURE AND OPTICAL ABSORPTION OF TWISTED BILAYER GRAPHENE**

### **5.1 | Introduction**

The microscopy tools introduced in Chapters 2, 3, and 4 constitute a suite of techniques which can be used to disentangle the complex structure-property relationships in heterogeneous 2D materials. In particular, combining dark-field TEM (DF-TEM) and various optical microscopy techniques allows a variety of comparisons between the physical structure (i.e. grain size, orientation, and stacking order) and the optical properties of 2D samples. Examples discussed in the previous chapters included the quantitative comparison of the optical conductivities ( $\sigma$ ) of known monolayer graphene and *h*-BN, and the D band Raman imaging of CVD graphene with an independently measured grain structure.

In the following two chapters, we combine DF-TEM with the microscopy techniques described in Chapters 3 and 4 to establish the relationships between the stacking structure, optical absorption, and Raman scattering spectra of twisted bilayer graphene (tBLG) samples. As discussed in Chapter 1, interlayer rotation is a unique degree of freedom available in stacked 2D materials, and its effects on the properties of these materials were poorly understood until recently. A significant proportion of the bilayer graphene produced by CVD is tBLG, where the layers are rotated by a relative angle  $\theta$ . Several previous studies of tBLG provided evidence of intriguing,  $\theta$ -dependent electronic and optical properties, such as new van Hove singularities in its electronic density of states and additional peaks in its optical absorption spectrum. However, despite the abundance of tBLG in CVD-grown samples and the growing scientific interest in this material, previous studies were not comprehensive enough to generalize the properties of tBLG

for arbitrary  $\theta$ , because they lacked the capability to determine  $\theta$  both accurately and over a large area for many samples.

For the first time, we determine quantitative relationships between  $\theta$  and the optical response of tBLG over a large energy and angle range. In this chapter, after reviewing the previous theoretical and experimental studies of the electronic properties of tBLG, we provide a theoretical description of its optical properties. Then, we compare these calculations to our experimental results, and apply our new structure-property relationships for precise, all-optical characterization of CVD-grown tBLG samples. This chapter sets the stage for examining more complex, many-body optical processes in tBLG in Chapter 6, including excitonic effects and Raman scattering. Sections of this chapter were adapted from [1], [2], and [3].

## 5.2 | Defining the physical structure of tBLG

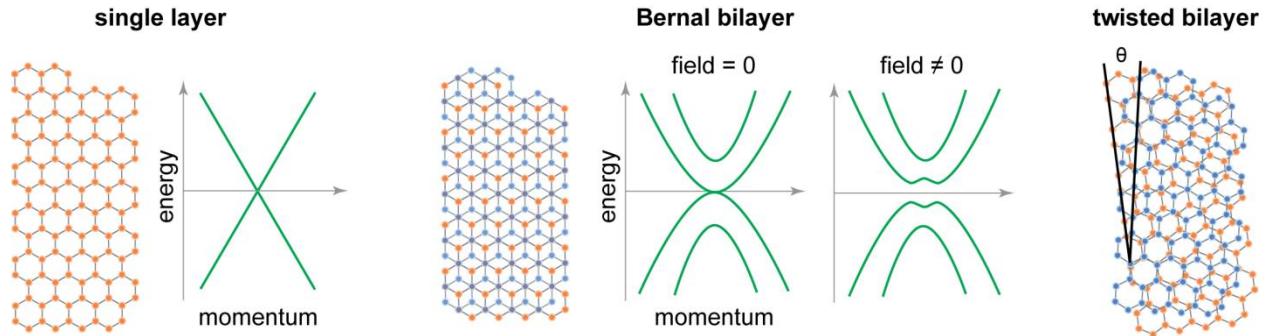


**Figure 5.1: Single layer, Bernal, and twisted bilayer graphene**

Illustrations of the physical structure of single layer, Bernal stacked bilayer, and twisted bilayer graphene. For single layer and Bernal bilayer graphene, we also include schematics of their low energy band structures. Single layer graphene has linear bands, while Bernal bilayer graphene has quadratic bands with a gap that opens under an applied vertical electric field.

While monolayer graphene has a unique linear band structure (Figure 5.1) and a high carrier mobility, it does not have a band gap, limiting its potential applications. However, the low energy band structure of oriented, or Bernal stacked, bilayer graphene is significantly different:

the bands are quadratic, and a band gap can be opened under an applied vertical electric field [4,5]. The earliest studies of exfoliated bilayer graphene were performed on Bernal stacked samples, because these samples originated from high quality bulk crystals of graphite in which all layers were oriented.

An additional structure is possible in lower quality bulk graphite: turbostratic stacking, where the orientations between neighboring layers are random. Exfoliated monolayer samples can also occasionally fold over on themselves, creating bilayer samples with random interlayer rotation [6,7]. Finally, as discussed in Chapter 1, twisted bilayer graphene (tBLG) is often produced in CVD-grown samples. Understandably, the earliest interest in these samples regarded their low energy band structure: would it resemble that of single layer graphene, or of Bernal stacked bilayer graphene? Later, theoretical studies continued in more detail once it was discovered that there were a variety of interesting,  $\theta$ -dependent phenomena in the band structure of tBLG. Early theoretical and experimental findings in this area will be discussed in more detail in Section 5.3.

First, however, one of the primary challenges for theoretical studies of tBLG is to define the physical structure of a given sample. In order to rigorously define a band structure of a material, it must be possible to describe the physical structure with an infinitely repeating unit cell of finite size. For tBLG, there are certain *commensurate* structures with finite unit cells. Examples of commensurate twisted bilayer graphene are shown in Figure 5.2.

There is also an alternative, more intuitive way to define the structure of tBLG. Starting from Bernal stacked bilayer graphene, one of the two layers can be rotated by an angle ( $\theta$ ) around a perpendicular axis which includes an atom from each layer. After rotation, the top layer

can be translated by an arbitrary vector. This combination of rotation and translation can describe any possible tBLG structure, including *incommensurate* tBLG, where no unit cell can be defined.

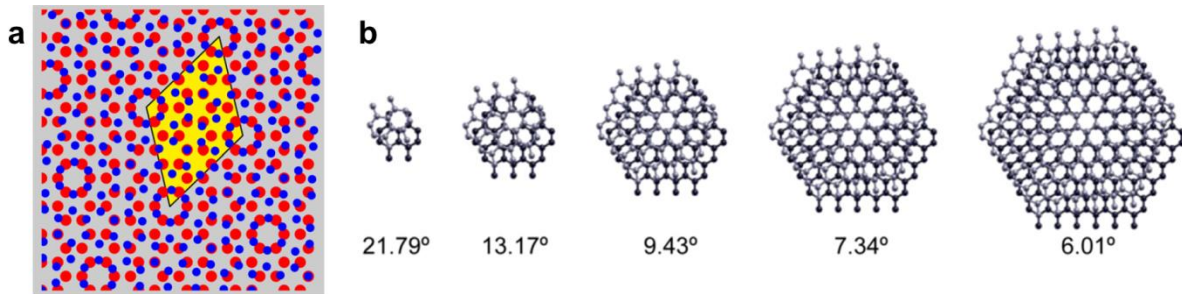


**Figure 5.2: Commensurate tBLG**

(a) The structure of commensurate,  $27.8^\circ$  twisted bilayer graphene. Its unit cell (yellow region) contains 52 atoms. [8] (b) tBLG with decreasing  $\theta$ , showing the emergence of a clear moiré pattern at lower angles with periodicity inversely proportional to  $\theta$ . [9]

Converting between these two structural descriptions of tBLG is challenging. Figure 5.3 plots the unit cell size of tBLG as a function of rotation angle. While there are a few special angles with very small unit cells ( $<100$  atoms), many values of  $\theta$  provide unit cells which contain thousands or more atoms, and for every possible commensurate tBLG structure there are infinitely many incommensurate structures. Thus, for nearly all possible  $\theta$ , the large unit cell size makes it difficult or impossible to calculate the band structure with standard computational methods. In addition, a very small change in  $\theta$  leads to a very large change in unit cell size. Finally, the minimum unit cell size (dashed blue line) increases rapidly when  $\theta$  is close to  $0^\circ$  or  $60^\circ$ , corresponding to layers that are very nearly oriented. This is due to the large moiré periodicity of low twist angle tBLG; in general, a clear, hexagonally symmetric moiré pattern emerges in both commensurate and incommensurate tBLG when  $\theta < \sim 10^\circ$ , whose periodicity is inversely proportional to  $\theta$ . Examples of the moiré for several commensurate cases are shown in Figure 5.2b.

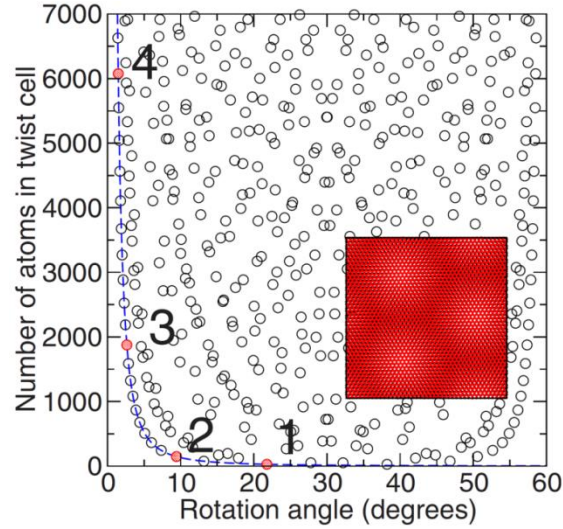


**Figure 5.3: Unit cell size vs.  $\theta$**

A plot of the unit cell size vs.  $\theta$  for tBLG. This plot illustrates how a very small change in  $\theta$  can lead to a very large change in unit cell size. In addition, the minimum unit cell size (blue line) increases rapidly as  $\theta$  decreases, due to the large spatial period of the resulting moiré pattern (inset). [10]

The important point is to determine which of these two structural descriptions is best correlated with the properties of tBLG. A few initial theoretical studies found unit cell-dependent properties in tBLG at very low energies [11]. However, the majority of theoretical [10,12,13] and experimental [14] studies, including our own, have found that most observable properties of tBLG (such as the energies of the interlayer van Hove singularities, described in the next section) show a smooth relationship with  $\theta$ . Furthermore, many studies have provided evidence that the structural description of tBLG can be further simplified. The relative translation between the tBLG layers does not affect its properties [13], and no measurable properties have been found to depend on the handedness of the rotation, so one parameter,  $0^\circ < \theta \leq 30^\circ$ , is usually sufficient to define the structure of tBLG.

Additionally, we note that our extensive characterization of CVD-grown tBLG has shown that the structure of tBLG is not rigid, and  $\theta$  can vary spatially. Because of the known superlubricity of twisted layers of graphene and graphite [15,16], the same property that makes

graphite an excellent lubricant, there is little to prevent spatial variations in  $\theta$  in a macroscopic sample. Subsequently, in a sample where the layers experience variations in strain or shear, spatially varying  $\theta$  is probably commonplace. An example where we were able to observe this phenomenon experimentally is shown in Figure 5.4 [17], which is a DF-TEM image of a CVD-grown trilayer sample. The top and bottom layers are nearly oriented, while the middle layer is twisted. If the top and bottom layers maintained identical orientations and lattice constants throughout the trilayer region, we could expect a homogeneous DF-TEM image. Instead, we observe spatially varying moiré fringes, which reflect spatial variations in strain, shear, and relative rotation between the two layers.

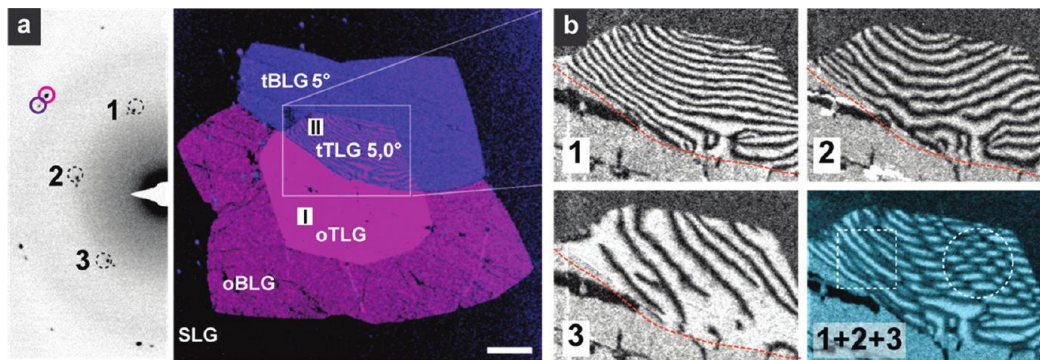


**Figure 5.4: Spatially varying structure in twisted multilayer graphene**

A DF-TEM image of trilayer CVD graphene in which the top and bottom layers are very nearly oriented, and the center layer is slightly twisted. The complex moiré patterns between the top and bottom layers (b) show spatially varying strain, shear, and rotation. [17]

Thus, the most accurate way to describe CVD-grown tBLG is likely by an average  $\theta$ , with the understanding that there are some local spatial variations of a fraction of a degree. The idea of defining a rigid unit cell is only theoretically relevant, since tiny variations away from an angle corresponding to a commensurate structure produce tBLG with a completely different unit cell. However, this is still a useful description of tBLG for the purpose of comparing experiment

to theory. In particular, computationally taxing *ab initio* band structure calculations can only be performed for tBLG with a small unit cell. Despite this, it appears that most of the behavior found in these calculations for a few specific angles can be extrapolated to describe the behavior of tBLG at other angles [12,18].

### 5.3 | Electronic properties

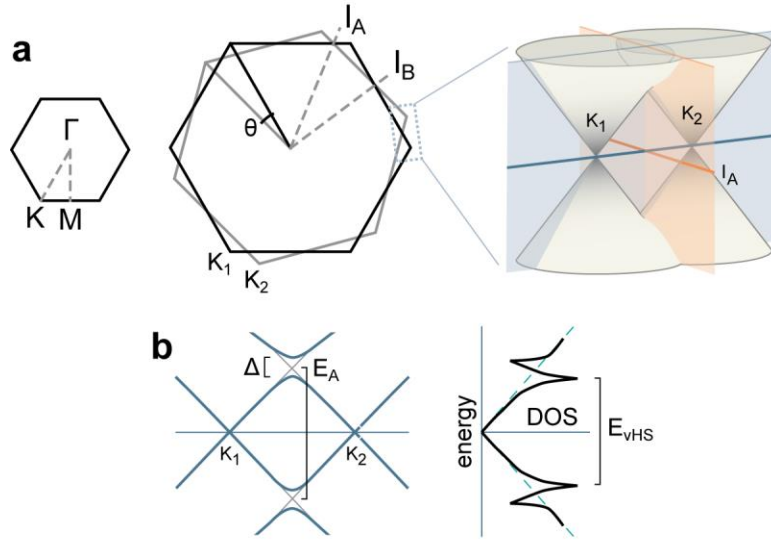


**Figure 5.5: Continuum model of tBLG band structure**

(a) The two Brillouin zones corresponding to each layer in tBLG, rotated by the same relative angle as the interlayer rotation. The bands from each layer intersect along two distinct lines,  $I_A$  and  $I_B$ . The zoomed in area shows the cones from each layer. (b) The band structure of tBLG along the blue line in (a). A minigap of energy  $\Delta$  is formed where the cones intersect. The point at the bottom of the minigap is a saddle point, and its corresponding vHS in the DOS of tBLG is shown.

Early density functional theory (DFT) calculations of the band structure of commensurate tBLG quickly demonstrated that tBLG has a low energy band structure very similar to that of monolayer graphene [19]. However, seminal work by Dos Santos *et al.* showed that while a band gap does not open in tBLG under the influence of a vertical electric field, van Hove singularities (vHSs) appear in the band structure of tBLG at higher energies which depend on  $\theta$  [20]. This

theoretical work and several others [13] were able to overcome the issue of defining a commensurate structure for tBLG by treating the moiré pattern formed by the twisted layers (see Figure 5.2 and Figure 5.3) as a long wavelength structural perturbation for each layer. For simplicity, they assumed that the low energy band structure of each layer was a perfect Dirac cone. However, the long wavelength approximation only holds for small  $\theta$  ( $< 10^\circ$ ), and the Dirac model does not capture deviations from the linear band structure in single layer graphene at higher energies ( $< 1$  eV) (see Figure 5.7).

This continuum model picture of the band structure of tBLG is illustrated in Figure 5.5. Here, we will also pause to introduce some notation which will be used throughout Chapters 5 and 6. First, Figure 5.5a shows the single layer graphene Brillouin zone, labeled with three high symmetry points:  $\Gamma$ , K, and M. The band structure of tBLG can be viewed as two sets of single layer graphene bands with a relative rotation of  $\theta$  around the  $\Gamma$  point (Figure 5.5a), and we label the high symmetry points from each layer with the notation  $K_1$  or  $K_2$ . Interlayer interactions perturb the bands from each layer where they intersect. This occurs along two distinct lines, which we will refer to as  $I_A$  and  $I_B$  (Figure 5.5a). Here, we define an important energy scale: the energy difference between the states where the bands from each layer just begin to cross (Figure 5.5b), which we will refer to as  $E_A$  and  $E_B$  for the intersections  $I_A$  and  $I_B$ , respectively. The theory in the following two sections will focus exclusively on  $E_A$ , but we will return to  $E_B$  in Section 5.5.

Due to the electronic interactions between the layers, the eigenstates near these intersections are then hybridized between both layers. This produces a minigap of energy  $\Delta$ , which is  $\sim 0.2$  eV for tBLG [21]. The band hybridization also forms new saddle points in the band structure of tBLG, and thus new vHSs in the density of states (DOS) of the material. A

schematic of the DOS of tBLG vs. energy is shown in Figure 5.5b. From our model, the energy separation between these vHSs is  $E_{\text{vHS}} = E_A - \Delta$ .

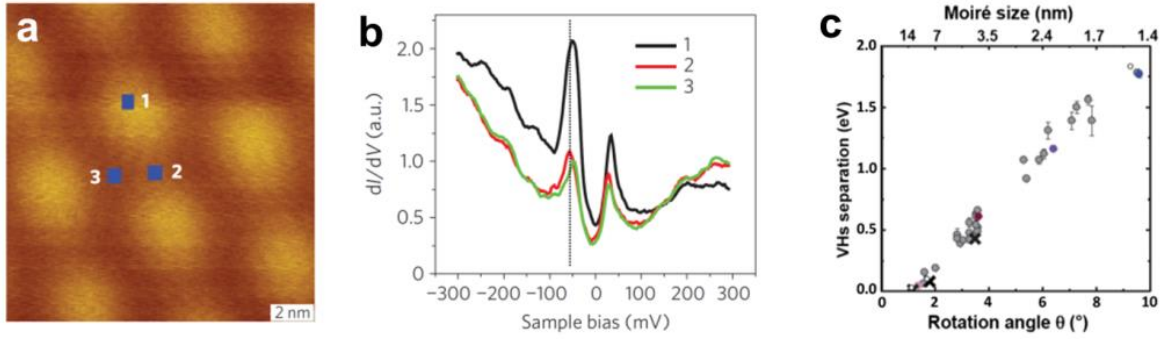


**Figure 5.6: Experimental studies of the tBLG DOS**

(a) STM image of  $1.79^\circ$  tBLG, which exhibits a large moiré pattern. (b) STS spectra of the same sample, which exhibit peaks corresponding to vHSs in the material's DOS. [22] (c) The separation between vHSs vs.  $\theta$  for a group of samples, determined by STS. The relationship is approximately linear. [14]

These vHSs were observed experimentally in 2009 for low angle tBLG using scanning tunneling spectroscopy (STS), which probes the local density of states spectrum of a material as discussed in Chapter 2 [22]. Figure 5.6a shows an STM image of tBLG grown with CVD on a nickel substrate. The twist angle of this sample can be determined by the period of the large moiré pattern, which corresponds to a small,  $1.79^\circ$  twist. Van Hove singularities are observed in the STS spectra of this sample taken at a variety of locations, shown in Figure 5.6b. Further STS experiments confirmed the robust nature of these vHSs in tBLG, and found an approximately linear relationship between the  $E_{\text{vHS}}$  and  $\theta$  for  $1^\circ < \theta < 10^\circ$  [14]. In addition, the tBLG band structure illustrated in Figure 5.5 was recently directly confirmed with ARPES measurements [21].

The linear relationship between the tBLG  $E_{\text{vHS}}$  and  $\theta$  for small  $\theta$  reflects the linear low energy band structure of graphene. From Figure 5.5, it can be seen that as  $\theta$  increases, the

separation between  $K_1$  and  $K_2$ , and thus  $E_A$  and  $E_{vHS}$ , will also grow. Within the continuum model, it can be shown that  $E_A = 2v_F\kappa\sin(\theta/2)$ , where  $v_F$ , the Fermi velocity of graphene (i.e. the slope of the Dirac cone), is approximately  $10^6$  m/sec and  $\kappa = 4\pi/3a_0$ , where  $a_0 = 2.46 \text{ \AA}$  is the graphene lattice constant [20]. This equation predicts a linearly increasing  $E_A$  (and hence  $E_{vHS}$ ) for small  $\theta$  with a slope of roughly  $1 \text{ eV}/5^\circ$ , and provides a close fit to the data in Figure 5.6c.

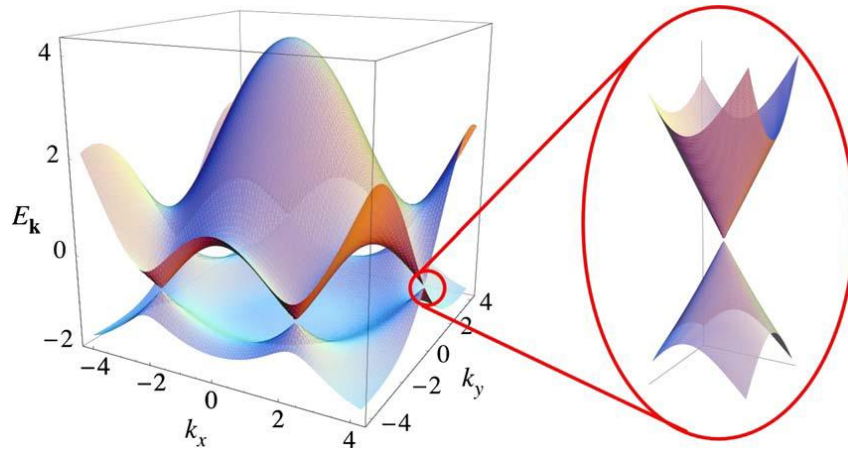


**Figure 5.7: Full band structure of graphene**

The band structure of graphene, showing the linear dispersion near zero energy (right) as well as the deviations from linearity at higher energies. At higher energies ( $\sim \pm 2 \text{ eV}$ ; the energy scale in this plot is in units of the tight binding parameter  $t = 2.7 \text{ eV}$ ) there are saddle point vHSs in the band structure of single layer graphene. [23]

However, the energy range of STS is limited, such that it is difficult to observe the vHSs in tBLG with  $\theta > 10^\circ$ . This unexplored high angle regime is potentially very interesting. Although we have limited our discussion so far to the low energy band structure of single layer graphene and tBLG, it is well known that the graphene band structure deviates from linearity at higher energies. The full calculated band structure of single layer graphene is shown in Figure 5.7 (here, energy is plotted in units of a tight binding parameter  $t = 2.7 \text{ eV}$ ). The bands become sublinear and lose their electron-hole symmetry at energies greater than roughly  $\pm 1 \text{ eV}$ , and large saddle point vHSs are present at the M point with energies of roughly  $\pm 2 \text{ eV}$ . If we can experimentally

measure  $E_A$  and  $E_B$  in tBLG for the largely unexplored  $10^\circ < \theta < 30^\circ$  case, we will also be probing the band structure of single layer graphene over this entire energy range. In addition, the continuum model contains approximations which are not valid at higher angles, and it is important to examine whether the simple picture in Figure 5.5 continues to predict the properties of tBLG at higher energies.

The DUV-Vis-NIR hyperspectral microscope introduced in Chapter 3 is a clear choice for probing the properties of tBLG at higher angles and energies. Combined with DF-TEM, we can correlate  $\theta$  and the quantitative, full optical function of the same samples of tBLG for energies from 1.2 to 6.2 eV. Since the optical response of a material is related to its DOS, it is expected that we will observe  $\theta$ -dependent signatures in the optical response of tBLG at energies near  $E_{\text{vHS}}$ .

While this prediction is indeed correct, the theoretical description of the optical response of tBLG is somewhat more complex than that of the STS spectra which were discussed in this section. In the following section, we will describe the theory of the optical properties of tBLG in more detail.

#### **5.4 | Calculated optical properties of tBLG**

There are two factors which are important to consider when calculating the optical response of any material. The first is the joint density of states (JDOS), which is similar to the DOS described in the previous section. However, while the DOS counts the number of states within an absolute energy range  $E \pm \delta E/2$ , the JDOS counts the number of potential transitions between states with an energy *difference* of  $E \pm \delta E/2$ . Second, it is also necessary to consider the optical transition matrix element,  $M_{\text{op}}$ , for each possible transition, which defines a quantum mechanical

probability that a certain transition can occur. Symmetry considerations typically require that some potential transitions are allowed, while others are forbidden. The overall strength of the optical response of a material at a given energy depends on both the total number of transitions available at that energy (i.e. the JDOS) and  $|M_{\text{op}}|^2$  for each transition.

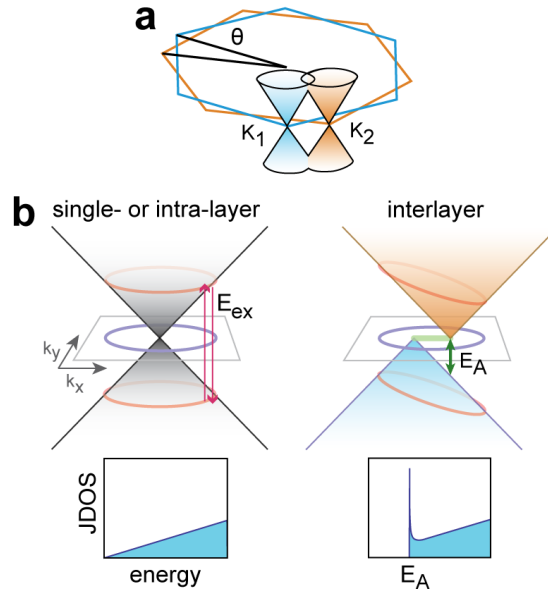


**Figure 5.8: JDOS in tBLG**

(a) Band structure of tBLG for non-interacting layers. The Dirac cones from each layer (orange, blue) are separated in  $k$ -space by the twist angle  $\theta$ . (b) Schematics of the two types of optical transitions, intra- and interlayer, which conserve momentum in non-interacting tBLG. No interlayer transitions are allowed below  $E_A$ , but there is a large singularity in the interlayer JDOS at  $E_A$  due to the parallel valence and conduction bands. [1]

In this section, we separately examine both the JDOS and  $M_{\text{op}}$  for various transitions in tBLG. We introduce a new class of transitions, “parallel band” optical transitions, which are enabled by the interlayer coupling in tBLG. Based on our considerations, we conclude that parallel band optical transitions are the most important contribution to the  $\theta$ -dependent optical behavior of tBLG. We first presented the findings of this section in [1], which were further verified by an independent group of theorists in [12].

First, we discuss the JDOS for optical transitions in tBLG. Initially, we consider the band structure of tBLG for the case of non-interacting layers. In principle, there exist two types of transitions for every value of  $k$ : *intralayer* and *interlayer* optical transitions. The JDOS of single layer graphene, as well as intralayer transitions in tBLG, can be derived by mapping all of the states within a pair of Dirac cones sharing the same apex (K point) that satisfy the momentum and energy conservation for a given excitation energy,  $E_{ex}$ . These states form a pair of circles whose diameter increases linearly with  $E_{ex}$ , resulting in the well-known linear JDOS *vs.* energy ( $E$ ) (Figure 5.8b, left). We initially use the same selection rules to examine interlayer transitions (Figure 5.8b, right). From Figure 5.8b, it is clear that interlayer transitions are forbidden at energies below  $E_A$ . However, there are many states between  $K_1$  and  $K_2$  where the valence and conduction cones run parallel to each other, with a transition energy near  $E_A$ .

We can analytically derive the JDOS for this transition as a function of  $E_{ex}$ . For a given momentum  $k$ , the energy of initial state in the valence band of the first layer is  $E_{1v} = -\hbar v_F |k - K_1|$ . Similarly, the energy of the final state in the conduction band is  $E_{2c} = \hbar v_F |k - K_2|$ . Therefore, states that fulfill energy conservation satisfy  $|k - K_1| + |k - K_2| = E_{ex} / (\hbar v_F)$ . Since an ellipse is a collection of points that has the same combined distance from two foci, this shows that the locus of allowed  $k$  states is an ellipse with  $K_1$  and  $K_2$  as its two foci and  $k_a = E_{ex} / (2\hbar v_F)$  and  $k_b = (k_a^2 - (|K_1 - K_2|/2)^2)^{1/2}$  as its major and minor radii, respectively ( $|K_1 - K_2| = \Delta K$ ). The area of this ellipse in the momentum plane is  $A(E_{ex}) = \pi k_a k_b$ , and the JDOS is proportional to  $dA/dE_{ex}$ , or:

$$\left( \sqrt{1 - (\Delta/E_{ex})^2} + 1/\sqrt{1 - (\Delta/E_{ex})^2} \right) (E_{ex}/\pi \hbar^2 v_F^2)$$

This expression approaches the single layer JDOS for  $E_{ex} \gg E_A$ , but the second term diverges as  $E_{ex} \sim E_A$ , producing a singularity in the interlayer JDOS for tBLG (Figure 5.8b).

The electronic interaction between the two layers results in two main modifications to this model. First, splitting occurs at the degeneracy points in the band structure of tBLG (i.e. along  $I_A$  and  $I_B$ ). Second, near the degeneracy point, optical transitions are no longer strictly interlayer or intralayer, because the relevant states are hybridized from both layers. However, the bands corresponding to the original interlayer transition continue to run parallel to each other through the avoided crossing (see Figure 5.5 and Figure 5.11). We refer to the transitions between these bands as “parallel band” transitions, which captures their behavior both near and away from the degeneracy point. While the splitting leads to additional vHSs in the single-particle electronic density of states, as discussed in Section 5.3, it has a small effect on JDOS for both the parallel band and intralayer optical transitions, because the states affected by this splitting are a small subset of the total states which contribute to either type of transition. This can be seen from our numerical calculations in Figure 5.9 (splitting is introduced with a simplified 4-band model of the tBLG band structure [24]).

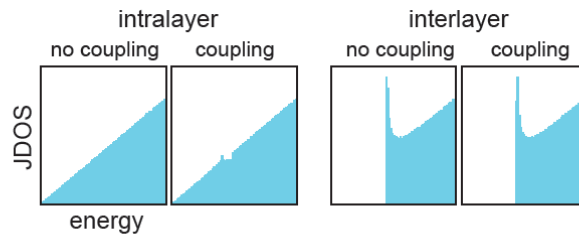


**Figure 5.9: Calculated JDOS with coupling**

Calculated JDOS vs. energy for intra- and interlayer (or “parallel band”) transitions with and without degeneracy point splitting. The introduction of interlayer coupling has very little effect on either JDOS. [1]

We next consider the optical transition matrix element,  $M_{op}$ , for both parallel band and intralayer transitions. We have used a tight binding model at a commensurate angle ( $13.2^\circ$ ) to calculate  $M_{op}$  for these transitions in tBLG. The calculations of the tBLG band structure are

performed using the VASP program (Vienna ab initio simulation program) employing the projector augmented wave method within the frozen-core approximation [25,26]. A cutoff energy of 250 eV and a  $6 \times 6 \times 1$  Gamma-centered k-point mesh ensures convergence of the band structure results. The tBLG structures are constructed using the graphene C-C bond length of 1.42 Å and an interlayer spacing of 3.35 Å.

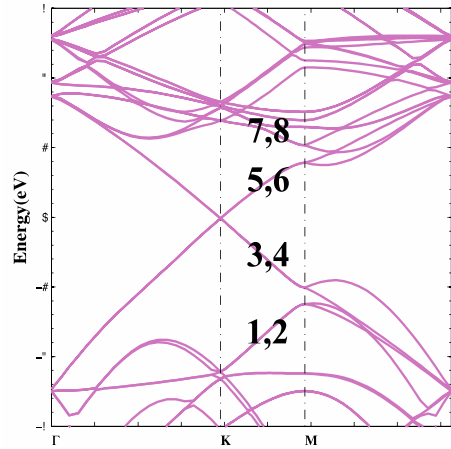


**Figure 5.10: Tight binding band structure of  $13.2^\circ$  tBLG**

Calculated band structure for  $\theta = 13.2^\circ$ . Bands used in calculations of  $M_{op}$  are labeled #1-8. [1]

The calculated band structure for a commensurate  $\theta = 13.2^\circ$  is shown in Figure 5.10. Comparing the band structure of commensurate tBLG to the familiar continuum model can be difficult because the larger unit cell of the commensurate structure results in a folded Brillouin zone. For this particular commensurate cell, the bands between the K and M symmetry points of the folded Brillouin zone lie in the same k-space plane as the continuum bands illustrated in Figure 5.5b. In addition, the bands in Figure 5.10 are doubly degenerate, because the cones from each layer fold on top of each other in the new Brillouin zone. Parallel band transitions are defined as  $1,2 \rightarrow 5,6$  (red in Figure 5.11) and  $3,4 \rightarrow 7,8$  (yellow), while intralayer transitions are  $3,4 \rightarrow 5,6$  (green) and  $1,2 \rightarrow 7,8$  (blue).

The calculations of the optical matrix elements are performed using an orthogonal tight-binding model. The parameters for the intra-layer coupling and the coupling Hamiltonian matrix elements for the  $p_z$  orbitals localized on atoms in different layers are taken from [27]. Comparisons of the tight-binding band structures with the density functional calculations confirm the accuracy of the tight-binding parameterization. In addition to band structures, we calculate the optical absorption using Fermi's golden rule:  $\eta = 2\pi/\hbar |M_{op}|^2 \rho$ , where  $\rho$  is the joint density of states. The optical matrix element  $M_{op}(\omega)$  which is defined as:

$$M_{op}(\omega) = \frac{ie}{\omega} E \left\langle \Psi_c \left| \frac{P}{m_e} \right| \Psi_v \right\rangle$$

where  $e$  is the electron charge,  $\omega$  is the photon frequency,  $E$  is the electric field of the light,  $m_e$  is the electron mass,  $P$  is the momentum operator,  $\Psi_c$  and  $\Psi_v$  are the wave functions for the conduction and the valence states of bilayer graphene, respectively [28]. The velocity matrix element ( $P/m_e$ ) above can be expressed by the gradient of the Hamilton as follows [29,30]:

$$M_{op}(\omega) = \frac{ie}{\hbar\omega} E \langle \Psi_k^c | \nabla_k H | \Psi_k^v \rangle$$

and this is the expression that we calculate in order to study the behavior of  $M_{op}$  for different transitions in tBLG.

As the result of these calculations, Figure 5.11 shows a plot of the square velocity matrix element ( $\propto (\omega |M_{op}|)^2$ ) in  $k$ -space for all possible types of transitions. Our work provides two central results. First, the intralayer transitions are suppressed near the degeneracy point. As discussed previously, the JDOS associated with these transitions is also relatively small.

Second, we find that the parallel band transitions are optically active for all hybridized states; their strength is maximum (almost equivalent to that of single layer graphene) near the degeneracy point, and monotonically decreases away from it, with a long tail. Considering both

the large JDOS (Figure 5.8b, right) and  $M_{op}$  for parallel band transitions, we expect that they should cause a measurable increase in absorption (proportional to  $JDOS \times |M_{op}|^2$ ) [31].

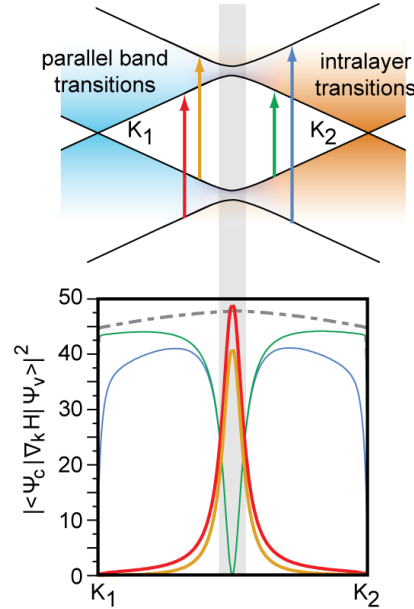


**Figure 5.11: Optical matrix element**

A slice through the band structure of tBLG, where interlayer interactions cause splitting of the electronic states near the degeneracy point (shaded). Possible parallel band and intralayer transitions are labeled. Below is a plot of the square velocity matrix element, which is proportional to  $|M_{op}|^2$ , for each transition type (calculated from a tight binding model at  $13.2^\circ$ ). The dashed line is the square velocity matrix element for intralayer transitions in single layer graphene. [1]

To summarize our results so far, our calculations predict that new optical transitions occur in tBLG for the states which are hybridized between both layers. The allowed optical transitions are those between parallel bands, and the large number of transitions with the same energy should lead to a new optical absorption peak in tBLG. The energy of this absorption peak should be equal to  $E_A$ ; in the continuum model approximation, this energy is  $2v_F k \sin(\theta/2)$ . Note that unlike the  $E_{VHS}$  discussed in Section 5.3, the energy of the tBLG optical absorption peak should independent of  $\Delta$ , assuming that  $\Delta$  is the same for the valence and conduction bands. We will return to this point in Section 5.5.

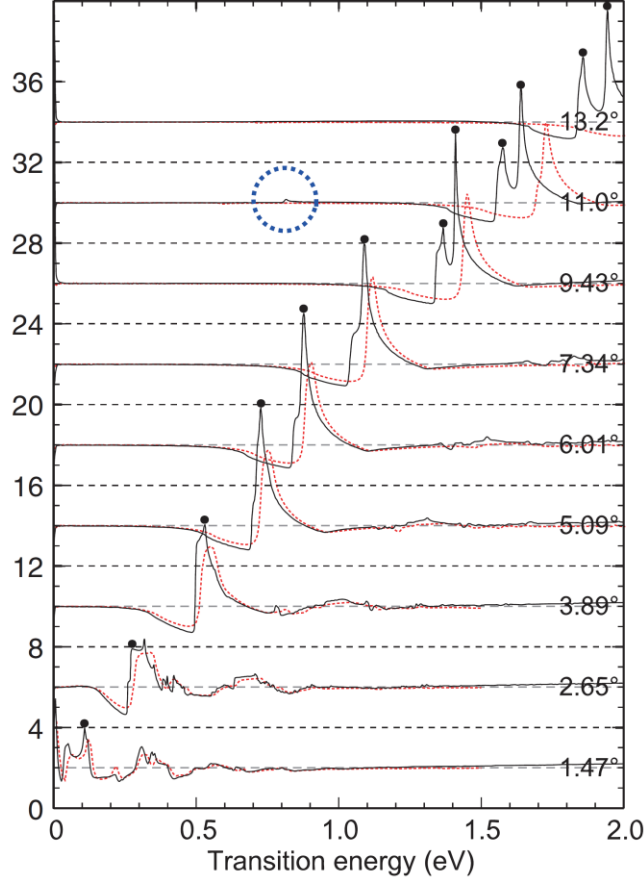


**Figure 5.12: Calculated optical absorption of tBLG**

Optical conductivity of tBLG calculated with a continuum model approximation (red lines) and a tight binding model (black lines) as a function of  $\theta$ . Conductivity is plotted in units of  $e^2/4\hbar$  and plots are offset by  $4e^2/4\hbar$  apiece. [12]

Finally, the actual calculated optical absorption spectra of tBLG are presented in Figure 5.12 as a function of increasing  $\theta$  (here, we present the results of Moon *et al.* [12]). Consistent with our predictions, tBLG is found to exhibit an absorption peak whose energy increases with increasing  $\theta$ . The shape of the calculated absorption peak is asymmetric, and reflects the  $1/E_{\text{ex}}^{1/2}$  functional form of the peak in the interlayer JDOS of tBLG (see Figure 5.8). In addition, the energy of this peak as a function of  $\theta$  is in qualitative agreement with the STS data in Figure 5.6. The work by Moon *et al.* also confirmed that the optical selection rules that we calculated for the  $13.2^\circ$  case hold for a variety of other commensurate angles.

Next, we present our experimental results of the quantitative optical conductivity of tBLG as a function of known  $\theta$ . Our data verifies our theoretical predictions, and we extend our model to account for the nonlinear single layer graphene band structure at high energies.

## 5.5 | Experimental results

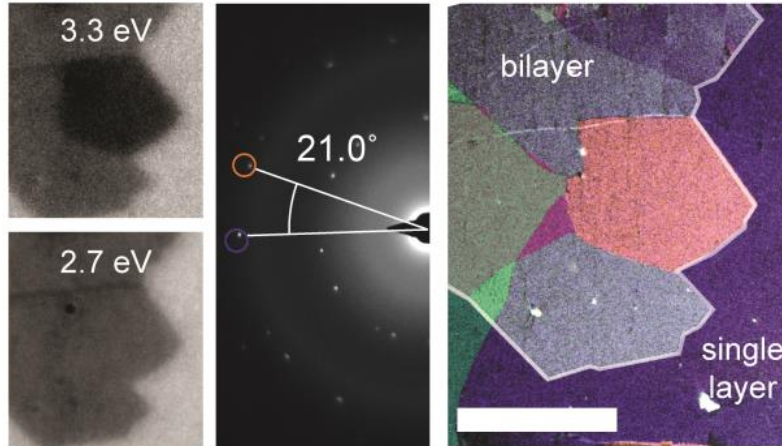


**Figure 5.13: Correlating optical absorption with  $\theta$**

The experimental procedure for imaging the optical conductivity and physical structure of the same tBLG domains. Here we illustrate that certain tBLG regions appear darker in a transmission image at specific energies, and that these regions correlate with rotational domains imaged with DF-TEM. [2]

The predicted optical behavior of tBLG outlined in Section 5.4 has been confirmed qualitatively in other experiments for a few domains over a small energy (1.4-3 eV) and  $\theta$  (below  $15^\circ$ ) range [1,7,32]. However, our hyperspectral optical imaging and DF-TEM measurements provide a direct way to measure the optical properties of tBLG with known  $\theta$  over a larger energy (1.2-6.2 eV) and  $\theta$  ( $6-30^\circ$ ) range. As shown in Figure 5.13, we find that distinct regions with decreased transmission appear in monochromatic images of CVD BLG. We confirm that these regions correspond to tBLG rotational domains, and measure their twist angle, by combining our optical measurements with DF-TEM.

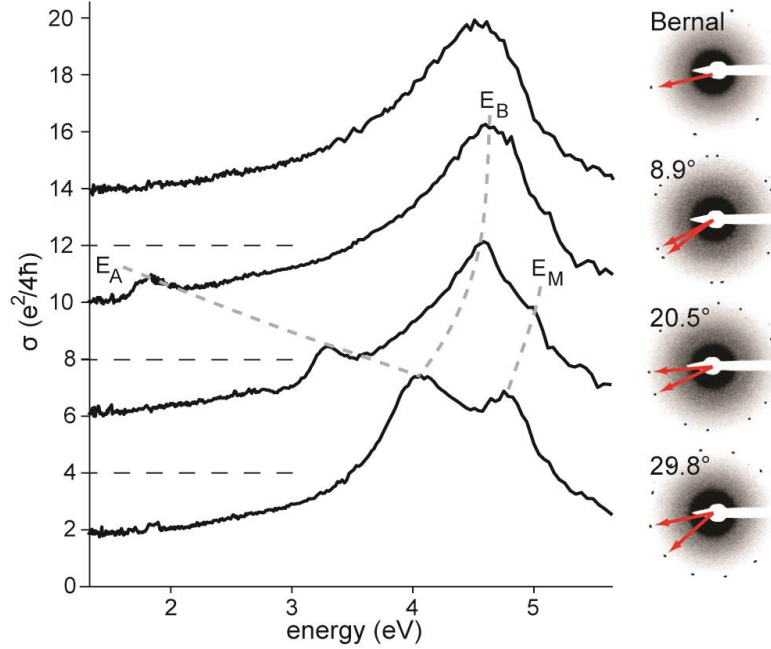


**Figure 5.14: Optical conductivity of tBLG**

(left) Measured  $\sigma$  spectra of BLG (top), and tBLG with increasing  $\theta$ . Dashed lines are guides to the eye indicating three features in the  $\sigma$  spectra of tBLG which are not found in BLG. Spectra are offset in  $\sigma$  by  $4e^2/4h$  apiece for clarity. (right) Electron diffraction patterns (inverted and contrast enhanced) from the same bilayer regions, indicating  $\theta$  for each. [3]

Using the experimental procedure outlined in Chapter 3, we have extracted the optical conductivity spectra for 34 CVD-grown tBLG domains (typically a few microns or larger in size) with  $8^\circ < \theta < 30^\circ$ . The twist angle of these domains is known to within a fraction of a degree after electron diffraction measurements of the same samples, which sit on electron-transparent, 10 nm thick silicon nitride windows [2]. While we obtain the full complex optical conductivity from a combination of reflection and transmission spectroscopy, we focus here on its real part, referred to as  $\sigma$ . The  $\sigma$  spectrum of tBLG at several angles is shown in Figure 5.14, and it exhibits a number of  $\theta$ -dependent features. Compared with Bernal stacked bilayer graphene (BLG) (top curve), which has a constant  $\sigma = 2e^2/4h$  at infrared and visible energies [31] and a peak due to its saddle point vHS near 4.6 eV [33,34], an extra  $\sigma$  peak appears in tBLG whose energy increases from  $\sim 2$  to 4 eV with increasing  $\theta$ . Consistent with previous experiments [7,32],

we assign this peak as the  $E_A$  feature in tBLG, discussed in Section 5.4. Additionally, at higher energies ( $\sim 4.5$ - $5$  eV), we find that the  $\sigma$  spectrum is also strongly modified compared to that of BLG. Most noticeable is the additional dip and peak which grows in magnitude as  $\theta$  increases, significantly modifying the  $\sigma$  spectrum of tBLG near  $30^\circ$ . This is due to the presence of two additional peaks,  $E_B$  and  $E_M$ , which we will assign based on our analysis in Figure 5.15 and Chapter 6, respectively.

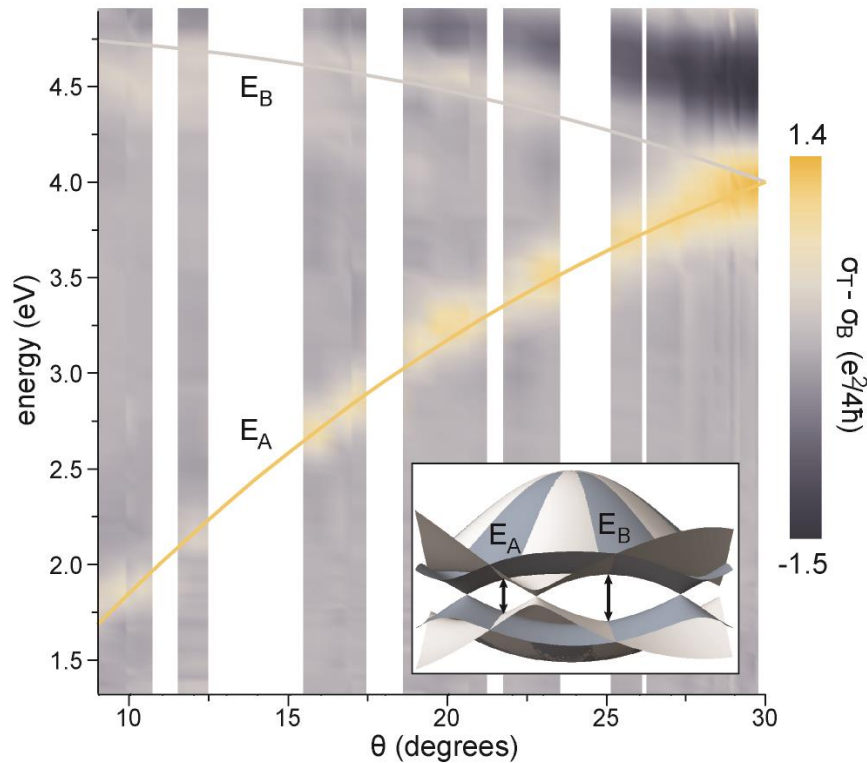


**Figure 5.15: 2D plot of tBLG optical conductivity**

A 2D plot of  $\sigma_T - \sigma_B$  combining all spectra. A linear background was subtracted from each spectrum after averaging every 10 nm. The two main features,  $E_A$  and  $E_B$ , are fit to the model described in the text (inset). [3]

To more clearly distinguish small changes in  $\sigma$  between tBLG and BLG, particularly the high energy features that are difficult to resolve over the large absorption peak at 4.6 eV, we subtract the  $\sigma$  of BLG ( $\sigma_B$ ) from that of tBLG ( $\sigma_T$ ). We examine the general trends in all of our

collected  $\sigma_T - \sigma_B$  spectra by combining them into a two-dimensional plot, as shown in Figure 5.15. Both the  $E_A$  and  $E_B$  features indicated in Figure 5.14 are clearly visible at all angles, and the two peaks each lie on single, monotonic curves (solid lines denoted as  $E_A$  and  $E_B$ , Figure 5.15) in energy vs.  $\theta$ .

The  $E_A$  and  $E_B$  peaks correspond to the two interlayer vHSs in the tBLG bands [12,20], as discussed in Sections 5.3 and 5.4. As we discussed previously for the  $E_A$  case, both of the optically allowed transitions near  $I_A$  have the same energy, which is independent of  $\Delta$  at the band intersection and can be calculated based on the band energies of single layer graphene for a given  $\theta$ . However, the applicability of this simple picture, based on the low energy continuum model, has not been experimentally confirmed for larger energies and angles. Our data show that both  $E_A$  and  $E_B$  can be accurately predicted using this model for  $\theta$  up to  $30^\circ$ , simply by assuming the selection rules shown in Figure 5.11 and the known single layer graphene band structure. We model the band structure of single layer graphene using the third-nearest-neighbor tight binding parameters from [35], which were fit to a first-principles GW calculation of the few-layer graphene band structure. Then, we calculate  $E_A$  and  $E_B$  as the local minima in the difference between the conduction and valence band energies,  $E_c - E_v$ , along  $I_A$  and  $I_B$ , respectively.

We obtain a remarkably close fit (solid lines, Figure 5.15) to both peaks after a 4% increase in energy. This increase is most likely because the parameters in [35] were fit to the calculated band structure of graphite, while weaker screening in single layer and bilayer graphene slightly increases the band energies. Our renormalized tight binding model provides a Fermi velocity ( $v_F$ ) of  $1.03 \times 10^6$  m/sec, similar to previous results for single layer graphene [36,37]. Furthermore, our data provide a facile, all-optical identification method for  $\theta$  in future samples. For convenience, we fit  $E_A$  to an empirical function  $\theta = A - (B - CE_A)^{1/2}$ , with  $\theta$  in

degrees and  $E_A$  in eV. We find  $A = 41.4$ ,  $B = 1.74 \times 10^3$ , and  $C = 3.99 \times 10^2 \text{ eV}^{-1}$  fit our data for  $8^\circ < \theta < 30^\circ$  with a slightly smaller total mean squared error than the fit in Figure 5.15.

The results presented in this section represent two major accomplishments of our work: the surprisingly high precision with which the tight binding band structure of single layer graphene can be fit to our data over a large energy range, and the quantitative relationship we have established between the absorption peak energy and  $\theta$  in tBLG. However, we can obtain even more insight into the optical properties of tBLG by studying the precise shapes of the spectral features in our high quality optical data. We will continue to examine our data in Chapter 6. To conclude Chapter 5, we will discuss applications for all-optical characterization of tBLG samples.

## 5.6 | Applications

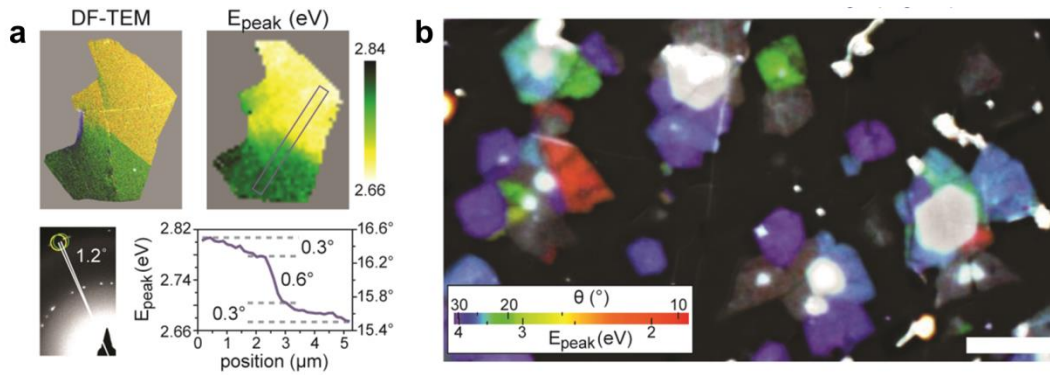


**Figure 5.16: All-optical  $\theta$  mapping**

(a) Comparison of DF-TEM (left) and pixel-by-pixel map of  $E_{\text{peak}}$  (i.e.  $E_A$ ) (right) for the same tBLG domain, illustrating that optical spectroscopy provides structural information with  $\theta \sim 0.1^\circ$  precision. See text for more details. (b) False color image of the resonance energies of many bilayer domains, illustrating the complex structure of tBLG grown by CVD (scale bar  $10 \mu\text{m}$ ). [2]

As shown in Figure 5.15, we have found that  $E_A$  is a robust probe of  $\theta$  in tBLG. This allows precise optical mapping of  $\theta$  as a function of position with submicron resolution, as shown in Figure 5.16a. In a color composite DF-TEM image (Figure 5.16a, left), we examine a tBLG

sample with  $\theta \sim 16^\circ$ , which has an additional low angle ( $\Delta\theta < 1.2^\circ$ ) boundary between the upper and lower regions. More precise spatial mapping of  $\theta$  with TEM would require collecting individual diffraction patterns from many small selected areas. However, this same feature is easily distinguished in a spatial map of  $E_A$  of the same region (Figure 5.16a, top right), based on which we estimate  $\Delta\theta$  to be a  $0.6^\circ$  using our fit in Figure 5.15. Furthermore, we observe continuous spatial variations in  $\theta$  of a few tenths of a degree away from the sharp boundary, as seen in a line cut (Figure 5.16a, bottom right) through the map of  $E_A$ . These small variations in  $\theta$  are consistent with previous DF-TEM studies of CVD-grown BLG (see Figure 5.4) [17], and may be the result of local shear or strain during growth.

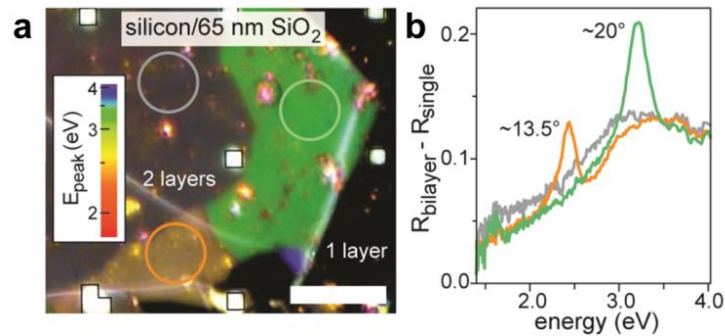


**Figure 5.17: tBLG imaging on Si/SiO<sub>2</sub>**

(a) False color image of BLG on Si/SiO<sub>2</sub> (65 nm); the grid of white dots (outlined) are gold alignment marks for use in further device fabrication (scale bar 10  $\mu\text{m}$ ). (b) Reflection spectra of the regions circled in (a). [2]

On a larger scale, a false color image mapping  $E_A$  reveals the striking domain structure of our CVD BLG, and directly determines  $\theta$  for all tBLG areas with optical resonances (Figure 5.16b). Currently, our microscope can measure optical features above 1.2 eV (corresponding to  $\theta > 6^\circ$ ), limited by the poor infrared sensitivity of our CCD. By comparing our optical and TEM data, we observe that 90% area of BLG without an absorption peak is Bernal stacked, a reflection

of the previously reported abundance of Bernal stacked, and lack of small  $\theta$ , bilayer graphene in CVD samples [17].

Furthermore, we can also determine  $\theta$  of tBLG on an Si/SiO<sub>2</sub> substrate, a geometry which could enable the fabrication of electronic devices with known  $\theta$ . Decreasing the oxide thickness compared to the 285 nm oxide example in Chapter 3 allows reflection spectroscopy over a broad range of energies by increasing the energy difference between zero contrast points (for example, see ~2.7, 4.2, and 5.5 eV for single-layer graphene on 285 nm oxide in Figure 3.9). Figure 5.17a shows a false color image (as in Figure 5.16b) of a bilayer graphene sample on Si/SiO<sub>2</sub> with 65 nm oxide, which resolves two colored tBLG domains and a gray, spectrally featureless (Bernal or small  $\theta$ ) BLG domain. Full reflection spectra between 1.4 and 4.1 eV from these regions are shown in Figure 5.17b, allowing us to determine  $\theta$  (~13.5° and 20°) for both tBLG domains. This capability will allow the fabrication of electronic and optoelectronic devices based on individual tBLG domains with different  $\theta$  as well as heterojunctions formed between them.

## 5.7 | Conclusion

Twisted bilayer graphene is an intriguing material, and attempts to understand the properties of this seemingly simple system have challenged theorists and experimentalists alike for many years. In this chapter, we described the challenges of modeling the physical structure of tBLG, and provided a thorough theoretical basis for the electronic and optical properties of tBLG. Then, we combined DF-TEM and DUV-Vis-NIR hyperspectral imaging to establish a quantitative relationship between the optical absorption peak energies of tBLG and its twist angle over a large energy and angle range. We connected our experimental results with our theoretical

predictions, and used our new structure-property relationships for all-optical characterization of tBLG on a variety of substrates.

In Chapter 6, we will continue our exploration of tBLG with a discussion of many-body optical processes in this material. Excitons (i.e. electron-hole interactions) are known to play an important role in the optical response of single layer graphene, and we will show that they also affect the optical response of tBLG. Furthermore, tBLG shows a number of  $\theta$ -dependent features in its Raman scattering (i.e. electron-phonon interactions) spectrum, and we will combine widefield Raman imaging and DF-TEM to study these effects in more detail.

## References

- [1] R. Havener, H. Zhuang, L. Brown, R. Hennig, and J. Park, *Nano Letters* **12**, 3162 (2012).
- [2] R. W. Havener, C. J. Kim, L. Brown, J. W. Kevek, J. D. Sleppy, P. L. McEuen, and J. Park, *Nano Letters* **13**, 3942 (2013).
- [3] R. W. Havener, Y. Liang, L. Brown, L. Yang, and J. Park, *Nano Letters* **14**, 3353 (2014).
- [4] F. Wang, Y. B. Zhang, C. S. Tian, C. Girit, A. Zettl, M. Crommie, and Y. R. Shen, *Science* **320**, 206 (2008).
- [5] K. F. Mak, C. H. Lui, J. Shan, and T. F. Heinz, *Physical Review Letters* **102**, 256405 (2009).
- [6] Z. Ni, L. Liu, Y. Wang, Z. Zheng, L. Li, T. Yu, and Z. Shen, *Physical Review B* **80**, 125404 (2009).
- [7] Y. Wang, Z. Ni, L. Liu, Y. Liu, C. Cong, T. Yu, X. Wang, D. Shen, and Z. Shen, *ACS Nano* **4**, 4074 (2010).
- [8] E. Mele, *Journal of Physics D-Applied Physics* **45**, 154004 (2012).
- [9] T. Mendes-de-Sa, A. Goncalves, M. Matos, P. Coelho, R. Magalhaes-Paniago, and R. Lacerda, *Nanotechnology* **23**, 475602 (2012).
- [10] S. Shallcross, S. Sharma, E. Kandelaki, and O. Pankratov, *Physical Review B* **81**, 165105 (2010).
- [11] E. Mele, *Physical Review B* **81**, 161405 (2010).
- [12] P. Moon and M. Koshino, *Physical Review B* **87**, 205404 (2013).
- [13] R. Bistritzer and A. MacDonald, *PNAS* **108**, 12233 (2011).
- [14] I. Brihuega, P. Mallet, H. Gonzalez-Herrero, G. de Laissardiere, M. Ugeda, L. Magaud, J. Gomez-Rodriguez, F. Yndurain, and J. Veuillen, *Physical Review Letters* **109**, 196802 (2012).
- [15] M. Dienwiebel, G. Verhoeven, N. Pradeep, J. Frenken, J. Heimberg, and H. Zandbergen, *Physical Review Letters* **92**, 126101 (2004).
- [16] Z. Liu, J. Yang, F. Grey, J. Liu, Y. Liu, Y. Wang, Y. Yang, Y. Cheng, and Q. Zheng, *Physical Review Letters* **108**, 205503 (2012).
- [17] L. Brown, R. Hovden, P. Huang, M. Wojick, D. A. Muller, and J. Park, *Nano Letters* **12**, 1609 (2012).
- [18] S. Shallcross, S. Sharma, and O. Pankratov, *Physical Review B* **87**, 245403 (2013).
- [19] S. Latil, V. Meunier, and L. Henrard, *Physical Review B* **76**, 201402 (2007).

- [20] J. dos Santos, N. Peres, and A. Castro, *Physical Review Letters* **99**, 256802 (2007).
- [21] T. Ohta, J. T. Robinson, P. J. Feibelman, A. Bostwick, E. Rotenberg, and T. E. Beechem, *Physical Review Letters* **109**, 186807 (2012).
- [22] G. Li, A. Luican, J. dos Santos, A. Neto, A. Reina, J. Kong, and E. Andrei, *Nature Physics* **6**, 109 (2010).
- [23] A. Castro Neto, F. Guinea, N. Peres, K. Novoselov, and A. Geim, *Reviews of Modern Physics* **81**, 109 (2009).
- [24] R. de Gail, M. Goerbig, F. Guinea, G. Montambaux, and A. Neto, *Physical Review B* **84**, 045436 (2011).
- [25] G. Kresse and J. Furthmuller, *Physical Review B* **54**, 11169 (1996).
- [26] G. Kresse and D. Joubert, *Physical Review B* **59**, 1758 (1999).
- [27] E. Morell, P. Vargas, L. Chico, and L. Brey, *Physical Review B* **84**, 195421 (2011).
- [28] A. Jorio, M. Dresselhaus, R. Saito, and G. F. Dresselhaus, *Raman Spectroscopy in Graphene Related Systems* (Wiley-VCH, 2011).
- [29] L. Johnson and G. Dresselhaus, *Physical Review B* **7**, 2275 (1973).
- [30] Y. Ho, Y. Chiu, D. Lin, C. Chang, and M. Lin, *ACS Nano* **4**, 1465 (2010).
- [31] R. Nair, P. Blake, A. Grigorenko, K. Novoselov, T. Booth, T. Stauber, N. Peres, and A. Geim, *Science* **320**, 1308 (2008).
- [32] J. T. Robinson, S. W. Schmucker, C. B. Diaconescu, J. P. Long, J. C. Culbertson, T. Ohta, A. L. Friedman, and T. E. Beechem, *ACS Nano* **7**, 637 (2012).
- [33] K. Mak, J. Shan, and T. Heinz, *Physical Review Letters* **106**, 046401 (2011).
- [34] D. Chae, T. Utikal, S. Weisenburger, H. Giessen, K. von Klitzing, M. Lippitz, and J. Smet, *Nano Letters* **11**, 1379 (2011).
- [35] A. Gruneis, C. Attacalite, L. Wirtz, H. Shiozawa, R. Saito, T. Pichler, and A. Rubio, *Physical Review B* **78**, 205425 (2008).
- [36] D. Miller, K. Kubista, G. Rutter, M. Ruan, W. de Heer, P. First, and J. Stroscio, *Science* **324**, 924 (2009).
- [37] A. Luican, G. Li, A. Reina, J. Kong, R. Nair, K. Novoselov, A. Geim, and E. Andrei, *Physical Review Letters* **106**, 126802 (2011).

## Chapter 6 : MANY-BODY OPTICAL PROCESSES IN TWISTED BILAYER GRAPHENE

### 6.1 | Introduction

Although twisted bilayer graphene appears to be a conceptually simple system, our discussion in Chapter 5 revealed that even a single particle description of the electronic and optical properties of tBLG can be quite complex. Even more exotic physics and new phenomena can be found in the many-body interactions in tBLG, including excitonic (i.e. electron-hole) effects and Raman (i.e. electron-phonon) scattering. In this chapter, we will attempt to understand the effects of a number of many-body processes on the optical properties of tBLG. As in Chapter 5, we will compare our experimental results with various theoretical models in order to ascribe physical meaning to our data. However, we note that both electron-hole and electron-phonon processes are extremely difficult to model in any material, let alone tBLG, and that the assumptions used in these models leave more room for error than for the single particle case. Hence, having access to the high quality experimental data presented in this chapter is even more important in order to confirm these theoretical predictions and identify their shortcomings.

We will first begin Chapter 6 where we left Chapter 5, and compare our experimental optical conductivity spectra of tBLG to the single particle, tight binding calculations by Moon *et al.* (see the end of Section 5.4) [1]. As discussed previously, many experimental studies of tBLG focused on relatively low energies where single layer graphene has a linear band structure. On the contrary, the band structure of single layer graphene becomes more complex at higher energies: the bands lose their linearity, electrons and holes are no longer symmetric, and a saddle point vHS occurs at the M point in the graphene Brillouin zone. We will discuss how this

asymmetry and nonlinearity affects the  $\theta$ -dependent vHSs and associated optical properties in tBLG.

In addition, the detailed absorption spectra we measure differ significantly, particularly at large  $\theta$ , from those calculated using the tight binding model. While it is known that there are resonant excitons associated with the M point vHS in single layer graphene, the excitonic effects associated with the interlayer vHSs in tBLG have not been studied. Furthermore, new excitonic states could form as coherent combinations of the multiple intralayer and interlayer vHSs in tBLG, particularly those closest in energy. Indeed, we find that new first-principles calculations which account for electron-hole interactions are needed to describe our data. Moreover, we observe signatures of coherence between the multiple vHSs in tBLG, which have similar energies at large  $\theta$ , in the form of the enhancement of the lower energy optical response and suppression of the higher energy features. We also discuss a new theory for potential bound excitonic states in tBLG.

Finally, we will discuss the Raman spectrum of tBLG as a function of  $\theta$ , obtained by combining widefield Raman and DF-TEM measurements. We observe a variety of  $\theta$ -dependent variations in the intensities, widths, and positions of the Raman G and 2D peaks for tBLG. The most striking feature we observe is a very strong enhancement of the Raman G peak, up to  $20\times$  that of single layer graphene, when the tBLG is excited on resonance with its optical absorption peak energy. We find that this enhancement can be explained by quantum coherence effects in the Raman scattering process, and we apply our experimental results toward preliminary studies of interlayer coupling in artificially stacked tBLG. Sections of this chapter were adapted from [2] and [3]. We note that many of the Raman results from [3] were also published concurrently by a different group in [4].

## 6.2 | Tight binding description of tBLG optical absorption vs. experiment

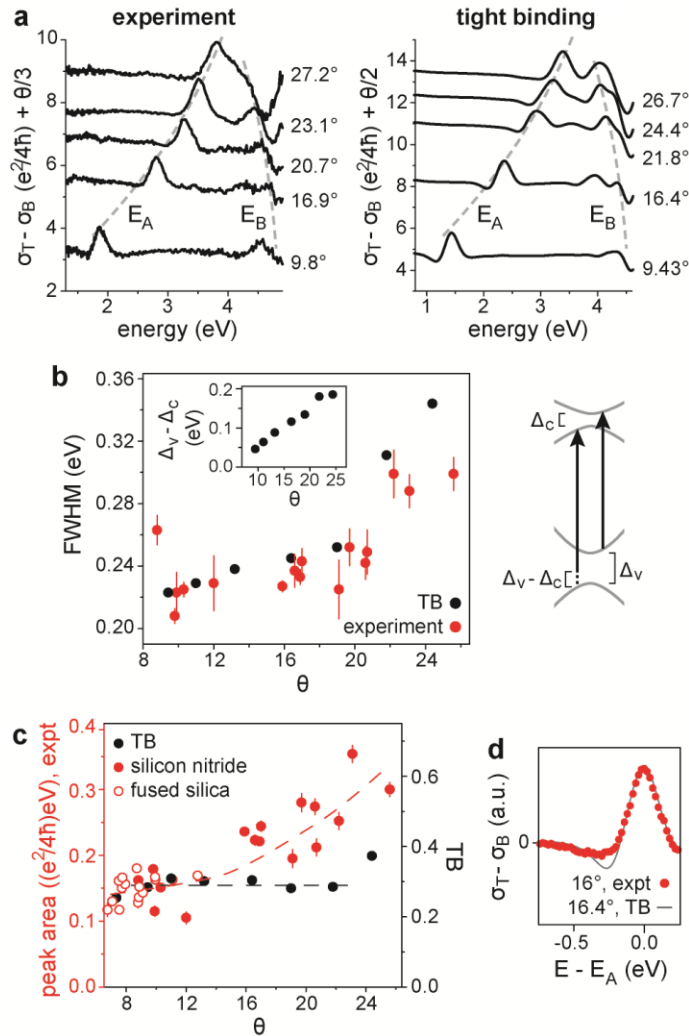


**Figure 6.1: Comparison of experimental data with tight binding calculations**

(a) Experimental and TB (adapted from [1]; see main text)  $\sigma_T - \sigma_B$  spectra at similar angles, with offsets proportional to  $\theta$ . Note different scales in each plot. (b, left) Peak FWHM, which increases with increasing  $\theta$ . (inset) TB calculated  $E_A$  peak splitting as a function of  $\theta$ . (b, right) Schematic showing  $e-h$  asymmetry, which leads to  $E_A$  peak broadening by  $\Delta_V - \Delta_C$ . (c)  $E_A$  peak area, determined by a Gaussian fit, as a function of  $\theta$ . Filled red circles are from spectra shown in Figure 5.15, on silicon nitride substrates, and empty circles are from additional samples on fused silica. Filled black circles are areas calculated from TB spectra (note different scale). Dashed lines are guides to the eye. (d) Calculated  $\sigma_T - \sigma_B$  at  $16.4^\circ$  (line), alongside averaged experimental data (circles). Four spectra within  $2^\circ$  of  $16^\circ$  were averaged as a function of  $E - E_A$ , and the calculations and experimental data were scaled to match in height. [2]

In order to more carefully examine the effects of single particle and many-body optical processes on the optical absorption spectra of tBLG, we now focus on the magnitude and lineshapes of our

$\sigma$  data that we first presented in Chapter 5. In Figure 6.1, we plot a selection of several individual  $\sigma_T - \sigma_B$  spectra from the 2D plot in Figure 5.15 ( $\sigma_T$  and  $\sigma_B$  are the optical conductivities of twisted and Bernal stacked bilayer graphene, respectively, as defined in Chapter 5). We compare these results to recent tight binding (TB) calculations of  $\sigma_T$  at similar commensurate angles [1], after subtracting the calculated  $\sigma_B$  from [1] and broadening the result by Gaussian convolution ( $\sigma_{\text{Gauss}} = 0.11$  eV). The empirical broadening needed to match our data is much larger than our experimental resolution (2 nm, or  $\sim 0.015$  eV at 3 eV), indicating additional thermal and/or inhomogeneous broadening of the optical response in our samples.

The TB calculations capture several features we observe. First, they clearly show the presence of the  $E_A$  and  $E_B$  peaks whose positions and shapes evolve with  $\theta$ . Second, we observe that the  $E_A$  peak broadens as  $\theta$  increases. Figure 6.1b plots the full width at half maximum (FWHM) of a Gaussian fit *vs.*  $\theta$  for all  $\theta < 27^\circ$  (red dots). After adding the empirical broadening discussed above, we find that the TB peak widths also increase with increasing  $\theta$  in a way which is numerically consistent with our data (Figure 6.1b). Our results suggest that the broadening is caused by the band asymmetry between electrons and holes at larger energies, discussed in [1] (Figure 6.1b, right), which originates from a non-zero overlap integral in the tight binding picture of the graphene band structure [5]. Here, electron-hole asymmetry alters the magnitudes of the minigaps near  $I_A$  in the valence ( $\Delta_v$ ) and conduction ( $\Delta_c$ ) bands, splitting the tBLG absorption feature into two peaks with separation  $\Delta_v - \Delta_c$ . This splitting can be observed in the unbroadened TB calculations of  $\sigma$  (see, for example, the  $9.43^\circ$ ,  $11.0^\circ$ , and  $13.2^\circ$  cases in Figure 5.12), and it increases with  $\theta$  up to  $\sim 0.2$  eV near  $25^\circ$  (inset, Figure 6.1b). While this splitting is too small to be observed directly in our data, it instead contributes to peak broadening.

However, the TB results deviate from experiment in several ways. First, there are significant differences between the calculated and observed peak shapes, especially for  $\theta > 20^\circ$ , as can be seen in Figure 6.1a. In particular, the relative weights of the  $E_A$  and  $E_B$  features do not match our results. Second, the relative areas of the  $E_A$  peaks as a function of  $\theta$  are also not well described by the TB calculations. Figure 6.1c shows the integrated area of the  $E_A$  peak, determined by a Gaussian fit. For this plot, we included the  $\sigma$  spectra of 12 additional tBLG domains on fused silica substrates using reflection spectroscopy [6], converting  $E_A$  to  $\theta$  with our empirical formula presented in Chapter 5. Our experimental results show an approximately constant peak area at low angles, followed by an increase at higher angles. On the contrary, the TB calculated area is roughly constant for  $10^\circ < \theta < 20^\circ$ . Finally, we observe a subtle, but significant, difference in the  $E_A$  peak shape between theory and experiment. Figure 6.1d compares the lineshapes of the  $E_A$  peak calculated for  $16.4^\circ$  with the experimental data averaged for samples near  $\theta \sim 16^\circ$ . The dip before the  $E_A$  peak is more pronounced in the TB calculation than it is in our data.

### 6.3 | Excitonic effects

The differences between the calculations in Section 6.2 and our experimental data may be caused by excitonic interactions in tBLG, which were not included in the single particle TB model. Deviations from the single particle prediction of the optical absorption lineshape in other low-dimensional carbon materials, such as single layer graphene [6-8] and metallic single walled nanotubes [9], have been attributed to excitons, which are quasiparticle states created by electron-hole ( $e-h$ ) interactions. Excitonic interactions are enhanced in low-dimensional materials due to increased confinement and reduced screening, such that even metallic systems

(i.e. graphene) exhibit excitonic effects. The strongest signatures of  $e-h$  interactions are often observed near band gaps and vHSs, and these excitons can have binding energies of up to hundreds of meV. For example, the 4.6 eV absorption peak in graphene (see Figure 5.15, and Figure 6.2 below) associated with its saddle point vHS exhibits several features which reflect the presence of excitons. Figure 6.2 shows the experimental optical conductivity of single layer graphene, alongside theoretical predictions using models without (blue line) and with (black dashed line)  $e-h$  interactions included. The model which includes  $e-h$  interactions provides a better fit to both the shape of the peak and the peak energy, which is redshifted by  $\sim 800$  meV from the energy predicted by theory which does not include  $e-h$  interactions [6-8]. Additionally, the asymmetric shape of the peak can be fit to a phenomenological Fano model (green line), where the exciton is treated as a discrete state which is coupled to the continuum of single particle states in the graphene band structure.

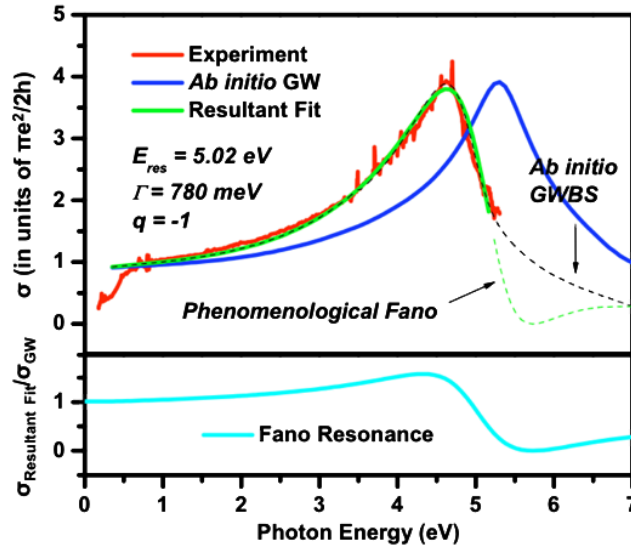


**Figure 6.2: Saddle point exciton in single layer graphene**

Including the effects of excitons, through either an *ab initio* (black dashed line) or phenomenological (green line) model, provides the best fit to the experimental optical conductivity of single layer graphene (red line). [6]

Despite the known effects of excitons on the single layer graphene optical response, little was known about the effects of  $e$ - $h$  interactions on the optical properties of tBLG. To study this further, we computed the optical absorption spectrum of tBLG using first-principles GW-Bethe-Salpeter-Equation (BSE) simulations (similar to those used to calculate the black dashed line in Figure 6.2) [10-13]. Because of the demanding computational requirements of many-body calculations, our first-principles simulations consider two twisted bilayer graphene (tBLG) structures with the smallest commensurate unit cells, whose rotational angles are  $21.8^\circ$  and  $27.8^\circ$ . As the starting point, we use density functional theory (DFT) within the local density approximation (LDA) [7] to perform a structural relaxation, and obtain ground-state eigenvalues and wave functions. The DFT/LDA plane-wave cutoff is set to be 60 Ry. The atomic structures of tBLG are fully relaxed until the force on each atom is below  $0.01 \text{ eV/\AA}$ . Since the degree of coupling between layers depends sensitively on the interlayer distance, we have also employed a van der Waals (vdW) functional [8], which should more accurately describe the interlayer interactions in graphene, to check whether the calculated interlayer distance is affected. Our simulation shows that the vdW-calculated interlayer distance (0.335 nm) is similar to that from DFT/LDA, and that it is not sensitive to the twist angle ( $0.335 \pm 0.002 \text{ nm}$  for  $21.8^\circ$  vs.  $0.336 \pm 0.002 \text{ nm}$  for  $27.8^\circ$ ). However, since the conventional GW-BSE framework is incompatible with the nonlocal vdW functional, we use DFT/LDA for consistency.

The single-shot GW-Bethe-Salpeter equation (BSE) approach is applied to obtain the quasiparticle band structures and optical absorption spectra. The static screening is included by the Alder-Wise form of the polarizability within the random-phase approximation (RPA). It is extended to the dynamical screening calculation for the quasiparticle-energy based on the general plasmon pole model (GPP) [9]. For these plane-wave simulations, the dielectric function is

expanded with a 6-Ry energy cutoff.  $30 \times 30 \times 1$  and  $18 \times 18 \times 1$  k-point grids are employed to calculate the dielectric functions and  $e$ - $h$  interaction kernels of  $21.8^\circ$  and  $27.8^\circ$  tBLG, respectively. Additionally, the finer k-point grids are necessary to obtain the smooth optical absorption spectra of tBLG ( $60 \times 60 \times 1$  for  $21.8^\circ$  and  $36 \times 36 \times 1$  for  $27.8^\circ$ ). Finally,  $e$ - $h$  interactions and optical absorption spectra are obtained by solving the BSE within the Tamm-Dancoff approximation [10]. Slab Coulomb truncation is applied to avoid artificial interactions between quasiparticles of adjacent unit cells [11].

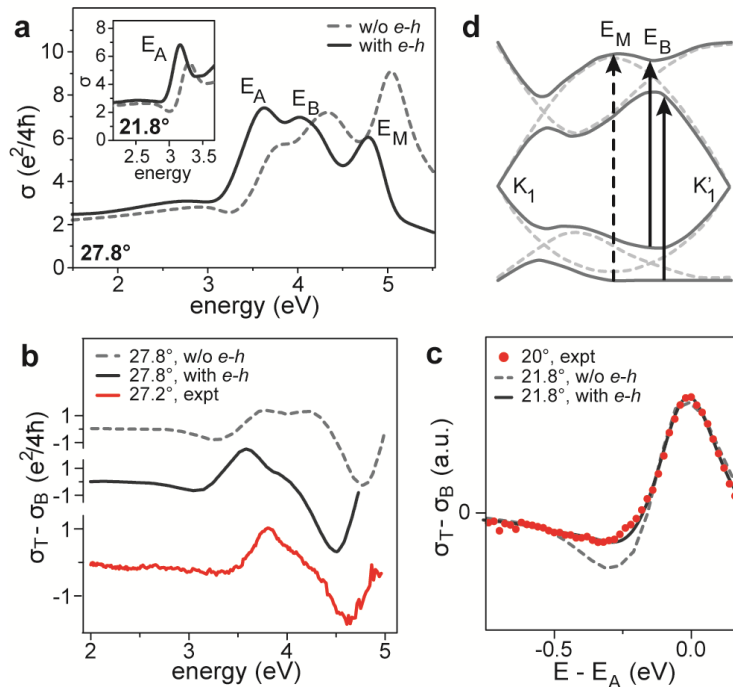


**Figure 6.3: Excitonic effects in tBLG**

(a) Calculated  $\sigma$  spectra of tBLG with and without  $e$ - $h$  interactions included. The  $e$ - $h$  interactions act to redshift the absorption features, and increase the spectral weight of the lower energy peaks while decreasing that of the higher energy peaks. (b) Calculated  $\sigma_T - \sigma_B$  at  $27.8^\circ$  alongside data at  $27.2^\circ$ . The  $e$ - $h$  calculation captures the relative heights of the peaks seen in experiment (note different y scales). (c) Calculated  $\sigma_T - \sigma_B$  at  $21.8^\circ$  (lines), alongside averaged experimental data (circles). (d)  $E_B$  and  $E_M$  optical transitions are overlaid on tBLG band structure without (dashed lines) and with (solid lines) interlayer interactions included. The  $E_M$  transition is weakened because the selection rules for the nearby  $E_B$  transition are different.

To reproduce the optical spectra across the full range of the relevant energies (0 to 6 eV), we must include enough conduction and valence bands (7 bands each for  $21.8^\circ$  and 12 each for  $27.8^\circ$ ). For the optical absorption spectra, we only consider the case of incident light with a polarization parallel to the graphene plane [12].

Our calculations indicate that excitonic effects play an important role in the optical response of tBLG. Figure 6.3a contrasts the calculated tBLG absorption spectra with and without  $e-h$  interactions. The inclusion of  $e-h$  interactions lowers  $E_A$  by  $\sim 200$  meV for both angles because of the reduced screening between quasiparticles. While these shifts are smaller than the exciton binding energy of 600 meV estimated for the saddle-point exciton in single layer graphene [8], they are an order of magnitude larger than those predicted in metallic single walled nanotubes [14,15].

In addition, our GW-BSE calculations reproduce several key experimental features that the TB calculations fail to explain, and suggest that the excitonic effects on the optical absorption spectra of tBLG are qualitatively different from those found in single layer graphene and BLG. First, the spectral weight of the absorption curve redshifts after  $e-h$  interactions are included. The lowest energy  $E_A$  peak experiences the largest enhancement, the  $E_B$  peak is roughly unchanged, and the highest energy peak associated with the M point vHS of single layer graphene ( $E_M$ ) is substantially reduced. This trend differs significantly from what is observed in single layer graphene or BLG, where excitonic effects are less pronounced at lower energies. The difference in tBLG is that the energies of the interlayer vHSs are close to each other for large  $\theta$ . Because of this, their excitonic interaction energy regimes overlap and make it possible for distant interband transitions to contribute optical oscillator strength to lower-energy excitons, such as  $E_A$ . Therefore, the optical absorbance of the lower-energy excitons is enhanced in tBLG. This

behavior is consistent with our data in Figure 6.1c: at higher angles, where the vHSs  $E_A$  and  $E_B$  are the closest in energy, the  $E_A$  peak area is enhanced the most strongly with respect to that predicted by TB calculations.

Moreover, these shifts in spectral weight provide a close match to the experimental lineshape of  $\sigma$  in tBLG. In Figure 6.3b, we plot the calculated  $\sigma_T - \sigma_B$  at  $27.8^\circ$ , with and without  $e-h$  interactions, alongside our data at a similar angle ( $27.2^\circ$ ). The overall shape of the calculated spectrum with  $e-h$  interactions is a much better fit, especially the relative weights of the  $E_A$  and  $E_B$  features. Finally, the  $e-h$  calculation provides a closer match to the  $E_A$  peak shape we observe. Figure 6.3c, comparing the experimental  $E_A$  peak near  $\theta \sim 20^\circ$  to the calculations at  $21.8^\circ$  (similar to Figure 6.1d), shows that the dip below the absorption peak becomes less pronounced after  $e-h$  interactions are included.

So far, we have focused on the two lower energy peaks in the tBLG spectrum,  $E_A$  and  $E_B$ . However, the interlayer vHSs also strongly perturb the peak associated with graphene's intrinsic saddle point vHs, or  $E_M$ . In single layer graphene and BLG, the  $E_M$  peak dominates the optical absorption spectrum (see Figure 5.14), and its exciton-induced red shift is calculated to be  $\sim 600$  meV [8]. However, in tBLG, we find that the excitonic red shift of the  $E_M$  peak is only 210 meV for  $27.8^\circ$  (Figure 6.3a). In addition, the  $E_M$  peak height is calculated to be  $\sim 5e^2/4\hbar$ , about half that found in BLG. Our experimental results in Figure 5.14 qualitatively reproduce the reduced height and blueshift of the  $E_M$  peak at high angles. Further analysis of our calculations shows that the screened Coulomb interactions in BLG and tBLG are not very different. However, we find that the M point optical transition strength is reduced by the  $E_B$  transition. Since the intralayer optical transition at the M point occurs between a different pair of bands than either of the  $E_B$  transitions (Figure 6.3d), these transitions compete when they are close to each other in  $k$ -

space, weakening the M point transition compared to that in BLG. Both the spectral weight redshift discussed above and the weakening of the intralayer transitions at the M point likely cause the reduction of the excitonic effects near the  $E_M$  peak in tBLG.

A few discrepancies remain between our experimental data and both TB and first principles calculations. First, all of the calculated values of the absolute magnitudes of the features in  $\sigma_T - \sigma_B$  are significantly larger than experiment, which can be seen from the different y-axis scales used for the theory results in Figure 6.1 and Figure 6.3. Second, the peak positions calculated with GW-BSE are significantly lower than the experimental results. Both of these discrepancies may reflect overestimated interlayer coupling. The local density approximation (LDA) is the starting point for all of the DFT calculations in this chapter (the TB parameters for tBLG are fit to DFT band structure calculations), and this approximation can overestimate the degree of interlayer hopping in bilayer graphene, resulting in vHSs of a larger magnitude and stronger excitonic effects after the GW-BSE framework is included. While DFT has successfully modeled BLG, there is no guarantee that this technique will accurately capture the weaker interlayer coupling in tBLG. Several additional factors may influence the reduced experimental peak intensity in comparison to the theoretical predictions. Charge inhomogeneities, which are common in 2D materials [16], could reduce the strength of the  $\sigma$  features we measure. Specifically, small potential differences across the layers would shift their valence and conduction band intersections to different locations in  $k$ -space [17], which would reduce the allowed optical transitions between them. Local doping could also modify the many-body contributions to  $\sigma$  by modifying screening. Finally, thermal fluctuations may also affect the tBLG coupling strength [3]. Further studies will be needed to examine each of these effects in more detail.

## 6.4 | Bound excitons in tBLG

Although tBLG provides an interesting example of the importance of excitonic effects in low-dimensional systems, a relevant question is whether the excitons in tBLG are bound or resonant. The excitons in single layer graphene are resonant, meaning that although the interactions between electrons and holes play an important role in the optical response of the material, the eigenstates are spatially delocalized and short-lived. On the other hand, bound excitons are hydrogenic, localized electron-hole pairs with longer lifetimes. Bound excitons have important applications in areas such as photovoltaics, since the long lifetime of the excited carriers can raise the efficiency of these devices. However, due to increased  $e-h$  screening, bound excitons are typically not allowed in metallic systems such as graphene.

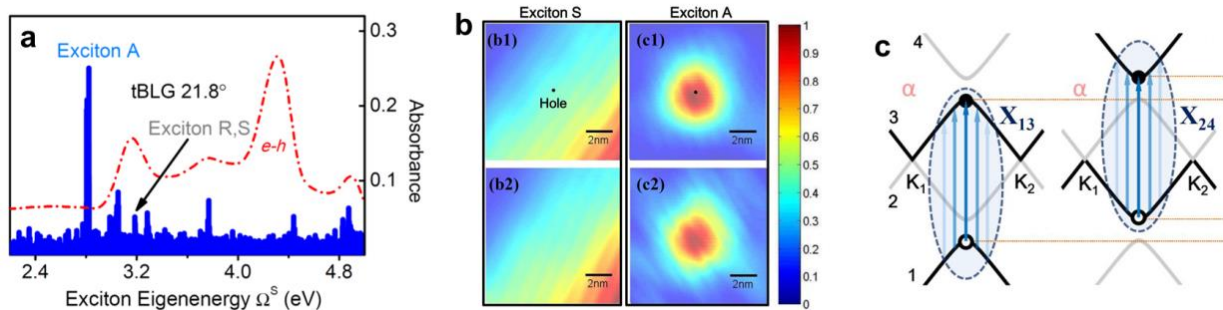


**Figure 6.4: Bound excitons in tBLG**

(a) The binding energies of the excitons in tBLG (blue), plotted alongside the calculated absorption spectrum (red dashed line). Exciton A with a high binding energy is found at an eigenenergy slightly below  $E_A$ . (b) The spatial wavefunctions of a resonant exciton (S) and the bound exciton (A). (c) The two equivalent resonant transitions in tBLG. [18]

In a related preprint to [2], our collaborators calculated the spatial wavefunctions of a number of excitonic states in tBLG [18]. Interestingly, they found that while the excitons associated with the  $E_A$  absorption peak were resonant excitons, an additional bound excitonic state existed at an energy  $\sim 400$  meV lower than the  $E_A$  peak (Figure 6.4). This is surprising given

that the interlayer vHSs in tBLG exist within the continuum of single particle states which are found in gapless single layer graphene. Scattering between the discrete excitonic states and this continuum would normally be expected to shorten the lifetime of the excitons and preclude the formation of bound states.

The key to explaining the existence of a bound state in tBLG is that two independent parallel band transitions are possible, each with almost identical energy (Figure 6.4c). Combined, these two excitations can form an antisymmetric bound state which is resistant to scattering from the continuum states. Such a “Ghost Fano resonance” has also been predicted for the analogous system of two identical electronic quantum dots coupled in parallel to a single continuum [19]. If these calculations are true, it would represent the first time that a bound exciton has been observed in any metallic two- or three-dimensional material.

While the resonant excitons in tBLG are optically bright states, the bound exciton, if it exists, appears to be an optically dark state which cannot be probed directly with linear absorption measurements. However, it may be possible for the optically excited resonant excitons in tBLG to relax into this dark bound state, and the bound state may be accessible with two photon absorption measurements which obey different selection rules. Future time-resolved spectroscopy and two-photon absorption measurements will explore these exciting possibilities in more detail.

## **6.5 | $\theta$ -dependence of Raman scattering of tBLG**

Next, in the following three sections, we will focus on the  $\theta$ -dependent Raman scattering spectrum of tBLG. There are a number of unusual phenomena which occur as a function of  $\theta$ , most notably a strong enhancement of the Raman G band intensity when the tBLG sample is

excited on resonance with  $E_A$ . As in the previous sections, we will compare our data to theory in order to understand this behavior better. However, the work described in these sections also has several practical implications. First, as discussed in Chapter 4, the intensity ratio between the Raman G and 2D peaks was once commonly used as a metric for identifying the number of layers in a graphene sample, with single layer graphene having the highest 2D/G ratio. While this metric is still valid for exfoliated samples, we will show in the following sections that the 2D/G ratio of twisted bilayer samples varies significantly as a function of  $\theta$ , with large  $\theta$  samples having a higher 2D/G ratio than single layer samples. Second, while hyperspectral imaging is a more accurate method to determine  $\theta$  for a tBLG sample, Raman spectroscopy is a more common experimental tool. The results in the following sections have since been used by several experimental groups to estimate  $\theta$  in their tBLG samples [20-22], and these results can be quite precise when the tBLG sample is excited on resonance.

Similar to the techniques discussed in Chapter 5, in which we combined DUV-Vis-NIR hyperspectral imaging with DF-TEM, we have combined widefield Raman imaging with DF-TEM to study the Raman response of tBLG as a function of  $\theta$ . With this, we have imaged over 50 CVD tBLG domains with known twist angles. A representative DF-TEM image, and widefield G and 2D band images ( $E_{\text{ex}} = 2.33$  eV, or  $\lambda_{\text{ex}} = 532$  nm), of one area containing 10 different tBLG domains with varying  $\theta$  is shown in Figure 6.5. The DF-TEM image is a false color composite of the domains mapped individually by diffraction-filtered imaging, as in [23], while the widefield Raman images were acquired in 2 minutes apiece using optical bandpass filters, as in [24]. These images clearly demonstrate that the variations in Raman intensity are strongly correlated with  $\theta$ ; furthermore, the intensity of both Raman bands is nearly constant within a single tBLG domain.

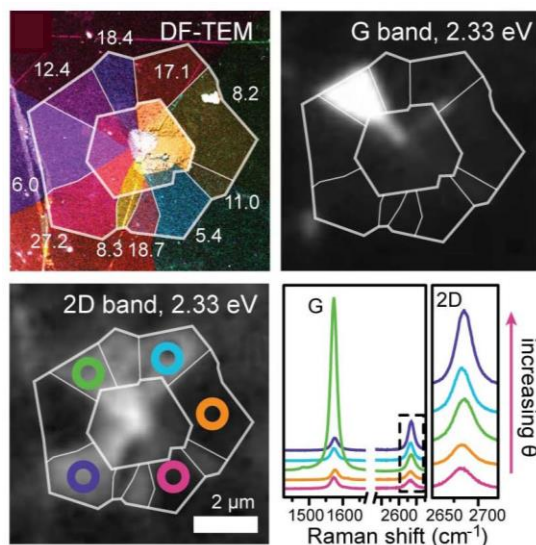


**Figure 6.5: Raman imaging of tBLG**

Dark-field TEM, G band, and 2D band Raman images of the same multilayer tBLG sample. The features in the Raman image correspond well with twisted bilayer domains identified with DF-TEM ( $\theta$  is labeled for each domain in the TEM image). Raman spectra for several domains are also shown.

In particular, there is a strong enhancement of the G band integrated area ( $A_G$ ) for a few specific domains, such as the  $12.4^\circ$  domain in Figure 6.5, while all others show similar  $A_G$  ( $\sim 1.5\times$  that of single layer graphene). We obtain full Raman spectra for each domain (see Figure 6.9), allowing us to detail the quantitative relationship between  $A_G$ ,  $\theta$ , and  $E_{ex}$ . Figure 6.6a shows a plot of  $A_G$  (normalized to  $A_G$  for single layer graphene) vs.  $\theta$ . At  $E_{ex} = 2.33$  eV,  $A_G$  shows a strong, sharp peak at  $\theta_{peak} = 12.5 \pm 0.1^\circ$ . Already, we note that this peak in  $A_G$  appears to be correlated with the  $E_A$  peak in the linear optical absorption of tBLG; for  $\theta = 12.5^\circ$ , we found that  $E_A = 2.27$  eV, which is very close to  $E_{ex}$  in this experiment.

Moreover, if we change  $E_{ex}$ , we find a monotonic relationship between  $E_{ex}$  and  $\theta_{peak}$  which closely matches the  $E_A$  vs.  $\theta$  relationship that we determined at the end of Chapter 5. First, Figure 6.6b shows widefield G band images of the same tBLG area at three different  $E_{ex}$ . For each, a different domain exhibits enhancement, with  $\theta$  later identified with DF-TEM.

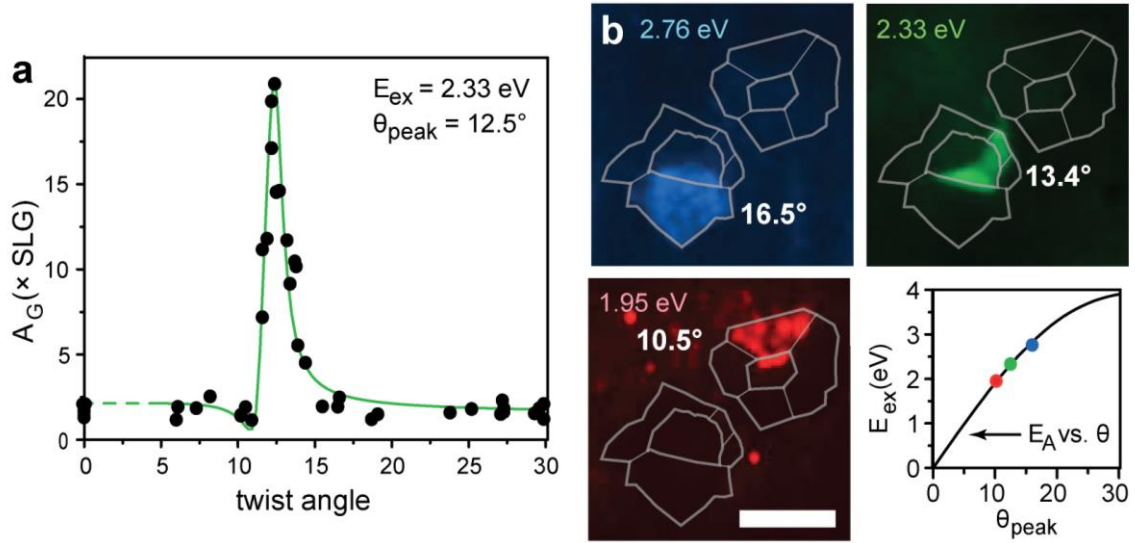


**Figure 6.6: G band enhancement on resonance**

(a) A plot of G band integrated intensity ( $A_G$ ) vs.  $\theta$  across many tBLG samples. Our data form a universal curve with strong enhancement near one specific twist angle. The fit is from a simplified calculation of G band intensity using our parallel band model, as described in Section 6.6. (b) Widefield G band images of the same tBLG regions at three different excitation wavelengths. A different domain exhibits strong G band enhancement in each image (scale bar 5  $\mu\text{m}$ ). Plotted are  $E_{\text{ex}}$  vs.  $\theta_{\text{peak}}$  for each of our available excitation wavelengths alongside a plot of  $E_A$  vs.  $\theta$ .

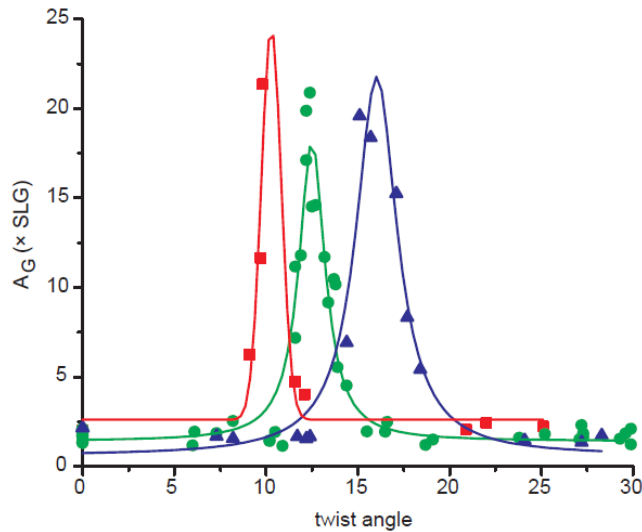


**Figure 6.7: Excitation energy dependent G band resonance**

$A_G$  vs.  $\theta$  for three different excitation energies (red = 1.97 eV, green = 2.33 eV, blue = 2.76 eV). The lines are Lorentzian fits to the data.

Next, we plot our  $A_G$  data for three different  $E_{ex}$  in Figure 6.7. Over 0.8 eV of variation in  $E_{ex}$ , we find that  $\theta_{peak}$  changes by  $\sim 6^\circ$ . We use a Lorentzian fit to estimate the peak position and width, which gives a reasonable estimate for  $\theta_{peak}$  and allows us to quickly compare our three data sets side by side. Because of our limited data at 1.97 eV (red), we were required to impose restrictions on the peak height and width to obtain a physically reasonable fit; whether or not we imposed these restrictions had very little effect on the peak position and error that we obtained. The fits provide the following parameters: 1.97 eV:  $\theta_{peak} = 10.2 \pm 0.3^\circ$ ; 2.33 eV:  $\theta_{peak} = 12.5 \pm 0.1^\circ$ ,  $FWHM = 1.7 \pm 0.2^\circ$ ; and 2.76 eV:  $\theta_{peak} = 16.0 \pm 0.1^\circ$ ,  $FWHM = 2.7 \pm 0.5^\circ$ .

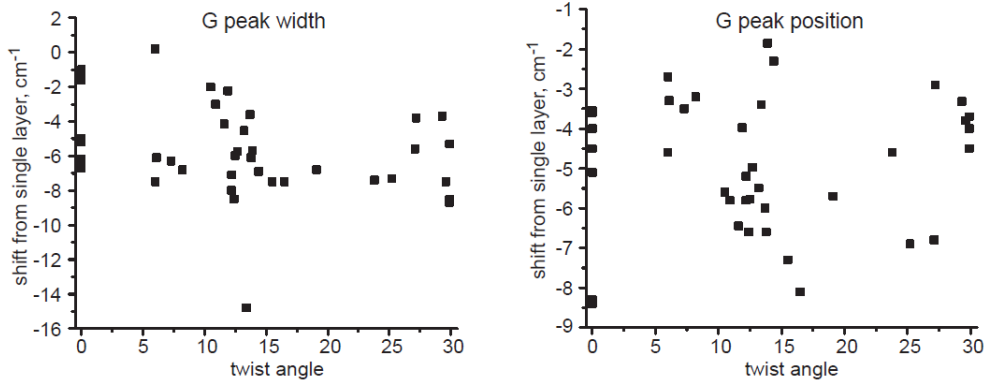


**Figure 6.8: G peak position and width dependence on  $\theta$**

G peak width and position vs. twist angle. We observe a slight decrease in wavenumber, consistent with previous studies [25,26], which has been attributed to reduced charge transfer doping from adsorbates or the substrate in BLG as compared with single layer graphene (SLG). We also observe a narrowing of the G peak of our bilayer graphene as compared to single-layer graphene. We see no clear dependence of either the G peak position or width on twist angle.

Finally, we plot these points in Figure 6.6b alongside our fit for  $E_A$  vs.  $\theta$ , and observe a strong correlation between these two experiments. Using our empirical formula in Chapter 5, we obtain  $E_A$  peak energies of 1.92, 2.27, and 2.74 eV for 10.2, 12.5, and 16.0°, respectively, which are very close to the peak  $A_G$  values obtained with the fits in Figure 6.7. Hence, we conclude that the enhancement of the Raman G peak in tBLG is related to its interlayer vHSSs. However, it is

unusual that the small (~20%) increase in optical absorption in tBLG would correspond to such a large (greater than one order of magnitude) increase in G band intensity. We will discuss the mechanism for this behavior, as well as provide a theoretical fit to our data (green line, Figure 6.6) in Section 6.7.

Our data also unambiguously show that, like the tBLG optical absorption features, the enhancement in  $A_G$  also has a universal, one-to-one correspondence with  $\theta$  for CVD tBLG. While similar behavior was observed by others [4,27], our data provide the first direct and spatially-resolved confirmation of its structural origin.

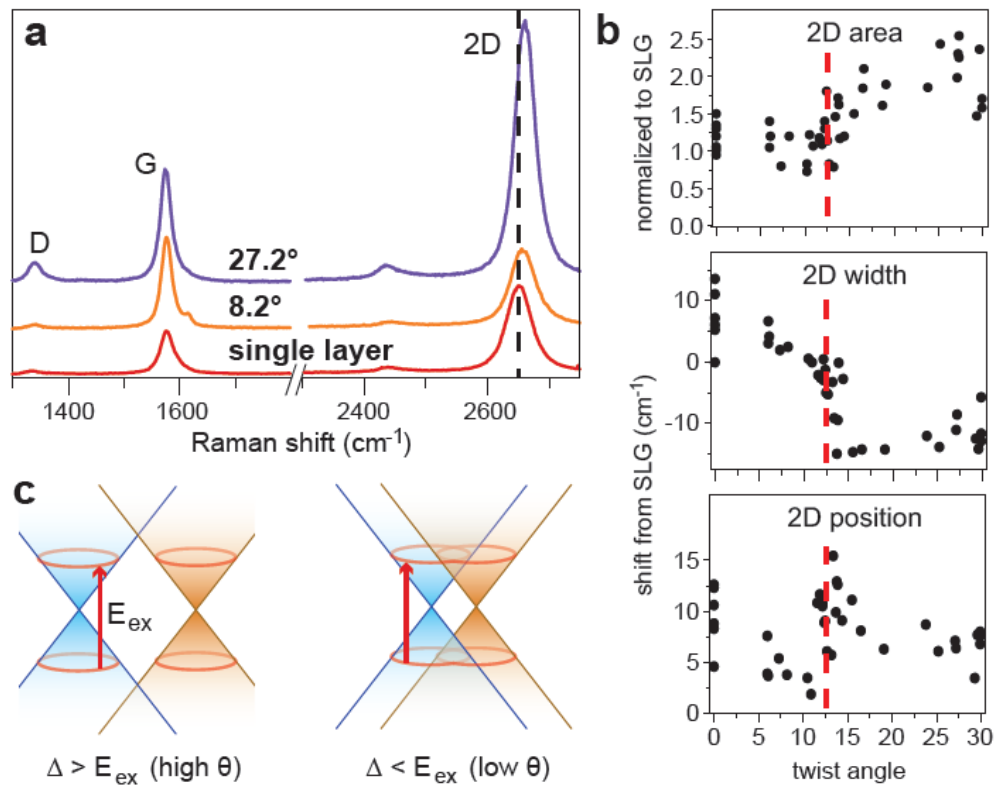


**Figure 6.9: 2D band behavior**

(a) Representative high and low angle Raman spectra, compared with single layer graphene (SLG). (b) Statistics of the 2D peak area, width and position vs.  $\theta$  at  $E_{ex} = 2.33$  eV. The dotted line indicates  $\theta_{peak}$ . (c) A simplified schematic of the band structure difference between high and low angle regimes.

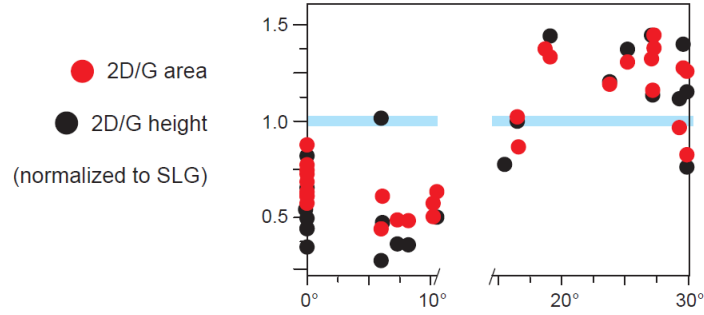


**Figure 6.10: 2D/G ratio**

A plot of the 2D/G height and area ratios vs.  $\theta$  at  $E_{\text{ex}} = 2.33$  eV

The width and position of the G peak show little dependence on  $\theta$  (Figure 6.8). However, the intensity, width, and position of the 2D Raman band, shown in Figure 6.9, show a variety of interesting  $\theta$ -dependent properties. These data are consistent with other results published concurrently by Kim *et al.* [4], except that  $\theta_{\text{peak}}$  is shifted due to the difference in excitation energy. Briefly, although no strong enhancement is present, the 2D band shows distinct behavior at high ( $E_A > E_{\text{ex}}$ ) and low ( $E_A < E_{\text{ex}}$ ) twist angles. We show representative Raman spectra for each case (Figure 6.9a), as well as 2D band statistics over many samples (Figure 6.9b). The Raman spectrum is similar to that of single layer graphene at high twist angles, but the integrated intensity of the 2D band is roughly twice that of single layer graphene. We expect that the Dirac cones of each layer are well-separated on a scale of  $E_{\text{ex}}$  in this angle regime (Figure 6.9c), but with twice as many pathways available for the 2D band process. At low twist angles, however, the integrated intensity of the 2D peak is almost identical to that of single-layer graphene, and the peak broadens compared to the high-angle case. Now, the Dirac cones from each layer overlap, and cannot be treated individually; more detailed Raman calculations have been performed by Kim *et al.* [4], and explain this behavior well. The 2D peak intensity, width, and position all change rapidly near  $\theta_{\text{peak}}$ , the transition between these two regimes. As in the case of the G band enhancement, we find that the 2D band behavior is well parameterized by  $\theta$ .

The 2D/G ratio is commonly used as a metric to distinguish single layer and multi-layer graphene, and it was typically assumed that the 2D/G ratio of single layer graphene is larger than that of all multi-layer graphene of any twist angle. We find that although the 2D/G ratio of tBLG is consistently lower than that of single layer graphene for low angles ( $<10^\circ$ ), it is consistently *higher* than single layer graphene between  $\sim 18$ - $27^\circ$ . Although we find that the absolute value of the 2D/G ratio may vary between different samples and substrates, this trend appears to be very consistent. Similar behavior can also be seen in Raman spectra obtained by others [28], although the increase in 2D/G ratio and its angle dependence was not discussed explicitly in that work.

### 6.6 | Mechanism for G band enhancement

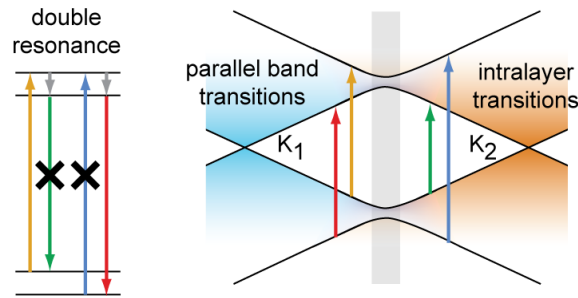


**Figure 6.11: Double resonance Raman enhancement**

Potential double resonance processes in tBLG (left), which would occur between hybridized interlayer states. The colored arrows correspond to the optical transitions shown in the tBLG band structure (right). Each possible double resonance process contains an optical transition which is not allowed in the region where the bands hybridize (x).

In contrast to the small increase in absorption, the G band enhancement is much stronger on resonance in tBLG. A “double resonance” mechanism, described below, was previously proposed to explain this enhancement in certain tBLG samples [27]. The minigap ( $\Delta$ ) in tBLG is, by coincidence, approximately the same energy as the G band phonon,  $\sim 0.2$  eV. Because of this, a double resonance process can potentially occur, where all three energy levels involved in the Raman scattering process correspond to real electronic states (Figure 6.11). In contrast, a

maximum of two energy levels involved in the G band Raman process may correspond to real electronic states in single layer graphene. Thus, a double resonance process would enhance the G band intensity compared to that of single layer graphene.

However, in light of the optical selection rules discussed in Chapter 5, it seems unlikely that this mechanism is correct. For both possible double resonance processes in tBLG, one of the optical transitions is forbidden (Figure 6.11). Instead, we find that the substantial increase in G band intensity for tBLG on resonance is due to quantum interference effects particular to resonance Raman scattering [29,30]. In general, every possible Raman pathway has a phase, which has a different polarity depending on whether the excitation energy is above or below the energy difference between the electronic states in the resonant Raman transition; for a system with many available states, these pathways can interfere constructively or destructively. In single-layer graphene, for example, many pathways interfere destructively due to the linear JDOS, weakening the overall intensity [29,30]. Near the parallel band singularity in tBLG, on the other hand, many states with the same energy difference can add constructively, leading to a considerable G band enhancement at  $E_{ex} \sim E_A$ .

To verify the significance of these effects, we include all possible transitions in a simplified expression for the Raman intensity in tBLG with varying  $\theta$ . The G band intensity is given by:

$$I \propto \left| \sum_k \frac{|M_{op}|^2 M_{el-ph}}{(E_{ex} - E_{ab} - i\gamma)(E_{ex} - E_{ph} - E_{ab} - i\gamma)} \right|^2$$

where  $M_{el-ph}$  is the electron-phonon coupling matrix element,  $\gamma$  is the inelastic scattering rate (we use  $\gamma = 0.1$  eV, which is reasonable for a sample with some doping/defects present [31]),  $E_{ph} = 0.196$  eV is the G band phonon energy, and  $a$  and  $b$  are electronic states [32]. As our theoretical

fit (green line) in Figure 6.6, we plot a simplified version of this expression which captures the effect of the interference between the various pathways ( $k$ ) available in the electronic band structure. We ignore  $M_{\text{el-ph}}$ , assuming that most of the Raman enhancement we see is due to the band structure alone. We use a phenomenological Lorentzian to model the  $k$ -space dependence of  $M_{\text{op}}$  along the line which passes through  $K_1$  and  $K_2$ , and assume no  $k$ -space dependence in the orthogonal direction.

For the tBLG band structure, we use a simplified four band model presented in [33] (Eqs. 6-9). This model is not intended to be accurate at high twist angles, but it is analytically tractable and contains the qualitative features we desire – two Dirac cones, one for each layer, which exhibit splitting where they intersect. We initially set the splitting  $\Delta = 0.20$  eV, which is consistent with the value we obtained in the commensurate tight binding calculations discussed in Chapter 5.

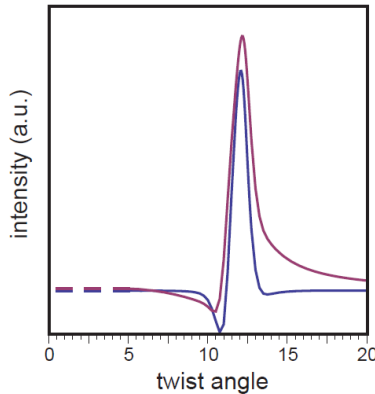


**Figure 6.12: Simplified calculation of G band intensity**

Calculation of simplified G band intensity without (blue) and with (purple) double resonance terms, using  $t$ ,  $M_{\text{op}}$  determined from tight binding calculations.

In addition to parallel band transitions, we can include double resonance terms. We argue above that the double resonance process should be relatively weak; however, since enhancement

due to double resonance should also occur at an energy near  $E_A$ , the two models are difficult to differentiate without further calculation. For double resonance terms, the initial state involved in the emission process (the second term in the denominator of the Raman scattering equation) is different than the final state of the absorption process. We weigh these terms by a factor  $|M_{op}|^2 = (|M_{intra}|^2 |M_{parallel}|^2)^{1/2}$ .

We fit the  $\theta_{peak}$  of our curve to our data by varying  $v_F$ , the Fermi velocity, which defines the slope of the Dirac cones. We achieve the best fit for  $v_F = 0.93 \times 10^6$  m/sec, which is slightly less than that of single-layer graphene ( $\sim 10^6$  m/sec). This is reasonable because it corrects for the slight sublinearity in the band structure of graphene at this energy scale.

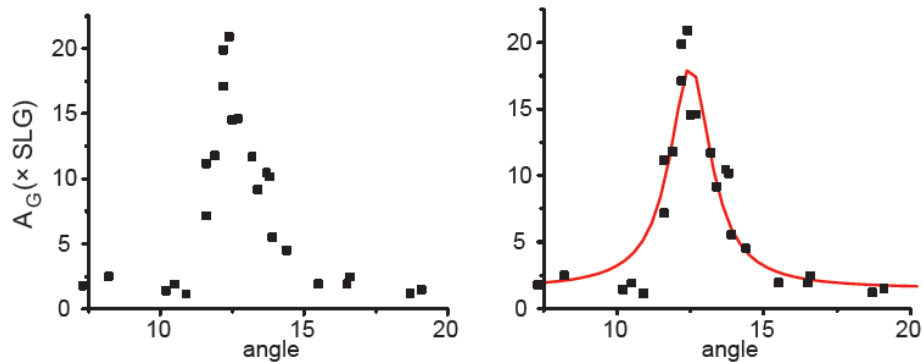


**Figure 6.13: Asymmetry in our  $A_G$  vs.  $\theta$  data**

(left) Our data of G peak intensity vs. twist angle, plotted between 7.5 and 20 degrees, and (right) the same data with a phenomenological Lorentzian fit. While the right half of the data is well fitted to a Lorentzian, the left half is sharper, exhibiting similar asymmetry to our calculated curve.

Our results are shown in Figure 6.12. Including only parallel band and intralayer transitions, we obtain an enhancement of almost an order of magnitude at  $\theta_{peak}$ . Adding double resonance terms has almost no effect on the peak height, but adds an asymmetric tail to the high angle side of the curve. The G band enhancement on the low angle half of the curve falls off more steeply as  $\theta$  decreases, as a result of interference effects between states which become

available when  $E_{\text{ex}}$  is slightly larger than  $E_{\text{A}}$ . The asymmetry in our theoretical calculation of G band intensity is not a reflection of the asymmetry of the singularity in the JDOS, and in fact has the opposite weight than what one would expect from considering the JDOS alone. Our data also appears to exhibit this asymmetry (Figure 6.13); however, more detailed studies are required to confirm the experimental and theoretical peak shape.

Our Raman calculation shows that interference effects can strongly enhance the G band signal, and that parallel band transitions cause most of this enhancement. The peak height is particularly sensitive to the degree of coupling between layers and  $\gamma$ . The fit in Figure 6.6 was obtained both by setting  $\gamma = 75$  meV, and by multiplying the interlayer coupling parameters ( $\Delta$  and the width of the Lorentzian used to model  $M_{\text{op}}$ ) by  $1.2\times$  their calculated values – these modest adjustments create a reasonably good fit. However, our Raman calculation is not fully accurate, because we ignored  $M_{\text{el-ph}}$ ; additionally, our calculations of the band structure,  $t$  and  $M_{\text{op}}$  are not derived from an exact description of our experimental system, as discussed in Chapter 5.

## 6.7 | Applications

Finally, while  $\theta_{\text{peak}}$  only depends on  $E_{\text{ex}}$ , the magnitude of the G band enhancement and variations in 2D behavior are sensitive to the degree of interaction between layers. Thus, Raman imaging provides us with a tool to study tBLG materials in different interaction regimes on a large scale. To demonstrate this, we examine two extreme cases: CVD-grown tBLG, which is fully in contact, and two single layer graphene layers transferred on top of each other, which are in very loose contact and separated by debris.

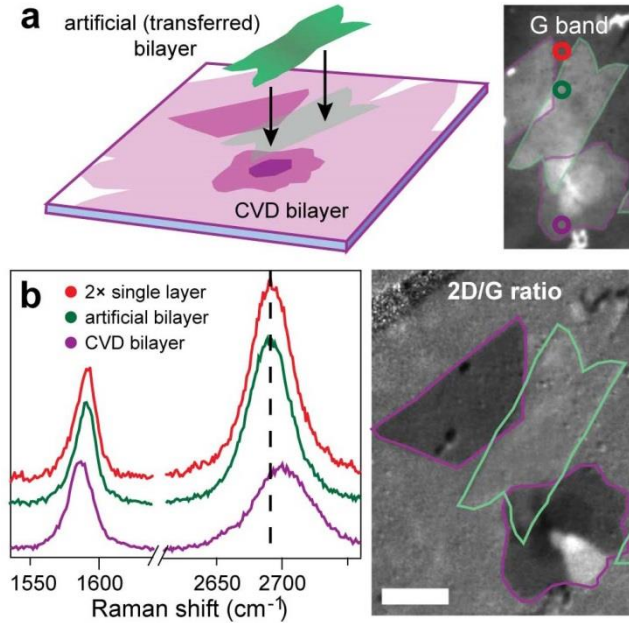


**Figure 6.14: Raman imaging of interlayer coupling in tBLG**

(a) Schematic of our sample and G band image showing CVD and artificial bilayer regions. (b) Raman spectra of artificial and CVD bilayer. The artificial bilayer has weak interlayer coupling, and its Raman signature is almost identically  $2\times$  nearby SLG. Consistent with the spectra, the artificial region disappears in a 2D/G ratio image (scale bar  $5\ \mu\text{m}$ ).

Figure 6.14 shows a schematic of our sample; the artificial tBLG layers are separated by 1-2 nm, as confirmed by atomic force microscopy (Figure 6.15). The Raman spectrum of the artificial tBLG is markedly different from that of a nearby CVD bilayer region (as grown) and is almost identically twice that of single layer graphene (Figure 6.14b). Additionally, in a 2D/G ratio widefield image, the CVD bilayer graphene varies in contrast (2D/G is either higher or lower than single layer graphene, depending on  $\theta$ ), but the entire artificial region cannot be distinguished from the 2D/G ratio of single layer graphene, indicating that the as-transferred layers do not interact and are completely decoupled.

Our findings are confirmed by AFM images of the same region, allowing us to attribute the differences in coupling to differences in interlayer spacing. The artificial bilayer graphene is easily distinguished from the CVD bilayer in AFM. Height measurements indicate an increased

height (1-2 nm) overall from single layer graphene, as well as additional wrinkles and perhaps pockets of debris trapped between the layers. This is in contrast to the CVD bilayer, which is difficult to distinguish from single layer graphene, and has a nominal height of  $\sim 0.6$  nm from the single layer region.

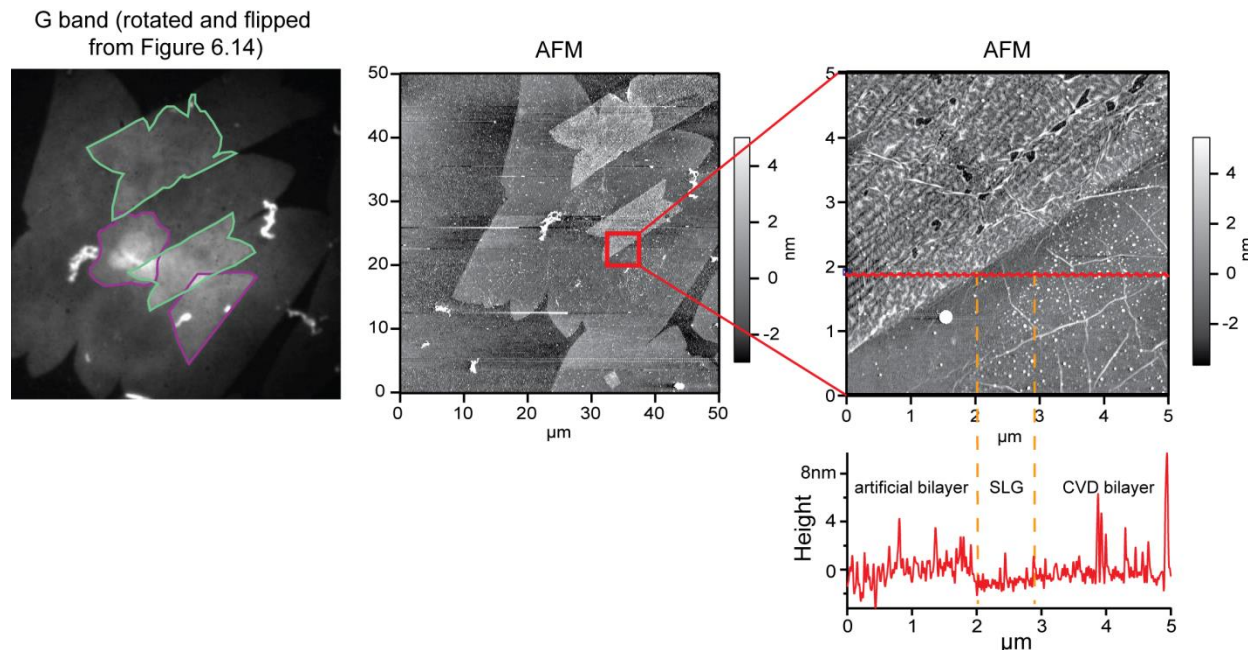


**Figure 6.15: AFM of artificially transferred bilayer graphene**

AFM images and a line scan of the region of the sample shown in Figure 6.14. We focus on a region that contains both artificial (green) and CVD (purple) bilayer.

While we illustrated two extreme examples here, more recent work has established better techniques for coupling artificially stacked layers of 2D materials. We will discuss artificially stacked vertical heterostructures briefly in Chapter 7. However, it is still unknown whether there are quantitative differences in the coupling between artificially stacked graphene layers and CVD tBLG, and the high sensitivity of Raman spectroscopy to the degree of coupling in stacked graphene layers will enable us to probe this question in future studies.

## 6.8 | Conclusion

In this chapter, we have explored a variety of interesting many-body phenomena in tBLG, and our data and analysis indicate that other exciting experimental results, such as the potential existence of bound excitons in tBLG, may be on the horizon. At the beginning of Chapter 7, we discuss our preliminary work on one additional experiment: the optical response of tBLG under the influence of doping and applied vertical electric field.

However, a broader implication of our work is the extreme versatility of the characterization tools we developed in Chapters 3 and 4. While tBLG is abundant in CVD graphene, new tools were required to study the complex, spatially varying structural and optical properties of these samples. Once we developed these tools, they immediately enabled the discovery of many new phenomena in tBLG. Since our work began, the family of heterogeneous 2D materials has grown rapidly, and we expect that our techniques will also be extremely useful for future studies of 2D systems such as transition metal dichalcogenides (TMDs) and artificially stacked vertical heterostructures. We will discuss some of these possibilities in the second half of Chapter 7.

## References

- [1] P. Moon and M. Koshino, *Physical Review B* **87**, 205404 (2013).
- [2] R. W. Havener, Y. Liang, L. Brown, L. Yang, and J. Park, *Nano Letters* **14**, 3353 (2014).
- [3] R. Havener, H. Zhuang, L. Brown, R. Hennig, and J. Park, *Nano Letters* **12**, 3162 (2012).
- [4] K. Kim *et al.*, *Physical Review Letters* **108**, 246103 (2012).
- [5] R. Saito, G. Dresselhaus, and M. S. Dresselhaus, *Physical Properties of Carbon Nanotubes* (Imperial College Press, 1998).
- [6] K. Mak, J. Shan, and T. Heinz, *Physical Review Letters* **106**, 046401 (2011).
- [7] D. Chae, T. Utikal, S. Weisenburger, H. Giessen, K. von Klitzing, M. Lippitz, and J. Smet, *Nano Letters* **11**, 1379 (2011).
- [8] L. Yang, J. Deslippe, C. Park, M. Cohen, and S. Louie, *Physical Review Letters* **103**, 186802 (2009).
- [9] F. Wang, D. Cho, B. Kessler, J. Deslippe, P. Schuck, S. Louie, A. Zettl, T. Heinz, and Y. Shen, *Physical Review Letters* **99**, 227401 (2007).
- [10] W. Kohn and L. Sham, *Physical Review* **140**, A1133 (1965).
- [11] M. Hybertsen and S. Louie, *Physical Review B* **34**, 5390 (1986).
- [12] M. Rohlfing and S. Louie, *Physical Review B* **62**, 4927 (2000).
- [13] J. Deslippe, G. Samsonidze, D. Strubbe, M. Jain, M. Cohen, and S. Louie, *Computer Physics Communications* **183**, 1269 (2012).
- [14] C. D. Spataru, S. Ismail-Beigi, L. X. Benedict, and S. G. Louie, *Physical Review Letters* **92**, 077402 (2004).
- [15] J. Deslippe, C. Spataru, D. Prendergast, and S. Louie, *Nano Letters* **7**, 1626 (2007).
- [16] J. Martin, N. Akerman, G. Ulbricht, T. Lohmann, J. H. Smet, K. Von Klitzing, and A. Yacoby, *Nature Physics* **4**, 144 (2008).
- [17] J. dos Santos, N. Peres, and A. Castro, *Physical Review Letters* **99**, 256802 (2007).
- [18] Y. Liang, R. Soklaski, S. Huang, M. W. Graham, R. W. Havener, J. Park, and L. Yang, *arXiv*, arXiv:1401.6663 (2014).
- [19] M. L. L. de Guevara, F. Claro, and P. A. Orellana, *Physical Review B* **67**, 195335 (2003).
- [20] J. T. Robinson, S. W. Schmucker, C. B. Diaconescu, J. P. Long, J. C. Culbertson, T. Ohta, A. L. Friedman, and T. E. Beechem, *ACS Nano* **7**, 637 (2012).
- [21] Y. Kim *et al.*, *Physical Review Letters* **110**, 096602 (2013).

- [22] T. Beechem, T. Ohta, B. Diaconescu, and J. Robinson, *ACS Nano* **8**, 1655 (2014).
- [23] P. Huang *et al.*, *Nature* **469**, 389 (2011).
- [24] R. W. Havener, S.-Y. Ju, L. Brown, Z. Wang, M. Wojcik, C. S. Ruiz-Vargas, and J. Park, *ACS Nano* **6**, 373 (2012).
- [25] S. Berciaud, S. Ryu, L. Brus, and T. Heinz, *Nano Letters* **9**, 346 (2009).
- [26] P. Poncharal, A. Ayari, T. Michel, and J. L. Sauvajol, *Physical Review B* **78**, 4 (2008).
- [27] Z. Ni, L. Liu, Y. Wang, Z. Zheng, L. Li, T. Yu, and Z. Shen, *Physical Review B* **80**, 125404 (2009).
- [28] Z. Ni, Y. Wang, T. Yu, Y. You, and Z. Shen, *Physical Review B* **77**, 235403 (2008).
- [29] C. Chen *et al.*, *Nature* **471**, 617 (2011).
- [30] D. Basko, *New Journal of Physics* **11**, 095011 (2009).
- [31] C. Casiraghi, *Physica Status Solidi B-Basic Solid State Physics* **248**, 2593 (2011).
- [32] M. Cardona, *Light Scattering in Solids I* (Springer, 1982).
- [33] R. de Gail, M. Goerbig, F. Guinea, G. Montambaux, and A. Neto, *Physical Review B* **84**, 045436 (2011).

## Chapter 7 : FUTURE DIRECTIONS

### 7.1 | Introduction

To conclude our work, we discuss two potential future directions of the research presented in this dissertation. First, in the preceding chapters, we demonstrated all-optical structural characterization of a number of 2D heterostructures, such as tBLG and graphene/*h*-BN junctions, on substrates which would also enable the fabrication of electronic devices using standard photolithography techniques. We are now in a position to take advantage of these unique capabilities. In this chapter, we present a preliminary study of the optical properties of tBLG as a function of electrical gating. For this, we have fabricated transparent, dual gated tBLG field effect transistors in which the optical and electronic properties of the tBLG can be monitored simultaneously. This device geometry has the potential to provide a number of new insights into the properties of tBLG and other stacked 2D materials.

Second, while our previous work focused on the optical characterization of graphene and *h*-BN, the tools we have developed are extremely versatile. We will discuss some potential applications of our techniques for studying two new classes of heterogeneous 2D materials: semiconducting transition metal dichalcogenides (TMDs), and artificial vertical stacks of 2D materials. The large scale production of both of these systems was only achieved very recently, and many of their properties and potential applications are still unknown. Lastly, we will summarize our work in its entirety.

## 7.2 | Optical properties of tBLG vs. doping and vertical field

Our work in Chapters 5 and 6 focused on the intrinsic optical properties of tBLG. However, the addition of electronic gating could provide further insights into the band structure and optical response of tBLG, and increase the tunability of the system. There are two different mechanisms by which gating could affect the optical response of tBLG. First, gating could be used to dope the material (Figure 7.1, left), altering its total free carrier density. In a single particle picture, doping alone would have no effect on the optical properties of tBLG, since the Fermi energy ( $E_F$ ) which can be achieved with a standard gate (hundreds of meV) is much smaller than the optical excitation energy used in our studies. However, changing the free carrier density could alter  $e$ - $h$  and electron-electron ( $e$ - $e$ ) screening, affecting the strength of many-body processes. Second, applying a vertical field to tBLG would shift the relative potentials of each layer (Figure 7.1, right). A vertical field would affect the optical response of tBLG even in a single particle picture, causing the interlayer vHSs to shift away from each other in momentum space [1] and reducing the allowed optical transitions between them.

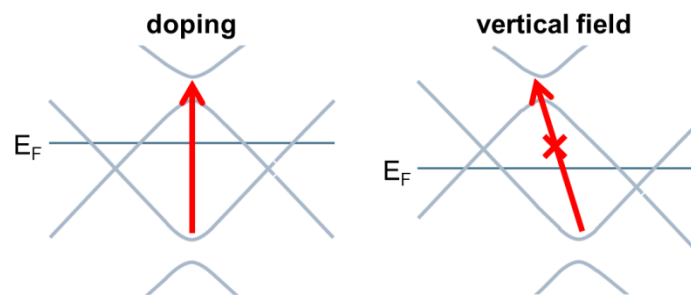


**Figure 7.1: Doping and vertical field in tBLG**

Schematics showing the effects of doping and vertical field in tBLG. For the doping case, the Fermi energy ( $E_F$ ) of both layers changes with respect to their Dirac points, increasing the total free carrier density. This does not affect the optical transitions (red arrow) in the single particle picture. For the field case, there is a relative potential difference between the two layers. The interlayer vHSs are now separated in momentum space and direct optical transitions cannot occur between them due to conservation of momentum.

Independently controlling the doping level and vertical field in tBLG requires two independent gates, one on either side of the graphene. However, fabricating a dual gated device in which the tBLG can still be probed optically is challenging, because standard metal gates are typically opaque. Here, we discuss our preliminary efforts in this area.

We have fabricated dual gated tBLG field effect transistors on a fused silica substrate, in which the metallic top and back gates are very thin ( $\sim 10$  nm) and optically transparent. Figure 7.2a shows a white light optical transmission image of a typical device. Although the active region is more opaque than the fused silica substrate, it is transparent enough for transmission spectroscopy at energies of up to  $\sim 4$  eV. The tBLG is also contacted by two electrodes (labeled S and D) so that the resistance of the device can be monitored as a function of both gate voltages ( $V_t$  and  $V_b$ ).

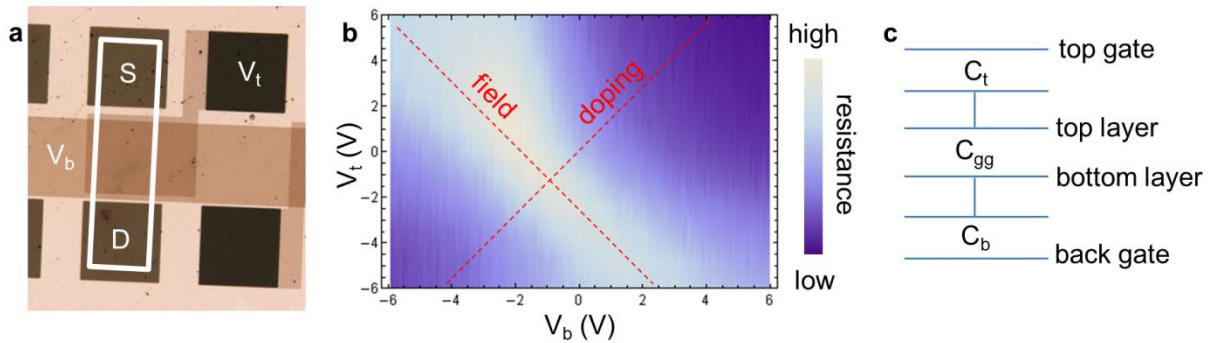


**Figure 7.2: Transparent, dual gated tBLG transistor**

(a) A transmission image of a transparent dual gate device. The graphene (outlined by the white rectangle) is contacted by two electrodes and gated with both a top and a back gate. The square pads (labeled S, D,  $V_t$ ) are  $100 \times 100 \mu\text{m}$ . (b) Typical device resistance as a function of  $V_t$  and  $V_b$ . The “field” and “doping” lines discussed in the text are labeled with red lines. (c) A simplified model of the device, used to convert  $V_t$  and  $V_b$  to carrier density or potential in each layer.

A typical 2D plot of the device resistance vs.  $V_t$  and  $V_b$  is shown in Figure 7.2b. The highest device resistance corresponds to the case when  $E_F$  is located at the Dirac point of both

layers, and the free carrier density is the lowest. This point occurs at a finite applied  $V_t$  and  $V_b$  due to intrinsic doping in the device, typically caused by charged impurities trapped between the gate dielectric material and the graphene. Increasing or decreasing both  $V_t$  and  $V_b$  together increases the total free carrier density, and the resistance drops quickly. Increasing  $V_t$  while decreasing  $V_b$ , or vice versa, is used to apply a vertical field. Here, the device resistance also decreases slightly due to the finite carrier density in each layer (see Figure 7.1) [2]. The 2D plot of device resistance can be used to monitor the actual doping level and vertical field in the device as the gate voltages are adjusted. We use this data to define “doping” and “field” lines: combinations of  $V_t$  and  $V_b$  where the interlayer potential and net carrier density, respectively, are zero.

We can convert our applied gate voltages (V) to doping ( $E_F$ , eV) and vertical field ( $\Delta\mu$ , eV) by modeling the device as a series of capacitors. A simplified version of this model is shown in Figure 7.2c. For our particular device geometry, the most significant terms are the capacitances of each gate and interlayer capacitance of tBLG ( $C_{gg}$ ), determined in a previous experimental study to be  $6.8 \mu\text{F}/\text{cm}^2$  [2]. There is currently significant experimental uncertainty (roughly a factor of 2) in the dielectric constants of our top and back gate dielectric materials, which limits the accuracy of this conversion. Finally, we can also convert the potentials of each layer to a total or net free carrier density using the known band structure of graphene.

While we sweep  $V_t$  and  $V_b$  and monitor the resistance of the tBLG device, we simultaneously measure its transmission spectrum. Here, we focus on the effects of doping and vertical field on the  $E_A$  peak of a single tBLG domain with  $\theta = 11.5^\circ$ , or  $E_A = 2.1$  eV. Figure 7.3 shows the variations of the  $E_A$  peak along the doping and field lines. Already, it is clear that both doping and field each have a different effect on the  $E_A$  peak in tBLG.

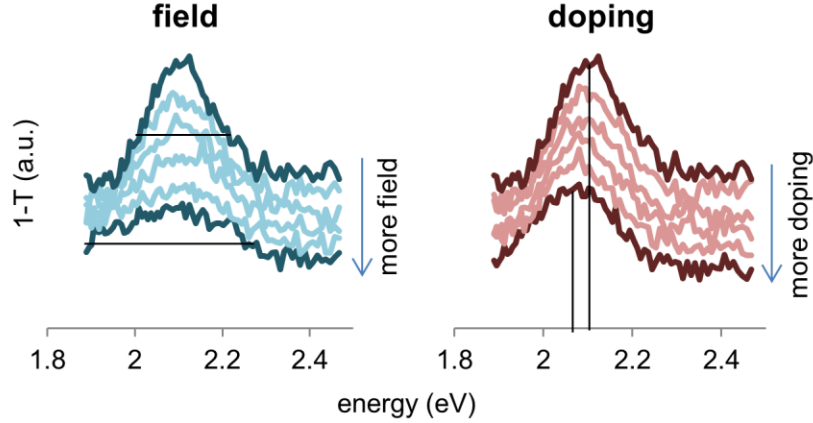


**Figure 7.3: Field and doping effects on the  $E_A$  peak**

Plots of  $1-T$  vs. energy for the  $E_A$  peak in  $11.5^\circ$  tBLG, showing the evolution of the peak with increasing field and doping. The plots are offset for clarity.

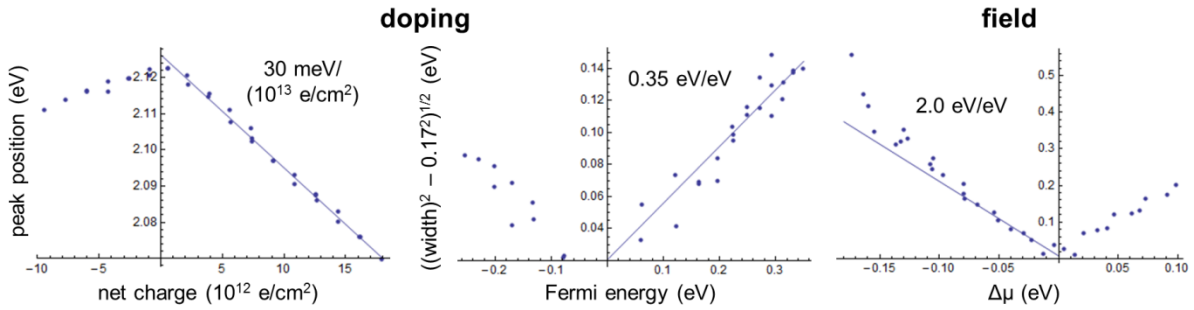


**Figure 7.4: Doping and field dependence of  $E_A$  peak parameters**

Doping dependence of  $E_A$  peak position (left) and broadening (center), and field dependence of  $E_A$  peak broadening (right). The slope of a linear fit is provided for all three plots.

To quantify this behavior, we fit the  $E_A$  peaks to Gaussians in order to extract a quantitative peak area, width, and position as a function of doping and field; some results from these fits are shown in Figure 7.4. For the doping case, the most significant effect is a redshift in the  $E_A$  peak energy with increasing carrier density. As discussed above, any changes in the  $E_A$  peak as a function of doping alone are due to many-body effects. Similar doping effects have been observed in the optical spectra of single walled carbon nanotubes [3] and single layer graphene [4]. In both cases, increased carrier density increases both  $e-e$  and  $e-h$  screening, with

the net effect being a slight redshift in the optical resonances. We find that the magnitude of the redshift in  $E_A$  that we observe as a function of carrier density is similar to that observed for the saddle point vHS in single layer graphene [4]. In addition, we also observe a slight broadening of the  $E_A$  peak with increased doping, corresponding to a decrease in the excited carrier lifetime when more free carriers are present. Together, these observations strengthen our previous findings of the importance of many-body effects on the optical processes in tBLG.

For the field case, the peak broadens substantially. We find that the field induced broadening is approximately linear as a function of field for small fields, assuming an intrinsic peak width of 0.17 eV and a total width of  $((\text{field induced broadening})^2 + 0.17^2)^{1/2}$ . We note that our extracted intrinsic peak width is significantly smaller than the  $E_A$  peak widths that we observed in Chapter 6 ( $\sim 0.22$  eV for similar  $\theta$ ) [5], indicating that a small amount of doping and/or vertical field was present in our previous samples. We are now working to understand the field data quantitatively using the single particle model presented in Figure 7.1.

Although preliminary, our current results are very promising. Future efforts in this area will include the more controlled fabrication of higher quality electronic devices, and we will study the effects of doping and field on additional tBLG devices with a range of  $\theta$ . The device geometry presented in this section will also be useful for studying the optoelectronic properties of other stacked 2D materials, including the examples which will be presented in the following sections.

### **7.3 | MoS<sub>2</sub> and related transition metal dichalcogenides**

We next discuss two new classes of materials which will be interesting subjects to study using the techniques we have developed in this dissertation. In this section, we will explore MoS<sub>2</sub> and

other similar transition metal dichalcogenides (TMDs). As introduced in Chapter 1, MoS<sub>2</sub> is an atomically thin semiconductor. Novel optical properties were previously discovered in few-layer MoS<sub>2</sub> samples produced by mechanical exfoliation: monolayer MoS<sub>2</sub> is a direct band gap semiconductor with significant photoluminescence intensity near ~1.9 eV, while multilayer MoS<sub>2</sub> has an indirect band gap [6]. Soon after, it was found that a number of other related TMDs, including MoSe<sub>2</sub> [7], WS<sub>2</sub>, and WSe<sub>2</sub> [8], exhibit similar behavior as a function of layer number, although the magnitudes of the direct and indirect gaps in these materials depend on their composition. Very recent developments in the CVD growth of MoS<sub>2</sub> and these related TMDs [9,10] are currently enabling the production of various TMD heterostructures, including samples with tunable composition (e.g. Mo<sub>1-x</sub>W<sub>x</sub>S<sub>2</sub>) [11-13] and twisted bilayer MoS<sub>2</sub> [14,15]. As a result, the tools and theories we have developed to characterize graphene heterostructures may be relevant for a whole new class of materials. A few examples of potential future directions of our work for optical studies of these heterogeneous TMDs are presented below.

First, the optical absorption spectra of these TMDs contain many more features than those of graphene or *h*-BN. Figure 7.5 plots the UV-Vis absorption spectra of bulk MoS<sub>2</sub>, MoSe<sub>2</sub>, MoTe<sub>2</sub>, WS<sub>2</sub>, and WSe<sub>2</sub> [16] (the *x*-axis, shown in units of cm<sup>-1</sup>, ranges from ~1.25 (right) to 5.5 (left) eV). Here, many changes in the TMD absorption spectra are observed at visible and ultraviolet wavelengths as the atomic composition of the materials varies. Hence, absorption spectroscopy and hyperspectral imaging of these TMDs could provide a very sensitive way to image variations in composition. Using new advances in CVD growth, it is possible to produce lateral heterojunctions between TMDs of different compositions, much like the graphene/*h*-BN case [17]. Absorption spectroscopy may also be used to differentiate between existing designer TMDs where compositions of the chalcogen or metal atoms are varied

continuously, such as  $\text{Mo}_x\text{W}_{(1-x)}\text{S}_2$  [11-13]. Finally, we note that despite the wealth of spectral features at UV energies in this family of bulk TMDs, little is known about these features in the corresponding atomically thin materials, and DUV-Vis-NIR imaging of few-layer samples could be very fruitful.

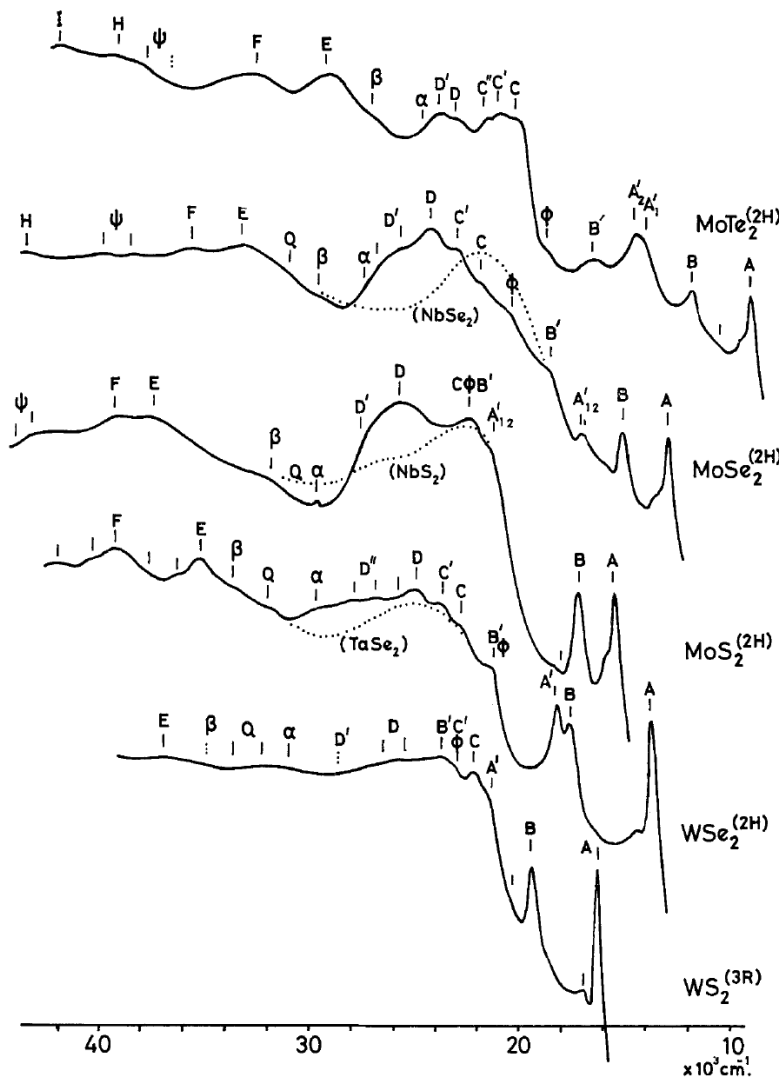


**Figure 7.5: Absorption spectra of bulk TMDs**

It is known that the optical absorption spectra of several bulk TMDs with different compositions contain a variety of interesting UV and visible energy spectral features. However, the corresponding atomically thin TMDs have almost exclusively been studied in the visible energy range only. [16]

Next, the optical properties of twisted bilayer MoS<sub>2</sub> have been the subject of recent research [14,15]. It was found that, as in oriented bilayer MoS<sub>2</sub>, twisted bilayer MoS<sub>2</sub> is an indirect band gap semiconductor for all  $\theta$  [14]. However, depending on  $\theta$ , the indirect gap energy varies by  $\sim 200$  meV. The majority of this variation is attributed to very small changes in the interlayer spacing as a function of  $\theta$ ; unlike the graphene case, the formation of new interlayer states was not observed in twisted bilayer MoS<sub>2</sub> in this study. However, this work focused only on the energy range very close to the band gap of the material. Thus, many questions remain about the properties of twisted bilayer MoS<sub>2</sub>. For example, it is known that the wavefunctions of the lower energy states in MoS<sub>2</sub> have more Mo character, while some of the higher energy states have more S character. Since the external S atoms from each layer of bilayer MoS<sub>2</sub> are in direct physical contact, while the Mo atoms are separated, the absorption spectrum of twisted bilayer MoS<sub>2</sub> over a larger energy range may reveal differences in the coupling between these different states. In addition, the excitonic effects for any existing interlayer states in twisted bilayer MoS<sub>2</sub> could be even more interesting than the graphene case, since additional, lower energy excitonic states already exist at the direct band gap of intrinsic MoS<sub>2</sub>. Electron-hole screening will be reduced due to the lower free carrier density in semiconducting MoS<sub>2</sub>, increasing the importance of excitons.

Finally, unlike graphene and *h*-BN, monolayer MoS<sub>2</sub> and related TMDs can exhibit visible photoluminescence (PL) due to their direct band gap. PL spectroscopy and imaging are currently standard tools for characterizing these few-layer TMDs, and it has been observed that grain boundaries [9], compositional variations [11,13,17], and layer number [6] can all have significant effects on their local PL intensity and PL peak energy. Our widefield Raman

microscope can be easily adapted for PL imaging, and the techniques we have developed can be used to correlate the physical structure and PL spectra of these materials in future studies.

#### 7.4 | Artificial vertical heterostructures

Next, as we mentioned at the end of Chapter 1, by sequentially transferring two arbitrary 2D layers onto a substrate, it is possible to form vertical heterostructures where the layers are in atomically precise contact (Figure 7.6) [18]. Through various combinations of graphene, *h*-BN, and TMDs, many novel devices have been created [19-29], and research in this area is ongoing.

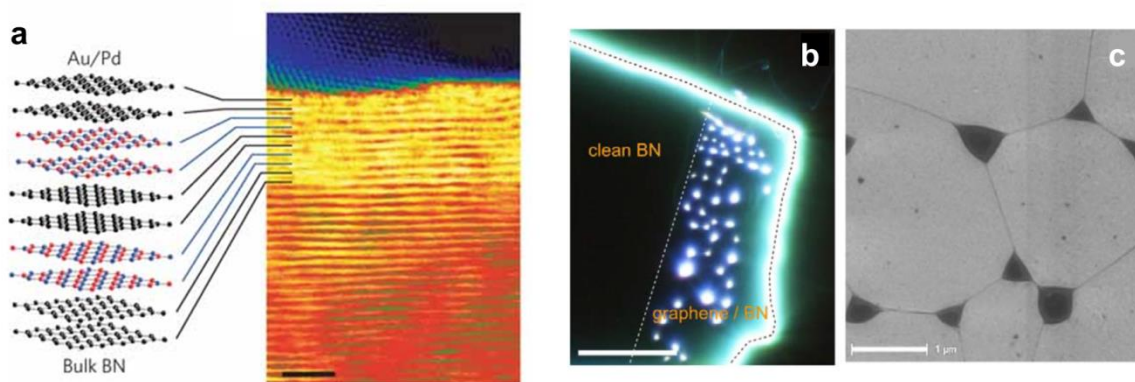


**Figure 7.6: Artificial vertical heterostructures**

(a) A cross-sectional TEM image showing atomically clean interfaces between stacked 2D materials. (b) A dark-field optical image which highlights the edges and bubbles of a graphene/*h*-BN vertical junction. (c) An SEM image showing the contamination channels in a graphene/*h*-BN stack. [18]

While we did not achieve interlayer coupling in the artificially stacked bilayer graphene that we presented at the end of Chapter 6 (published in 2012) [30], the technique to form coupled 2D layers is now fairly well-established. Realizing true atomic contact requires each layer to be very clean, and is often aided by annealing. However, it is still surprising that this contact can form between surfaces which are brought together in ambient air or liquid environments. Closer examination shows that while the majority of the area of the films is in close contact, the

adsorbates trapped between the films during transfer are pushed into channels which permeate the surface. The degree to which these channels affect the properties of the resulting material is currently unknown, and they have so far been avoided during the fabrication of individual devices. Both DUV-Vis-NIR hyperspectral imaging and widefield Raman imaging could be used to rapidly confirm and study the interlayer coupling in artificial 2D stacks over large areas, particularly for the established case of tBLG.

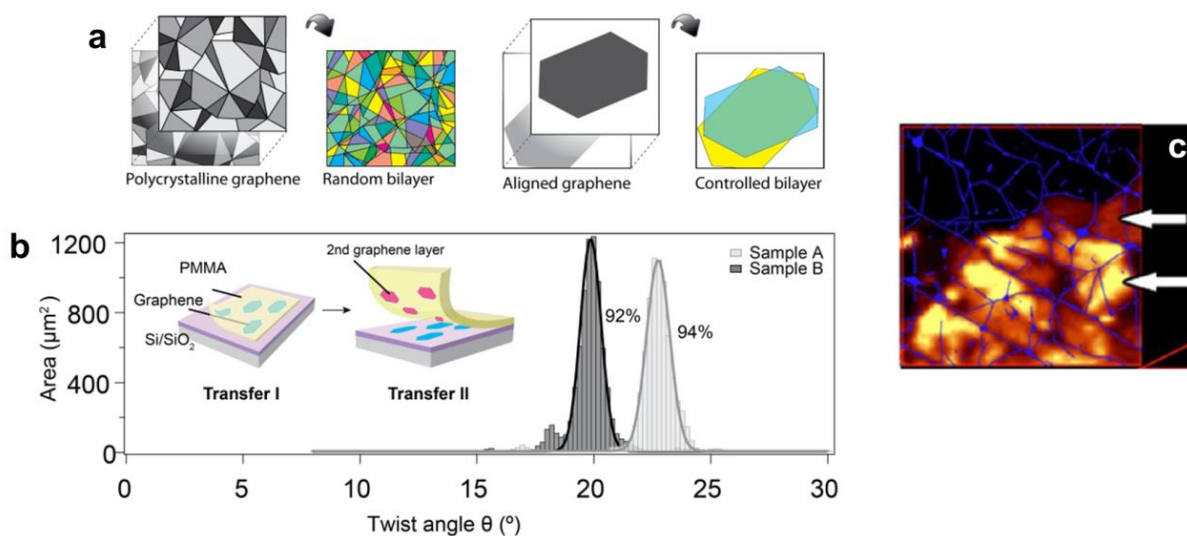


**Figure 7.7: Controlling twist angle in vertical stacks**

(a) A schematic illustrating the formation of tBLG with controlled  $\theta$ . (b) Histograms showing the  $\theta$  distributions in artificial tBLG samples with designed  $\theta$ , which were made from two highly oriented graphene monolayers. [31] (c) A G band Raman image, illustrating small variations in  $\theta$  which correlate with contamination channels (blue) in the artificially stacked sample. [32]

Efforts to control  $\theta$  in artificial stacks of 2D materials have already begun. To create a sample with controlled  $\theta$ , the orientation of each layer must be known (Figure 7.7a). This is difficult for exfoliated samples and polycrystalline CVD graphene, but possible with preferentially aligned growths where the shape of each island is a strong indicator of its orientation [31]. Figure 7.7b shows an example where our DUV-Vis-NIR microscope, described

in Chapter 3, was used to characterize  $\theta$  in a tBLG sample comprised of two highly aligned graphene layers; it was found that >90% of the tBLG had the designed  $\theta$ . However, due to the contamination channels in artificially stacked bilayers,  $\theta$  varies spatially across these samples, typically by  $\pm 1^\circ$  [32], even when the top and bottom layers are single crystals. Figure 7.7c shows a G band Raman image of an artificial tBLG sample excited close to its resonance. Small domains (arrows) have different G band intensities, corresponding to small variations in  $\theta$ , and these domains can be correlated with the contamination channels found in a corresponding AFM image (blue lines).

In addition, many 2D materials with different compositions have been combined into vertical heterostructures with novel properties. For example, *h*-BN is a high quality dielectric material for many other 2D devices due to its lack of reactive dangling bonds [22], and unique low temperature physics has been observed in oriented graphene/*h*-BN stacks [19-21] due to the large moiré periodicity of this system at  $\theta \approx 0^\circ$ . Just within the last few months, bilayer stacks of semiconducting TMDs with different band gaps have been the subject of studies by many groups [25-29] for their novel optical and optoelectronic properties, including the existence of a new interlayer exciton. However, with the exception of the low angle graphene/*h*-BN case, the effects of  $\theta$  have largely been ignored in these structures. Although many interesting properties appear to be  $\theta$ -independent in a variety of 2D stacks, it will be important to quantify the effects of  $\theta$  in these stacks in future work.

## 7.5 | Summary

Two-dimensional materials have continued to captivate scientists in a variety of disciplines for the past decade. Initially, graphene and other 2D materials were largely used as platforms to

study fundamental low-dimensional physics. However, the nature of the field changed when the large scale production of high quality 2D materials was enabled with chemical vapor deposition. While CVD has created the opportunity for 2D materials to be used for a number of practical applications, CVD also changed the way that the scientific community views 2D materials in general. CVD-grown samples can contain a variety of interesting structures, such as point defects, grain boundaries, and twisted multilayers, that were not found in exfoliated samples. The need to remove CVD samples from their growth substrates spurred advances in clean transfers, and ultimately enabled the vertical stacking of 2D materials to form designer heterostructures. CVD also provided control over the lateral composition of a growing 2D monolayer for the first time.

Within this setting, we developed new characterization tools specifically designed to study the growing family of heterogeneous 2D materials. The two optical imaging spectroscopy techniques described in this dissertation, DUV-Vis-NIR hyperspectral imaging and widefield Raman microscopy, are optimized to visualize spatial variations in composition, stacking order, and defect density for 2D materials transferred to a variety of substrates. In addition, when combined with direct structural imaging techniques such as DF-TEM, these tools enable the quantitative optical characterization of new 2D heterostructures. Our capabilities have allowed us to quantify the optical properties of one particular example, twisted bilayer graphene, in great detail, and we are still in the process of discovering new phenomena in this intriguing material. However, tBLG is a relatively simple system, especially compared with twisted bilayer MoS<sub>2</sub> and the heterogeneous vertical stacks introduced in this chapter. We anticipate that the tools we have developed will be essential for exploring the properties of a variety of other vertical and lateral 2D heterostructures for years to come.

## References

- [1] J. dos Santos, N. Peres, and A. Castro, *Physical Review Letters* **99**, 256802 (2007).
- [2] J. Sanchez-Yamagishi, T. Taychatanapat, K. Watanabe, T. Taniguchi, A. Yacoby, and P. Jarillo-Herrero, *Physical Review Letters* **108**, 076601 (2012).
- [3] Y. Miyauchi *et al.*, arXiv preprint arXiv:1308.5438 (2013).
- [4] K. F. Mak, F. H. da Jornada, K. He, J. Deslippe, N. Petrone, J. Hone, J. Shan, S. G. Louie, and T. F. Heinz, *Physical Review Letters* **112**, 207401 (2014).
- [5] R. W. Havener, Y. Liang, L. Brown, L. Yang, and J. Park, *Nano Letters* **14**, 3353 (2014).
- [6] K. Mak, C. Lee, J. Hone, J. Shan, and T. Heinz, *Physical Review Letters* **105**, 136805 (2010).
- [7] S. Tongay, J. Zhou, C. Ataca, K. Lo, T. S. Matthews, J. B. Li, J. C. Grossman, and J. Q. Wu, *Nano Letters* **12**, 5576 (2012).
- [8] W. J. Zhao, Z. Ghorannevis, L. Q. Chu, M. L. Toh, C. Kloc, P. H. Tan, and G. Eda, *ACS Nano* **7**, 791 (2013).
- [9] A. van der Zande *et al.*, *Nature Materials* **12**, 554 (2013).
- [10] Y. Zhan, Z. Liu, S. Najmaei, P. Ajayan, and J. Lou, *Small* **8**, 966 (2012).
- [11] Y. Gong *et al.*, *Nano Letters* **14**, 442 (2014).
- [12] D. Dumcenco, H. Kobayashi, Z. Liu, Y. Huang, and K. Suenaga, *Nature Communications* **4**, 1351 (2013).
- [13] J. Mann *et al.*, *Advanced Materials* **26**, 1399 (2014).
- [14] A. M. van der Zande *et al.*, *Nano Letters* **14**, 3869 (2014).
- [15] W. Hsu, Z. Zhao, L. Li, C. Chen, M. Chiu, P. Chang, Y. Chou, and W. Chang, *ACS Nano* **8**, 2951 (2014).
- [16] J. Wilson and A. Yoffe, *Advances in Physics* **18**, 193 (1969).
- [17] C. Huang *et al.*, arXiv preprint arXiv:1406.3122 (2014).
- [18] S. J. Haigh *et al.*, *Nature Materials* **11**, 764 (2012).
- [19] C. Dean *et al.*, *Nature* **497**, 598 (2013).
- [20] B. Hunt *et al.*, *Science* **340**, 1427 (2013).
- [21] L. Ponomarenko *et al.*, *Nature* **497**, 594 (2013).
- [22] C. Dean *et al.*, *Nature Nanotechnology* **5**, 722 (2010).
- [23] L. Britnell *et al.*, *Nano Letters* **12**, 1707 (2012).

- [24] L. Britnell *et al.*, *Science* **335**, 947 (2012).
- [25] H. Fang *et al.*, *PNAS* **111**, 6198 (2014).
- [26] S. Tongay *et al.*, *Nano Letters* **14**, 3185 (2014).
- [27] P. Rivera *et al.*, arXiv preprint arXiv:1403.4985 (2014).
- [28] C.-H. Lee *et al.*, arXiv preprint arXiv:1403.3062 (2014).
- [29] M. M. Furchi, A. Pospischil, F. Libisch, J. Burgdörfer, and T. Mueller, arXiv preprint arXiv:1403.2652 (2014).
- [30] R. Havener, H. Zhuang, L. Brown, R. Hennig, and J. Park, *Nano Letters* **12**, 3162 (2012).
- [31] L. Brown *et al.*, submitted (2014).
- [32] T. Beechem, T. Ohta, B. Diaconescu, and J. Robinson, *ACS Nano* **8**, 1655 (2014).